NATIONAL AERONAUTICS AND SPACE ADMINISTRATION

Space Programs Summary 37-54, Vol. I

Flight Projects

For the Period September 1 to October 31, 1968

JET PROPULSION LABORATORY
CALIFORNIA INSTITUTE OF TECHNOLOGY
PASADENA, CALIFORNIA

November 30, 1968

NATIONAL AERONAUTICS AND SPACE ADMINISTRATION

Space Programs Summary 37-54, Vol. I

Flight Projects

For the Period September 1 to October 31, 1968

JET PROPULSION LABORATORY
CALIFORNIA INSTITUTE OF TECHNOLOGY
PASADENA, CALIFORNIA

November 30, 1968

SPACE PROGRAMS SUMMARY 37-54, VOL. I

Prepared Under Contract No. NAS 7-100
National Aeronautics and Space Administration

Preface

The Space Programs Summary is a multivolume, bimonthly publication that presents a review of technical information resulting from current engineering and scientific work performed, or managed, by the Jet Propulsion Laboratory for the National Aeronautics and Space Administration. The Space Programs Summary is currently composed of four volumes:

Vol. I. *Flight Projects* (Unclassified)

Vol. II. *The Deep Space Network* (Unclassified)

Vol. III. *Supporting Research and Advanced Development* (Unclassified)

Vol. IV. *Flight Projects and Supporting Research and Advanced Development* (Confidential)

Contents

PLANETARY–INTERPLANETARY PROGRAM

I. *Mariner* Mars 1969 Project 1

A. Introduction 1

B. Project Engineering 2

C. Systems 5

D. Engineering Mechanics 15

E. Guidance and Control 25

F. Telecommunications 31

G. Space Sciences 45

I. *Mariner* Mars 1969 Project

PLANETARY–INTERPLANETARY PROGRAM

A. Introduction

1. Mission Description

The primary objective of the *Mariner* Mars 1969 Project is to make two flyby exploratory investigations of Mars in 1969, which will set the basis for future experiments—particularly those relevant to the search for extra-terrestrial life. The secondary objective is to develop Mars mission technology.

The spacecraft design concept is modeled after the successful *Mariner IV* spacecraft, considerably modified to meet the 1969 mission requirements and to enhance mission reliability.

The launch vehicle is the *Atlas/Centaur* SLV-3C, used for the *Surveyor* missions. This vehicle, developed by General Dynamics/Convair Company for the Lewis Research Center, has single- or double-burn capability in its second stage and a considerably increased performance rating over the *Atlas D/Agena D* used in the *Mariner IV* mission.

Mariner Mars 1969 missions will be supported by the Air Force Eastern Test Range launch facilities at Cape Kennedy, the tracking and data acquisition facilities of the Deep Space Network, and other NASA facilities.

The six planetary-science experiments selected by NASA for the *Mariner* Mars 1969 missions are listed in Table 1.

2. Project Status

Environmental testing of the flight spacecraft has been carried out, together with continued system-level functional testing. The first planning phase of the Mars encounter sequence was conducted and reviewed on September 13; a second iteration of the design was begun. Composite and spacecraft-adapter tests were completed on the launch vehicle, and the first vehicle was delivered to Cape Kennedy. The readiness of the Mission Operations System (MOS) for the test program was reviewed and demonstrated on September 19. The MOS participation in the second phase of the encounter

Table 1. *Mariner* Mars 1969 science experiments and investigators

Experiment	Investigator	Affiliation
Television	R. B. Leighton[a]	CIT
	B. C. Murray	CIT
	R. P. Sharp	CIT
	N. H. Horowitz	CIT
	A. G. Herriman	JPL
	R. K. Sloan	JPL
	M. E. Davies	Rand Corp.
	C. Leovy	University of Washington
	B. A. Smith	New Mexico State University
Infrared spectrometer	G. C. Pimentel[a]	UCB
	K. C. Herr	UCB
Ultraviolet airglow spectrometer	C. A. Barth[a]	University of Colorado
	F. C. Wilshusen	University of Colorado
	K. Gause	University of Colorado
	K. K. Kelly	University of Colorado
	R. Ruehle	University of Colorado
	J. B. Pearce	University of Colorado
	E. F. Mackey	Packard-Bell Electronics Corp.
	W. G. Fastie	Johns Hopkins University
Infrared radiometer	G. Neugebauer[a]	CIT
	G. Munch	CIT
	S. C. Chase	Santa Barbara Research Center, Hughes Aircraft Co.
S-band occultation	A. J. Kliore[a]	JPL
	G. Fjeldbo	Stanford University
	S. I. Rasool	Goddard Institute of Space Studies
Celestial mechanics	J. D. Anderson[a]	JPL
	W. L. Martin	JPL

[a]Principal Investigator.

sequence design was increased during October. The ninth project quarterly review was conducted on September 17 and 18.

B. Project Engineering

1. Launch Vehicle Integration

During this reporting period, the combined system testing program for the two launch vehicles, AC-19 and AC-20, was concluded. This program included composite testing of each vehicle, match-mating with the flight spacecraft adapters, and formal data reviews. The hardware changes incorporated between the AC-15 and AC-20 vehicles and the preliminary plans for the AC-17 launch were presented to the project on October 10. In late September, the AC-19 vehicle was shipped to the Air Force Eastern Test Range (AFETR), where checkout was begun. Spacecraft nose-fairing alignment tests were also conducted during the period.

Technical interface areas not yet fully resolved and under continuing effort include validation of the electrical/electronic interface at the launch complex, encapsulation and environmental procedures handling equipment/forward adapter alignment checks, and some flight-equipment calibration and analysis matters.

2. Spacecraft System Test and Operations

a. Introduction. Mariner Mars 1969 spacecraft system test operations progressed on schedule during September and October 1968 (SPS 37-50, Vol. I, Fig. 10, p. 42). During the period, all environmental testing of the flight spacecraft was completed.

b. Spacecraft M69-2.

Space simulation test, part I. Part I of the space simulation test began August 23 (SPS 37-53, Vol. I, p. 4) and ended on September 3 after 260 h of spacecraft operation. Problems were encountered with temperature control of some of the scan platform instruments and in performing the infrared spectrometer cooldown. Because of these problems, part II of the space simulation test was divided into two parts: part IIA corresponded to the temperature control test normally performed during part II; part IIB included a repeat of the infrared spectrometer cooldown test and several engineering tests associated with the encounter sequence.

Space simulation test, part IIA. Spacecraft M69-2 was prepared for part IIA of the space simulation test during the period September 3–5. Preparation included the removal of externally mounted test equipment, stimuli, test cables, and other hardware that could interfere with the compilation of good data for temperature control subsystem performance evaluation.

Space simulation test, part IIA, was satisfactorily conducted during the period September 5–12 in the 10-ft space simulator. Part IIA of the test was developed to verify spacecraft temperature control design. Data compiled during part IIA were used in making adjustments to the temperature control design of some of the scan platform instruments. The adjustments were verified during part IIB.

Space simulation test, part IIB. Preparation of spacecraft M69-2 for space simulation test, part IIB, was completed on September 14. The spacecraft temperature control subsystem was modified based on data obtained during part IIA. The spacecraft was also prepared for another cooldown sequence of the infrared spectrometer.

Part IIB of the space simulation test was performed from September 14 to 17. Good encounter and playback data were obtained and, although problems were encountered, a satisfactory cooldown of the infrared spectrometer was performed. The modifications made to the temperature control design proved adequate.

Vibration test. The spacecraft was returned to the JPL Spacecraft Assembly Facility on September 18 for the vibration test. Preparation included assembly of the spacecraft to the launch configuration (installation of solar panels, etc.) and the installation of instrumentation accelerometers at key locations. Final preparation was completed on September 24 after the spacecraft was installed on the vibration equipment in the environmental and dynamics test laboratory.

The vibration test performed from September 24 to 26 verified that the spacecraft could operate satisfactorily during and after exposure to vibration levels based on those expected from the *Atlas* and *Centaur* launch vehicles during the boost phase. The spacecraft was vibrated in three different axes: (1) the Z axis, (2) the *X* axis (vibration equipment attached to bay I), and (3) an *X–Y* axis (vibration equipment attached to bay VIII). Following vibration in each axis, a brief test was performed to verify that spacecraft performance had not been degraded by vibration.

Pyrotechnic shock test. The flight spacecraft pyrotechnic shock test was performed immediately after completion of the vibration test while the spacecraft was still installed on the spacecraft adapter. The flight spacecraft test was considerably reduced in scope from the proof-test model test performed in June (SPS 37-52, Vol. I, p. 4). In the test performed on spacecraft M69-2 on September 26, only the spacecraft adapter V-band pyrotechnics were detonated. Good data were obtained during the test.

Weight and center of gravity. Spacecraft M69-2 weight, center-of-gravity location, and the required adjustment to the propulsion subsystem thrust axis were measured from September 27 to 30. Spacecraft launch weight was 845.2 lb. The measured center-of-gravity location in spacecraft coordinates was $\overline{X} = +0.188$ in., $\overline{Y} = +0.541$ in., and $\overline{Z} = -9.047$ in. The alignment error after adjustment of the propulsion subsystem thrust axis was 0.032 in.

Simulated precountdown. The launch precountdown was simulated on October 2. The purpose of the precountdown was to perform the most detailed spacecraft verification permitted within the limits of the launch configuration and the launch complex equipment (LCE). No significant problems were encountered during the precountdown.

Simulated countdown. On October 3, a simulated countdown was performed on spacecraft M69-2 using the LCE and the system test complex. The purpose of the simulated countdown was to provide training for personnel who take part in spacecraft launch operations at the Air Force Eastern Test Range and to develop an optimum sequence for conditioning the spacecraft for launch and for taking engineering measurements that aid in postlaunch acquisition and spacecraft performance analysis. During the test, several prelaunch conditioning problems were detected; among them were telemetry data offsets caused by electromagnetic interference caused by simulated C-band radar signals and *Centaur* telemetry.

System test 2. System test 2 was performed from October 8 to 16; the functional performance of the spacecraft as an integrated system was verified. The spacecraft was operated in all of the major elements of a nominal flight sequence. The spacecraft was exercised through the central computer and sequencer and direct-command-controlled encounter sequences and a variety of trajectory correction maneuvers.

Scan platform instrument alignment. During the alignment of the scan platform instruments on October 23, the line of sight of all planetary instruments mounted on the scan platform was measured with respect to each other and to a reference plane on the scan platform.

Scan control subsystem telemetry calibration. A scan control subsystem telemetry calibration was conducted on October 24 and 25 to provide accurate data concerning the correlation between the telemetered scan platform position data and the actual position of the scan platform clock and cone axes.

Spacecraft disassembly, cleaning, and inspection. Spacecraft disassembly, cleaning, and inspection began

on October 26 and continued through the remainder of the month. The spacecraft was disassembled to the subassembly level (i.e., to the lowest level that could be achieved by demating connectors), cleaned, and inspected microscopically. Selected subsystems were returned to subsystem laboratories for calibration and margin testing.

c. Spacecraft M69-3.

System test 1. Spacecraft M69-3 system test 1 began on August 28 (SPS 37-53, Vol I, p. 4) and was completed on September 4. During the test, the spacecraft was operated in all major elements of the nominal flight sequence.

Scan platform instrument alignment. Scan platform instruments were aligned on September 6 and 10 using the same method employed for spacecraft M69-2.

Space simulation test, part I. Spacecraft M69-3 was prepared for space simulation testing in the JPL 10-ft space simulator from September 12 through 23. Over 75 instrumentation thermocouples and about 35 auxiliary heaters for spacecraft temperature control and analysis were installed on the spacecraft and associated support equipment in the space simulator.

Following installation of the spacecraft on the simulator endbell and connection of electrical cabling to the spacecraft, a preliminary test equipment and spacecraft verification was performed.

Part I of the space simulation test was performed during the period September 23–October 4. The purpose of part I was to demonstrate long-term (about 250 h) spacecraft functional performance while operating in a simulated space environment. Each of the key segments of the flight sequence was repeated several times during the test. The nominal environment for the test was a pressure of less than 5×10^{-5} torr and a space simulator cold-wall temperature of about $-300°$F.

Space simulator test, part II. During spacecraft preparation for space simulation test, part II (October 4–7), externally mounted test equipment, stimuli, test cables, and other hardware that could interfere with the compilation of accurate temperature control data were removed.

Space simulation test, part II, was successfully conducted from October 7 to 17 in the 10-ft simulator. In addition to verifying the spacecraft temperature control design, real-time 33-, 33-, and 17-picture encounter sequence was performed.

Simulated precountdown. A simulated precountdown was performed on October 26 and 28. During the precountdown, the most detailed spacecraft verification permitted within the constraints imposed by the launch configuration was conducted. Many procedural problems were found during the exercise.

Simulated countdown. A simulated countdown was conducted on October 28 to provide training for the personnel who will take part in spacecraft launch operations and allow further refinement of the procedure to be used for conditioning the spacecraft for launch. During the test, all operations went smoothly and no problems were encountered.

Vibration test. Spacecraft M69-3 vibration testing began on October 31 in the environmental and dynamics test laboratory. The purpose of the test was to verify that the spacecraft could operate satisfactorily during and after exposure to vibration levels based on those of the *Atlas/Centaur.*

Center of gravity. The measured center-of-gravity location in spacecraft coordinates was found to be: $\overline{X} = +0.139$ in., $\overline{Y} = +0.522$ in., and $\overline{Z} = -8.995$ in.

d. Spacecraft M69-4.

Subsystem interface and subsystem tests. Subsystem interface testing began shortly after initial power application on August 21 (SPS 37-53, Vol I, p. 5) and continued through early September. Following the verification of subsystem interfaces, each newly installed subsystem underwent a detailed subsystem test. The subsystem test provided a comprehensive evaluation of subsystem performance while operating on spacecraft power and allowed a preliminary determination of any possible effects the subsystem may have had on the spacecraft environment. Subsystem interface and subsystem tests were completed by the start of system test 1 on September 23.

Scan control subsystem telemetry calibration. A scan control subsystem telemetry calibration was performed on September 9 and 10 to provide accurate data concerning the correlation between the telemetered scan platform position data and the actual position of the scan platform cone and clock axes.

Spacecraft telemetry channel calibration. During mid-September, spacecraft telemetry channel calibrations were verified and, when necessary, corrected. During the end-to-end calibrations, data were obtained that allowed verification of computer-derived curves describing the relationship between the data numbers telemetered by the spacecraft flight telemetry subsystem and the engineering parameter (e.g., voltage, temperature, or pressure) being transduced on the spacecraft.

System test 1. System test 1 was performed from September 23 to October 3 to verify the functional performance of the spacecraft as an integrated system for the first time. All major parts of the nominal flight sequence were tested, including several types of encounter sequences and trajectory correction maneuvers.

Weight and center of gravity. Spacecraft M69-4 weight and center of gravity parameters were measured during the period October 7–10. The measured center-of-gravity location in spacecraft coordinates was found to be: $\bar{X} = +0.213$ in., $\bar{Y} = +0.540$ in., and $\bar{Z} = -8.992$ in. The alignment error after adjustment of the propulsion subsystem rocket engine undeflected thrust axis was 0.054 in. Spacecraft launch weight, less adapter, was 846.3 lb.

Vibration test. The spacecraft was prepared for vibration testing from October 11 to 17 and tested from October 17 to 19. The test demonstrated that the spacecraft could successfully operate during and after exposure to simulated *Atlas/Centaur* vibration levels. The spacecraft was vibrated in the Z, *X*, and *X–Y* axes; after each axis of vibration, a brief verification test was performed.

Scan platform instrument alignment. The scan platform instrument alignment was verified on October 15 while the spacecraft was being prepared for vibration testing. A second verification of scan platform instrument alignment was performed on October 21 and 22 to verify that alignments were not affected by vibration.

Simulated countdown. A simulated countdown was performed on October 23 for personnel training and further development of the countdown procedure. The problems encountered during the operation were primarily procedural. The electromagnetic interference problems encountered during the M69-2 countdown were accounted for in the new procedure produced for the M69-4 countdown.

Simulated precountdown. The simulated precountdown was performed on October 24, a day after the countdown. During the detailed examination of the spacecraft in the launch pad environment, many procedural problems were encountered.

Space simulation test, part I. Spacecraft M69-4 was prepared for space simulation tests in the 10-ft space simulator during the period October 25–31. The television subsystem was removed to investigate an intermittent condition. Before transportation of the spacecraft to the space simulation facility, instrumentation thermocouples and auxiliary heaters were installed. After installation of the spacecraft on the space simulator endbell, electrical cabling was connected to the spacecraft and a preliminary spacecraft and test equipment verification was conducted.

C. Systems

1. Systems Analysis

a. Trajectory targeting. Revision B to the detail *Mariner* Mars 1969 target specification was issued on July 17, 1968. This specification contains the selected post-separation spacecraft aiming points and arrival times at Mars for the 76 launch date/arrival date (LD/AD) cases that are to be targeted (have *Centaur* guidance tapes prepared) for the *Mariner* Mars 1969 mission. Figure 1 illustrates the location of the biased aiming points (biased to satisfy planetary quarantine requirements) for the nominal *Mariner F* and *G* trajectories. All 76 specified trajectories have since been targeted by General Dynamics/Convair, San Diego. The closed-loop final check trajectories were received at JPL on October 3 and approved on October 16, 1968.

The *Mariner* Mars 1969 launch period utilization and constraints document was published on October 15. This document describes the characteristics of the basic launch plan and delineates the characteristics and constraints associated with the utilization of the *Mariner* Mars 1969 launch period and daily launch windows. Figures 2 and 3 illustrate characteristics of the near-earth tracking coverage. Additional data concerning the behavior of various trajectory parameters during the 76 daily launch windows may be found in Ref. 1.

b. Spacecraft delivery accuracy. As a result of a recent degradation in the estimated accuracy of controlling

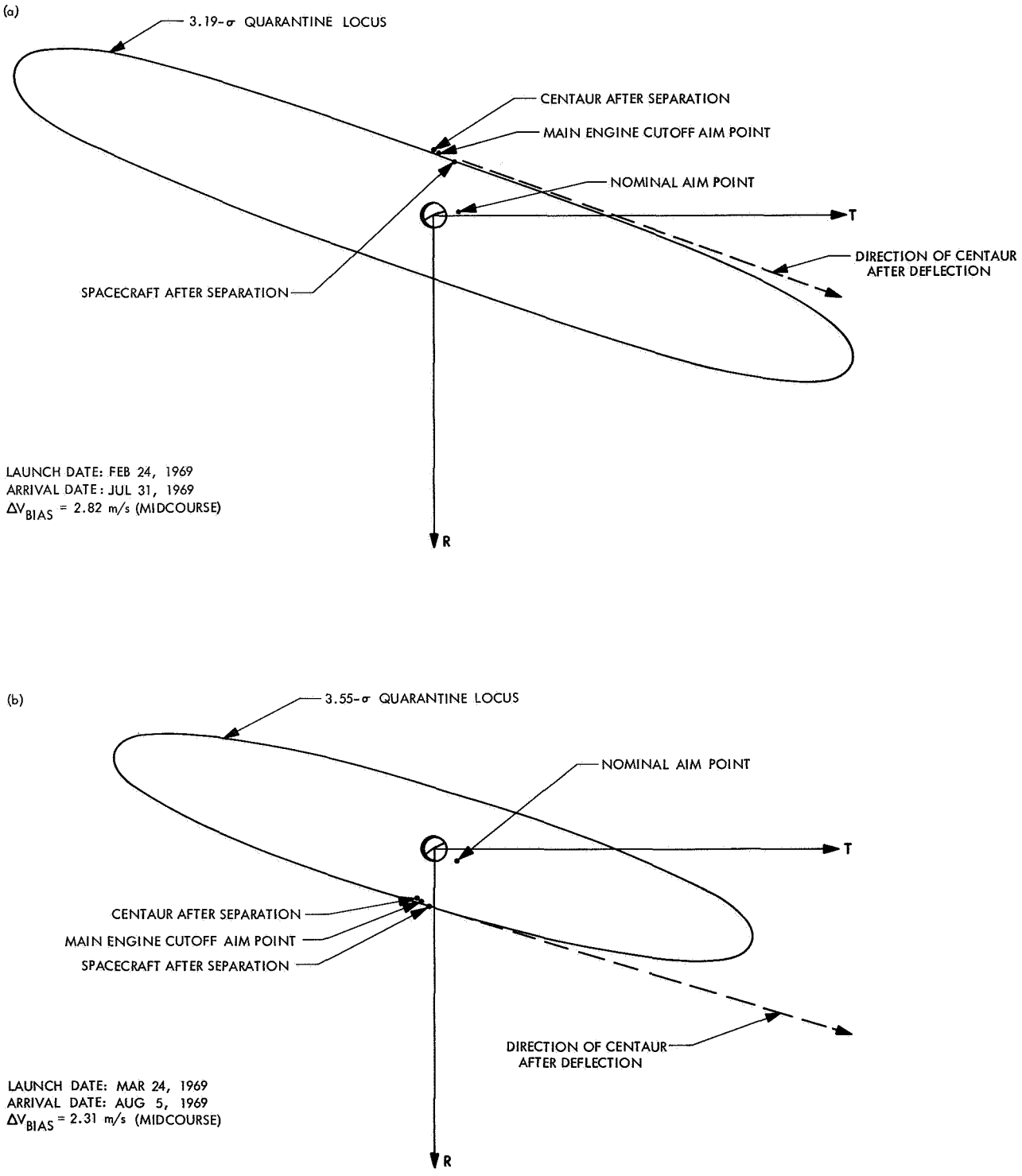

Fig. 1. Biased targeting aim diagrams: (a) *Mariner F*, (b) *Mariner G*

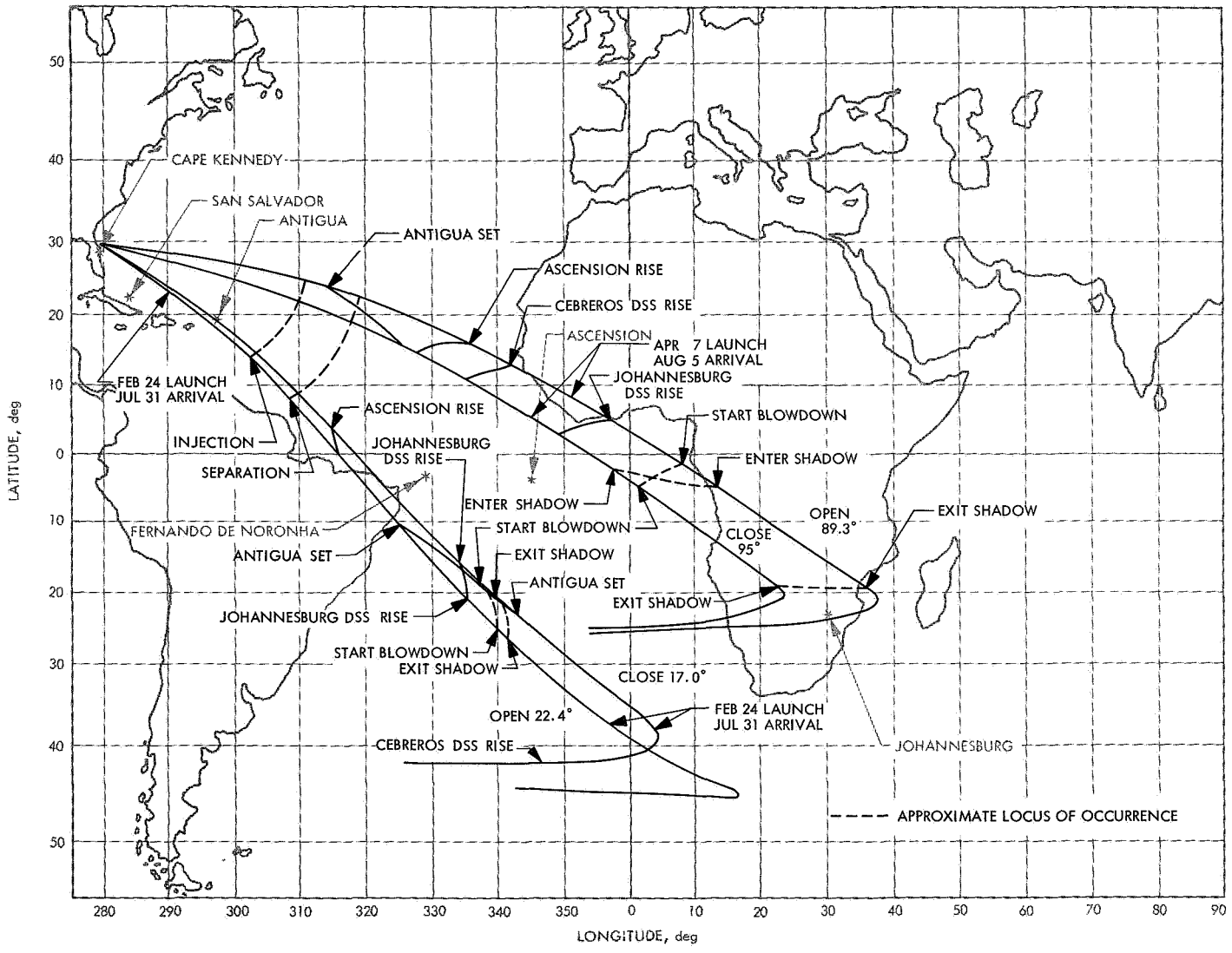

Fig. 2. Earth tracks for bounding launch azimuth cases

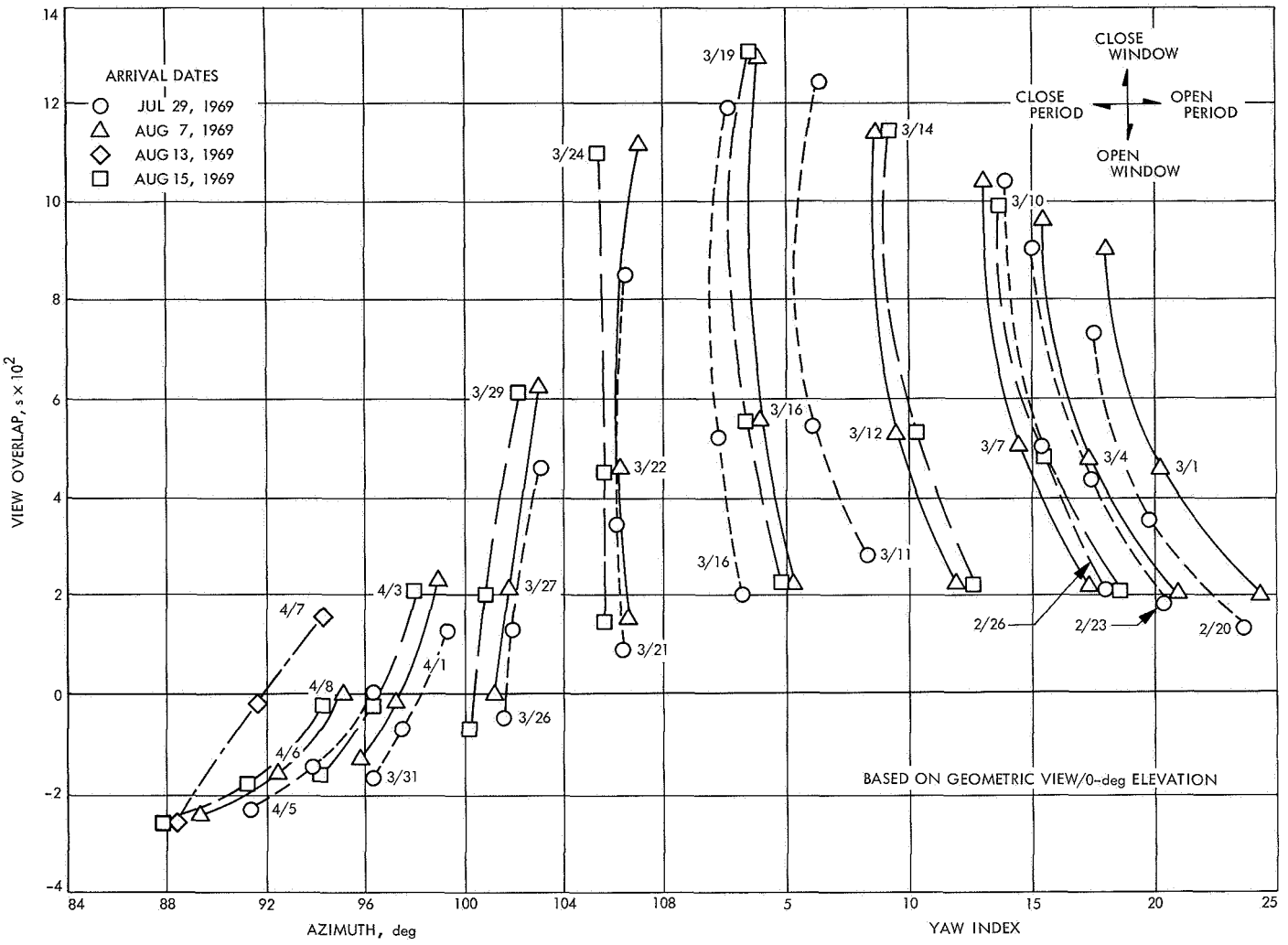

Fig. 3. Antigua/Ascension overlapping coverage as a function of launch azimuth or yaw index

the magnitude of the midcourse velocity increment magnitude, the spacecraft delivery accuracies were recalculated and are shown in Fig. 4 for the nominal *Mariner F* and *G* LD/AD cases. These figures show the total accuracy including both maneuver execution errors and orbit determination uncertainties at the time of the maneuver. The first maneuver dispersion ellipse is dominated by maneuver execution errors, whereas the second maneuver dispersion ellipse is dominated by orbit determination errors. The probabilities of delivering the spacecraft to the desired science aiming zone with only one trajectory correction are at least 0.75 for the *Mariner F* trajectory, and at least 0.95 for the *Mariner G* trajectory. If two corrections are performed, *a priori* probability is at least 0.99 for all trajectories.

c. Far-encounter TV picture coverage. During the time period from about 72 to 4 h before encounter (closest approach with Mars), several narrow-angle TV pictures of Mars are planned. The actual pictures obtained must meet, as a minimum, certain coverage requirements. These requirements, in order of importance, are:

(1) "Full-planet" coverage (all longitudes).

(2) Coverage of those areas that will be subsequently covered at higher resolution during the near-encounter scan phase.

(3) Coverage of Syrtis Major, Elysium, and Trivium Charontis.

(4) Coverage of the *Mariner IV* area.

(5) Coverage of the moons Phobos and Deimos.

In planning for the coverage of the surface feature areas, it was necessary to establish the geometrical

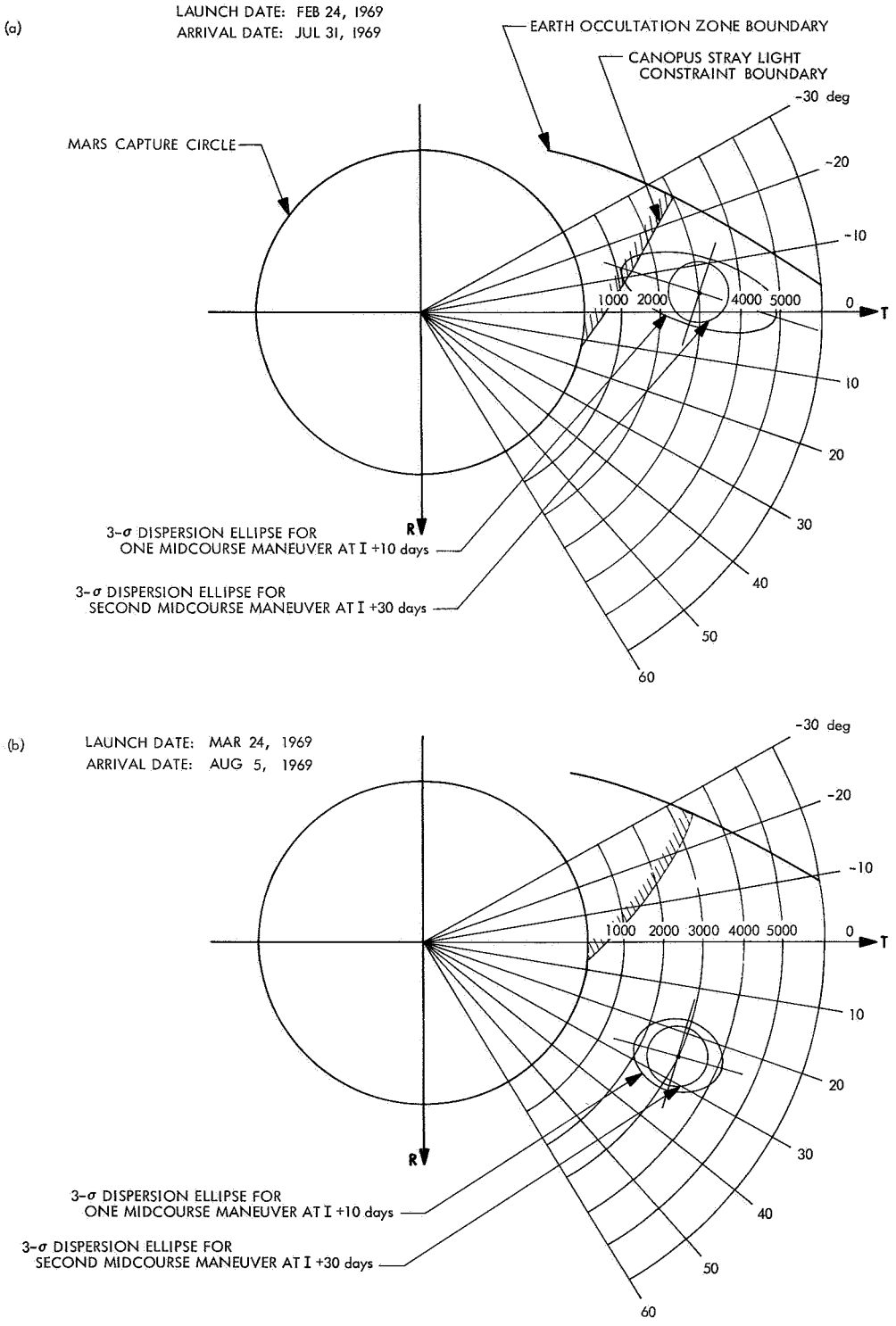

Fig. 4. Maneuver dispersion accuracy: (a) *Mariner F*, (b) *Mariner G*

conditions that would produce the best pictures. It was concluded that the best pictures would be obtained when the feature is photographed within about ±30 deg of the sub-spacecraft point (Fig. 5). This applies to the far-encounter pictures only, where the picture resolution is coarse (for good topographic relief for the near-encounter pictures, the scene should be located in the region of 15 to 50 deg from the terminator). Using the value criteria identified in Fig. 5 and the assumed feature longitudes given in Table 2, times were determined for photographing the areas of interest for the two preferred arrival dates of July 31 and August 5 (Fig. 6). Closest approach to Mars has been assumed to occur at 1 h 55 min past Goldstone zenith. The value trapezoids shown in Fig. 6 have been shortened in time width whenever the longitude width of the surface feature exceeds about 30 deg. Reference marks have also been shown on the near-encounter area trapezoids to indicate at what times during far encounter certain near-encounter regions are near the sub-spacecraft point.

The times for photographing the two moons of Mars shown in Fig. 6 are explained in Fig. 7. A higher value has been assigned for taking a picture when the moon is near one of the planet limbs than when it is near the edge

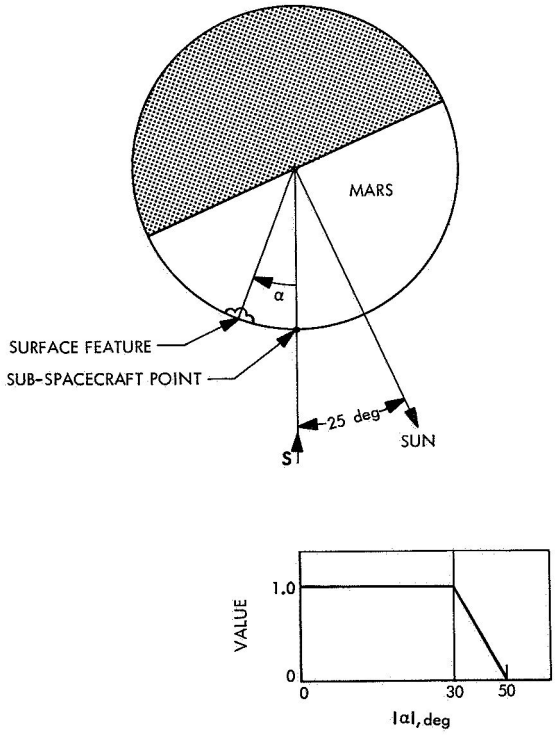

Fig. 5. Preferred surface feature location for far-encounter TV pictures

Table 2. Assumed feature longitudes

Feature	Longitude of feature center, deg	Longitude width of feature, deg
Near-encounter area for Jul 31 arrival	345	100
Near-encounter area for Aug 5 arrival	30	100
Syrtis Major	70	16
Elysium	145	30
Trivium Charontis	162	10
Mariner IV area	200	40
Solis Lacus	275	25

of the narrow-angle camera (TV-B) field of view. This has been done because of the greater possibility of missing the moon, as a result of pointing errors in the far-encounter planet sensor (FEPS)/TV-B system, when the moon is near the edge of the TV-B field of view. On the other hand, acquiring a moon near the limb of Mars is "merely" a matter of timing based on the estimated uncertainty in the ephemeris of the moons. It has been estimated that, at any given time, the position uncertainty of a moon along its orbit does not exceed about 500 km. Each moon travels fast enough to cover this distance in roughly 5 min. Thus, one need only wait 5 min (or advance, as the case may be) from the time when the moon is predicted to cross the limb before taking a picture.

In generating the moon timing data shown in Fig. 6, there was insufficient time to consider the offset between the planet center of brightness and the planet center. Thus, the times when the moons enter and leave the TV-B field of view are not accurate. For example, points 2, 3, 6, and 7 for the Deimos orbit shown in Fig. 7 should be shifted slightly towards the righthand side of the figure. However, as it is better to photograph (when under FEPS control) the moons when they are near one of the Mars limbs, this error is not significant.

From Fig. 6, it can be seen that pictures of the moons are not feasible under FEPS control after about $E - 12$ hours, as Mars fills up the entire TV-B field of view, and pictures of the moons in front of the bright Mars disk probably could not be seen. Furthermore, even at $E - 12$ hours, the estimated diameter of Phobos (about

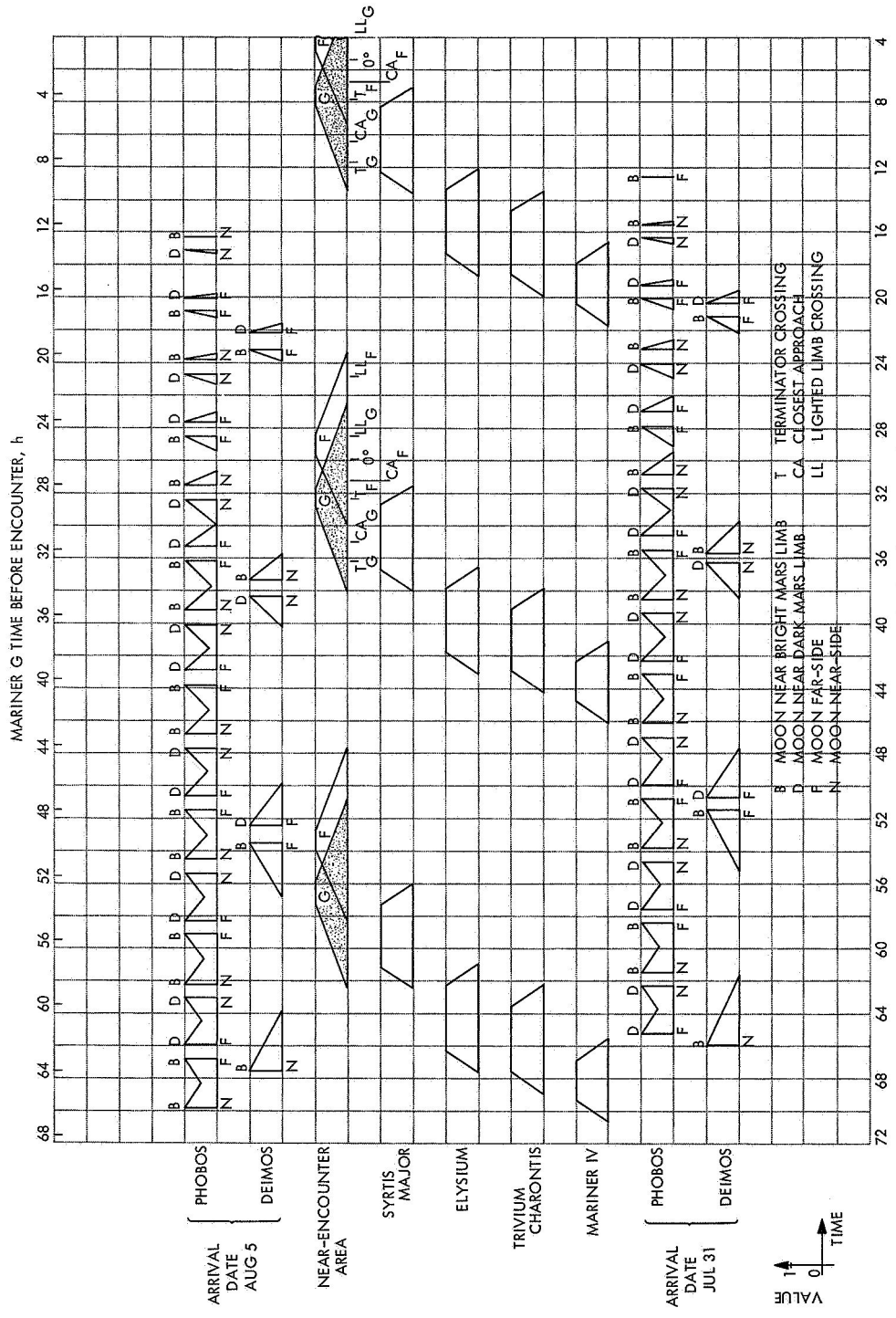

Fig. 6. Times of highest value for photographing various features of interest

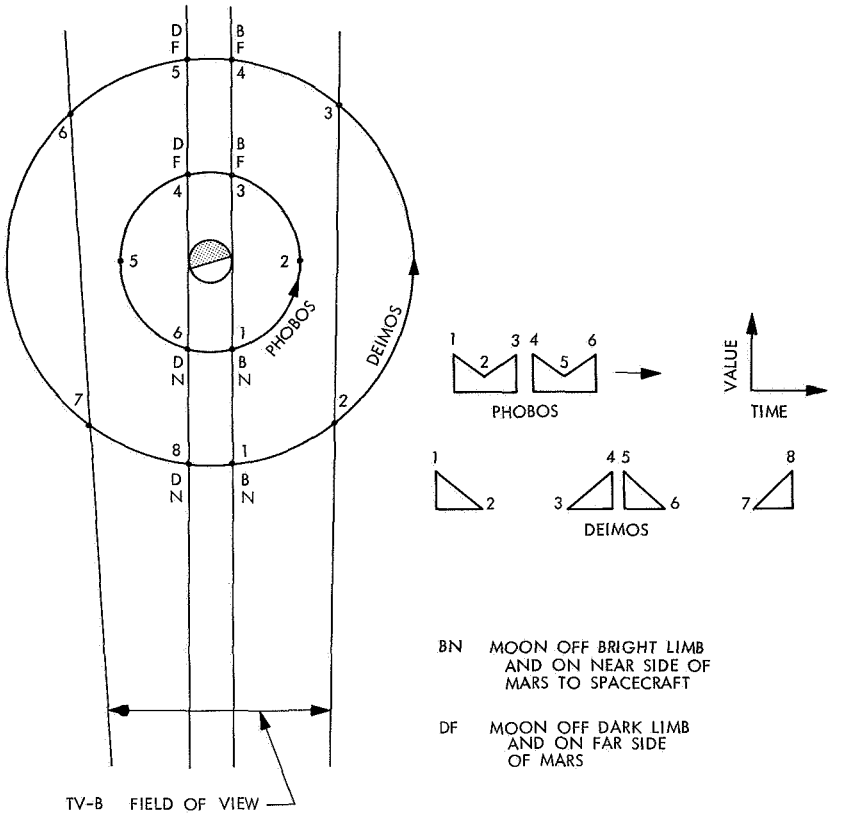

Fig. 7. Preferred moon locations for far-encounter TV pictures

15 km) is sufficiently small that only some 3 picture elements might be illuminated by Phobos. If it were feasible to take a central computer and sequencer or ground-commanded picture of Phobos as late as $E - 4$ hours, some 20 to 40 picture elements might be illuminated. However, as the moon pictures were assigned lowest priority during the far-encounter picture sequence, close-up pictures of the moons are not expected.

Reference

1. *Launch Time Dependent Excess Propellant Data for Mariner Mars 1969 Missions*, Revised, Report GDC63-0495-49, Appendix D. General Dynamics/Convair, San Diego, Calif., July 1968.

2. System-Test-Complex Data System

a. Test support. During this reporting period, the system-test-complex data system (STCDS) supported the nearly continuous space simulator testing of spacecraft M69-2 and M69-3, and the sequence of system tests of spacecraft M69-3, M69-4, and M69-2 (system test 2).

Additional investigations at the system level were also supported. These investigations included the TV–data storage subsystem (DSS)–flight telemetry subsystem (FTS) tests for investigating performance of the entire TV system by comparison of the real-time hardline output from the TV subsystem with digital and analog DSS outputs, at both high rate from the FTS block coder and the digital recorder playback rate of 270 bits/s. Supplementary capabilities for providing quick-production TV pictures and data are described in *Subsection 3, UNIVAC 1219 Data Processing System.*

The function of the STCDS test coordinator was continued during this period (see SPS 37-52, Vol. I, p. 9) since it is of value in increasing the reliability of support, especially when failures occur, when changes in configuration are required, and during startup of the system.

b. System development. An additional line printer was added to provide science analysis area display support according to the originally planned configuration of one test complex operational support equipment (OSE) printer and two science analysis area printers.

Program assembly H was used for all operations during this period. Assembly I is in checkout and is expected

to replace H during the next break in test support. The need for additional program assemblies is not anticipated.

Work is being done to improve the processing of science error messages that are generated from the correlation of response (as indicated by spacecraft telemetry data) with stimulus (as indicated by the occurrence of hardline events or change of status). Problems have been caused by lack of understanding of the detailed timing and sequencing of the stimuli and responses associated with the data automation subsystem clocking of events, data encoder sequences, and STCDS internal time tagging of data.

The software for use at the Air Force Eastern Test Range (AFETR) to unblock and distribute telemetry data received from the Deep Space Instrumentation Facility stations via high-speed data line has been developed and checked using data transmitted from the telemetry and command processor computer located in Compatibility Test Area 21 at JPL.

Problems were encountered in the wiring and checkout of the additional telemetry input module for use in the minor support configuration and its use has been delayed about 2 mo beyond the original schedule. Various malfunctions of data input subsystem B were uncovered and corrected during its use on system-test-complex 3; the counter input module was inoperative during this period because of power supply failure. No significant use of the low-speed analog module capability has been made. Although the system is operational, work on other problems has prevented obtaining necessary coefficients for conversion of raw data to engineering units, without which the system has no significance to the users. Further attempts to use this capability will probably be abandoned.

The functional utilization of the 65,000-word core memory of each CDC 3300 computer is shown in Table 3 for each routine utilizing more than 1000 words in the real-time support program. This program provides the capability for encounter test support of one spacecraft (or nonreal-time processing of encounter data), and simultaneous engineering telemetry decommutation and display from a second spacecraft with complete printer output as well as cathode-ray tube (CRT) display. At present there are only 314 core positions remaining that are not used by the support program.

The hardware and software were completed to permit tape playback of image-processing laboratory (IPL)-formatted TV data in either the 972- or 6804-bit format to the science OSE, where the digital data are converted to analog form for quick-look display and photography on the TV monitor. This capability is expected to be used at AFETR for quick validation of TV data or IPL tape production.

Table 3. STCDS core utilization by function

Function	Instructions	Operands
Executive program	1204	440
Input/output processors		
Message router formatter	1064	6066
Control	2633	3380
High-speed input (113.4 and 86.4 kbits/s)	3593	—
Magnetic tape	630	2237
Full frame display	724	1174
Operator console	334	1424
Plotting	560	1136
Low-speed input	1099	—
Other processors		
Standard	1198	6842
Input message	4216	2465
Telemetry decommutation	4139	2313
Science special	3146	2977
Engineering special	2010	341
CRT display	1212	607
Central computer and sequencer	932	622
Events, status, command, and digital data	1107	160
Analog data	947	218
All others	2020	366
Total	32768	32768

c. Nonreal-time processing. Requirements for STCDS production of IPL-formatted tapes were significantly reduced as a result of transferring the function of IPL tape preparation to the UNIVAC 1219 computer system, which accomplishes this function in real time from the block-coded 86.4-kbit/s data input.

Improvements were made in the programs and efficiency of operations associated with the use of the JPL Scientific Computing Facility for plotting engineering data from STCDS decommutated-format tapes, or ultraviolet spectrometer/infrared spectrometer (UVS/IRS) spectra from any IPL format tapes. Real-time plotting of IRS data is limited to the display of about 1/6 of the actual data, and UVS plot output is limited to about

1/20 of the available data, although an algorithm exists that smooths UVS spectral segments and compares the deviation in value of segment readings in successive spectra. Nonreal-time processing provides full plotting of all data samples. In the IRS plots, care is taken to prevent precession of the data frame from one plot to the next and to assure that the plotter presents the 667 data samples on a linear time scale. This is required because of the need to overlay plots in a back-to-back sense to obtain correct registration of the respective spectra during different scans of the instrument.

3. UNIVAC 1219 Data Processing System

The *Surveyor* Spacecraft Checkout Computer Facility, consisting of two UNIVAC 1219 computers and one 1218 computer, is planned to be used as the system-test-complex data system (STCDS) for *Mariner* Mars 1971. Because of its availability, the system will be used to support the proof-test model testing of *Mariner* Mars 1969 after launch; thus, one of the leased CDC 3300 computer systems can be returned to the vendor earlier than scheduled.

The UNIVAC 1219 Data Processing System (SPS 37-53, Vol. I, p. 6) is used to supplement the STCDS by performing real-time block decoding of the high-rate data. The prime image-processing laboratory (IPL)-formatted tape is also produced in real time from this data. These tapes provide common formats for transmission of science data between STCDS, UNIVAC 1219, and the IPL. Near the end of the reporting period, hardware interfaces were developed in the UNIVAC 1219 systems to also permit acquisition and logging of the 18.9-kbyte/s data from the science operational support equipment (OSE) and the 16.2-kbit/s hardline data that are transferred from the data automation subsystem (DAS) to the digital data storage subsystem (DSS). The OSE side interfaces are identical to those used by the STCDS, and will be used by the UNIVAC 1219 only as a backup to the normal STCDS function during periods of STCDS equipment malfunction or inability to support operations because of overcommitment.

A capability has been developed in the UNIVAC 1219 (or 1218) computer to drive the *Surveyor* spacecraft TV ground data handling system (now called TV-1). This function can provide TV pictures from spacecraft test or TV calibration data on a quick-look production basis, and has proven valuable in assessing problems in the TV–DSS areas of the spacecraft. A statistical analysis program was developed that permits analysis of the transfer function of the analog DSS and the high-rate system block encoding/decoding function. The program produces histograms showing the amplitude distribution of the digital value of the output picture elements that result from the occurrences of each discrete input picture element value in the TV video, DAS coding, or TV coding information.

Use of the UNIVAC 1219 system is being planned for obtaining quick-look prints and plots of science data at spacecraft encounter for mission operations purposes. The system will also be used for preparation of the science master data library. Development of these functions will be reported in subsequent SPS articles.

4. Mission Operations

Mission operations personnel training described in the Mission Operations Training Plan and shown on the Mission Operations Training Schedule has been completed in October except for the maneuver G/cruise F exercise, which has been delayed until November. After completion of the maneuver G/cruise F training exercise, the tests described in the Space Flight Operations Test Plan and scheduled in the Mission Operations Test Schedule will begin. The main difference between these tests and the exercises recently completed is the involvement of the deep space stations in the testing and, at a later date, the introduction of anomalies into the testing.

The Phase IA simulation program for the EMR 6050 computer (described in SPS 37-51, Vol. I, p. 10) completed acceptance-testing early in this reporting period. The program is used to provide simulated *Mariner* Mars 1969 spacecraft telemetry data for use by spacecraft performance analysis personnel during mission operations training and testing. The simulated data are derived from actual spacecraft telemetry data taken from a flight spacecraft during system testing and modified in the computer to appear more realistic and to follow a predetermined sequence of events. This simulation has been used in training exercises for both mission operations personnel training and spacecraft performance analysis personnel training.

A review of the proposed encounter sequence for the *Mariner* Mars 1969 spacecraft was held on September 13 for the purpose of examining and evaluating the far- and near-encounter sequences that must be contained in the on-board spacecraft computer prior to launch. A second encounter sequence design effort, with particular emphasis on the mission operations aspects of the encounter

sequence, will be conducted early in the next reporting period.

D. Engineering Mechanics

1. Cabling Subsystem

The flight cabling subsystem consists of the following components:

(1) Upper ring harness and harness tray.

(2) Science platform harness.

(3) Lower ring harness.

(4) Spacecraft to *Centaur* mounting adapter harness.

The purpose of the upper ring harness is to interconnect (1) all electronic assemblies in the spacecraft with one another, (2) all instruments on the upper bus through the ring harness to the electronic assemblies as required, and (3) the solar panels with the power electronics. The cabling is separated into three categories: a power harness, a noisy signal harness, and a quiet signal harness. Its interface with the spacecraft subsystems is by means of 46 connectors (Fig. 8).

The upper ring tray is the support for the upper ring cabling, and the eight faces of the tray support the hard-

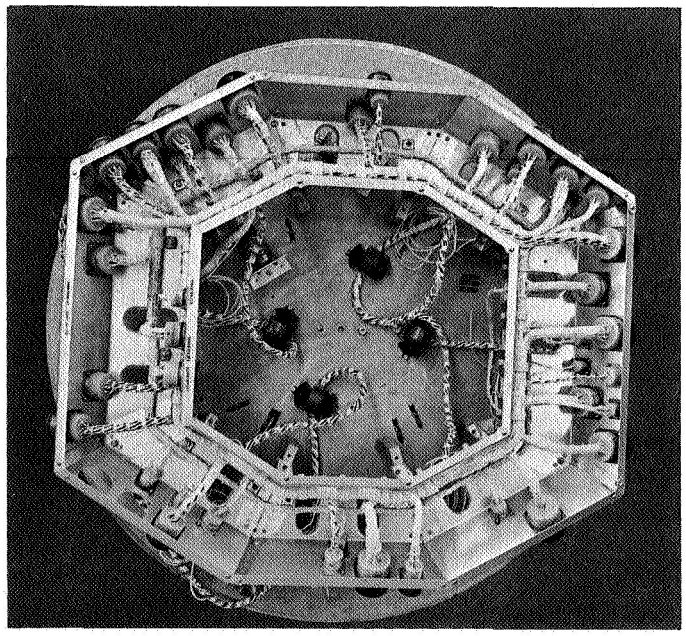

Fig. 8. Upper ring harness and tray on fabrication and handling fixture

mounted interface connectors. Due to the relocation of the attitude-control gas bottles, it was necessary to design a completely new ring harness tray, relative to earlier *Mariner* spacecraft, and substantial improvement was accomplished in the tray structure and attach arrangement with the bus.

The science platform cabling electrically interconnects the various science instruments with their electronics subsystems, and distributes instrument power from the ring tray power harness to the platform instruments. It also contains a pyrotechnic actuation cable for control of the valves for the infrared spectrometer cooling gas bottles and a scan actuation control cable for position control of the science platform.

The platform cable contains approximately 240 separate wires and is configured to offer minimum torsional resistance to the science platform during the scanning mode. The cable design readily permits unrestricted actuation of the platform through its operational limits of 215 deg in the clock mode and 69 deg in the cone mode.

The size of the science platform and the maximum excursions of the science instruments in the various scan positions created several new design problems. It became necessary to reduce the size of the lower ring harness and its mode of attachment. The electronic assembly harness supports and mounting brackets were required to be redesigned and the lower portion relocated to provide adequate clearance for the platform-mounted instruments. As a result of the inaccessibility of the lower electronic assemblies cable brackets, which normally carry the direct access connectors for the operational support equipment, and the necessity for providing greater platform clearance, the direct access connectors had to be moved to the upper brackets. In turn, this required relocation of the pyrotechnic harness connectors and the scan control connector to bay I, and the science to platform connectors to bay VII. In accomplishing these changes, a congested cabling area was created in the immediate vicinity of the upper ring.

The purpose of the lower ring harness (Fig. 9) is to interconnect the spacecraft subsystems to the secondary sun sensors, motion sensors, separation-initiated timer, pyrotechnic arming switch, and the inflight disconnects between the spacecraft and the spacecraft adapter. The inflight disconnects carry all the umbilical functions plus several systems functions that are actuated upon separation of the spacecraft from the *Centaur*.

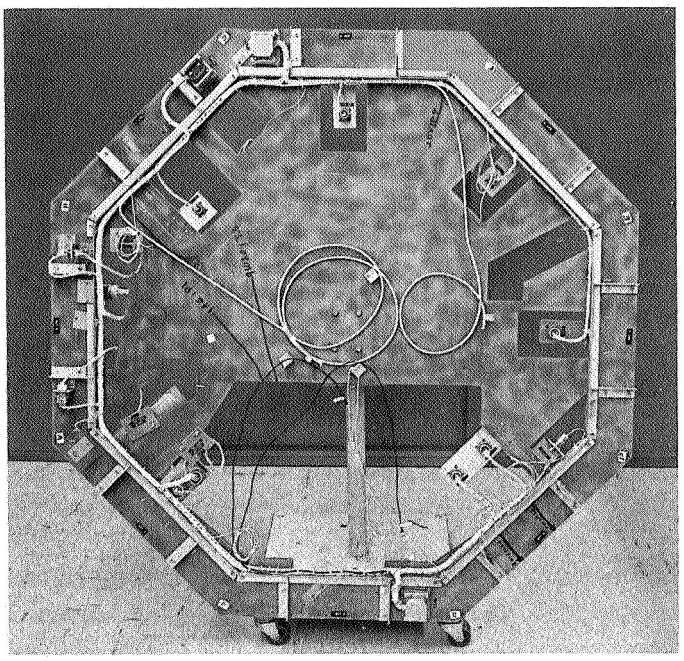

Fig. 9. Lower ring harness on fabrication fixture

In previous *Mariner* spacecraft of 1964 and 1967 vintage, the umbilical functions were carried through an umbilical connector approximately 4 in. in diameter, which was reached by entry through the spacecraft shroud. On the *Mariner* Mars 1969 spacecraft, the functions are routed through two inflight disconnect connectors plus a third connector that accommodates two coaxial RF cables.

This arrangement allowed three important accomplishments: (1) it essentially doubled the number of available contacts from 69 to 126, of which 102 contacts are used; (2) it attained a weight reduction of well over 50%; and (3) it provided a very substantial cost savings.

The lower ring harness was significantly reduced in volume by moving some functions from the lower ring to the upper ring, and a new method of installation was devised. By tying the harness to the inboard surface of the lower octagon structure through nylon pillow blocks, the harness was held close to the structure for improved support, and the time required for installing the harness was reduced to approximately 2 h.

The spacecraft adapter cable (Fig. 10) carries all the spacecraft umbilical functions from the spacecraft to the adapter island. The harness is hard-mounted to the adapter island and mates with cables routed from the *Centaur* umbilical connectors. The adapter island is also the junction for the separation pyrotechnic harness, adapter accelerometers, band tension monitors, and TV stimuli lights. At the "upper" end of the cable, the connectors are mounted to floating attach brackets and mate with the spacecraft inflight connectors.

2. Television Camera Assembly: Mechanical Design

a. Introduction. The *Mariner* Mars 1969 spacecraft utilizes two TV camera assemblies that differ in angular resolution by a factor of 10. The cameras use identical head subassemblies and different optical subassemblies. The camera A optics (wide-angle) subassembly consists of a multi-element $f/3.5$ refracting lens with a 2.0-in. focal length and a combination filter/shutter wheel mechanism. The shutter is a rotating-disk type with an appropriate filter introduced into the light path by the application of a current pulse. Camera A will take wide-angle pictures of Mars in two or three spectral bands. The camera B optics (narrow-angle) subassembly consists of an $f/2.5$ catadioptric telescope with a 20-in. focal length and a solenoid-operated blade-type shutter with no filters.

The identical camera head subassemblies consist of a vidicon photo-sensor, the mechanical and electronic components necessary to image a scene on the vidicon tube photo surface, and the signal conditioners required for transmission to the TV electronics that are located within the octagonal portion of the spacecraft. The camera A head subassembly is fastened directly to the spacecraft platform structure, and the camera head chassis supports the optics assembly (Fig. 11). The camera B optics subassembly (Fig. 12) is larger than the camera head subassembly and is designed to support the camera head. Each camera head contains a vidicon tube surrounded by deflection and focus coils, the preamplifier section, a high-voltage power supply, a bank of capacitors for the shutter solenoids, and miscellaneous electronic control circuits. An exploded view of the assembly is shown in Fig. 13. The high-voltage elements of the camera heads were designed to meet the requirements of M69-220-2 and operate in the critical pressure region.

A major difference between the *Mariner* Mars 1964 vidicon system and the *Mariner* Mars 1969 system is in the vidicon tube and deflection system. The *Mariner* Mars 1964 camera utilized electrostatic deflection plates within the vidicon tube envelope to obtain electron beam control, while the *Mariner* Mars 1969 vidicon system uses bulky magnetic coils external to the tube envelope to

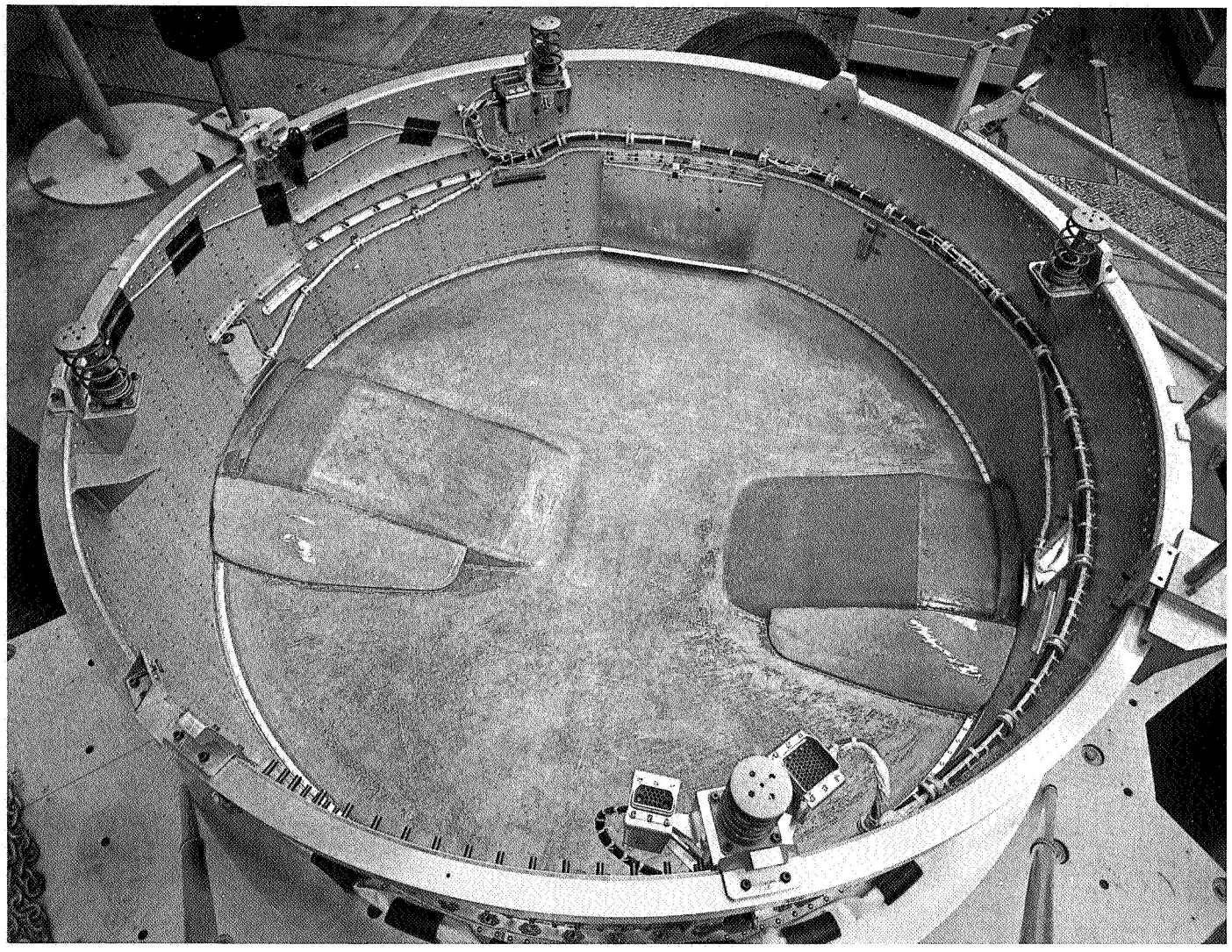

Fig. 10. Spacecraft adapter cable

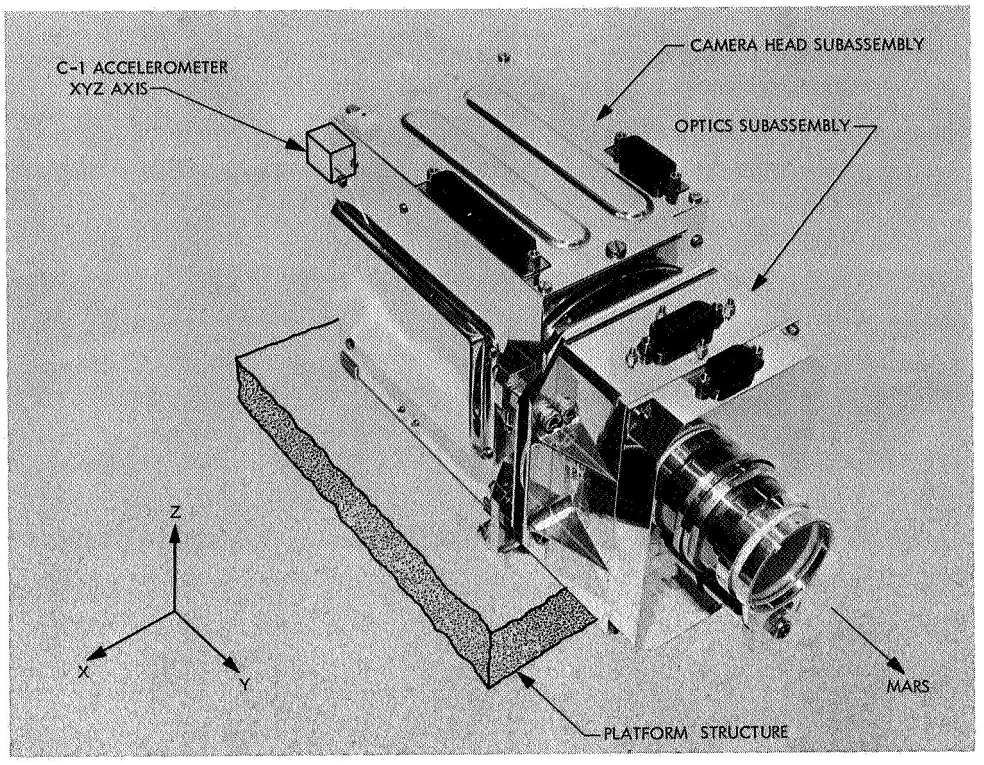

Fig. 11. Wide-angle camera assembly

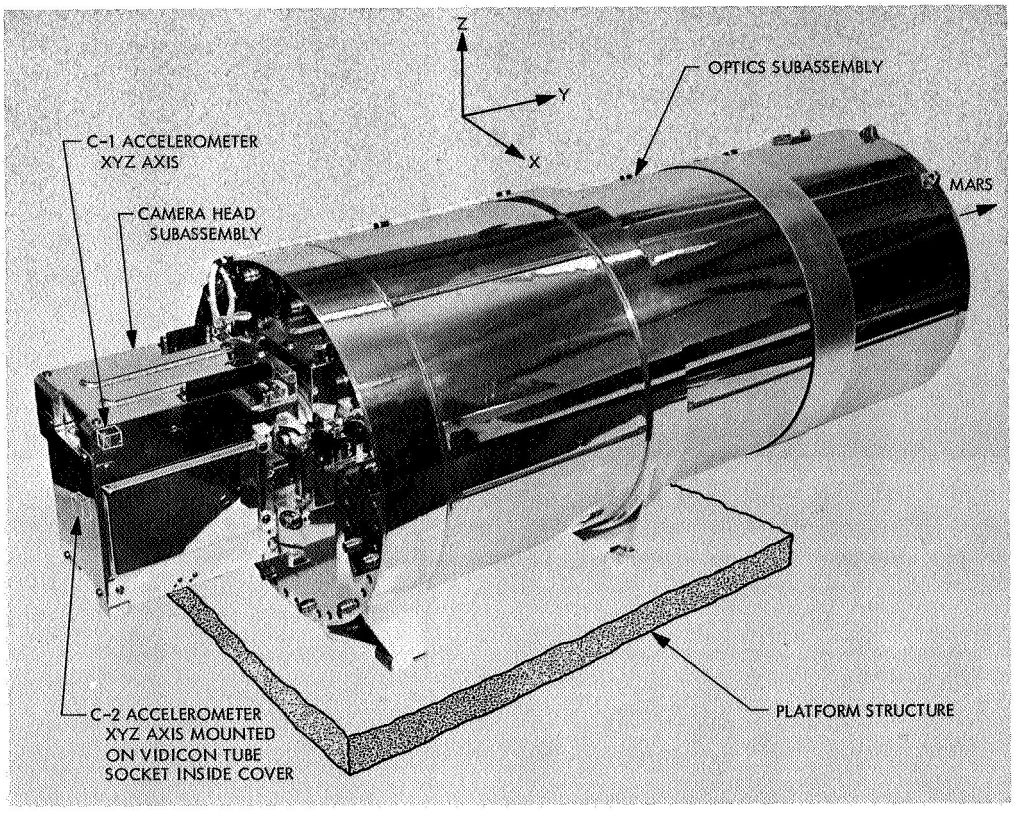

Fig. 12. Narrow-angle camera assembly

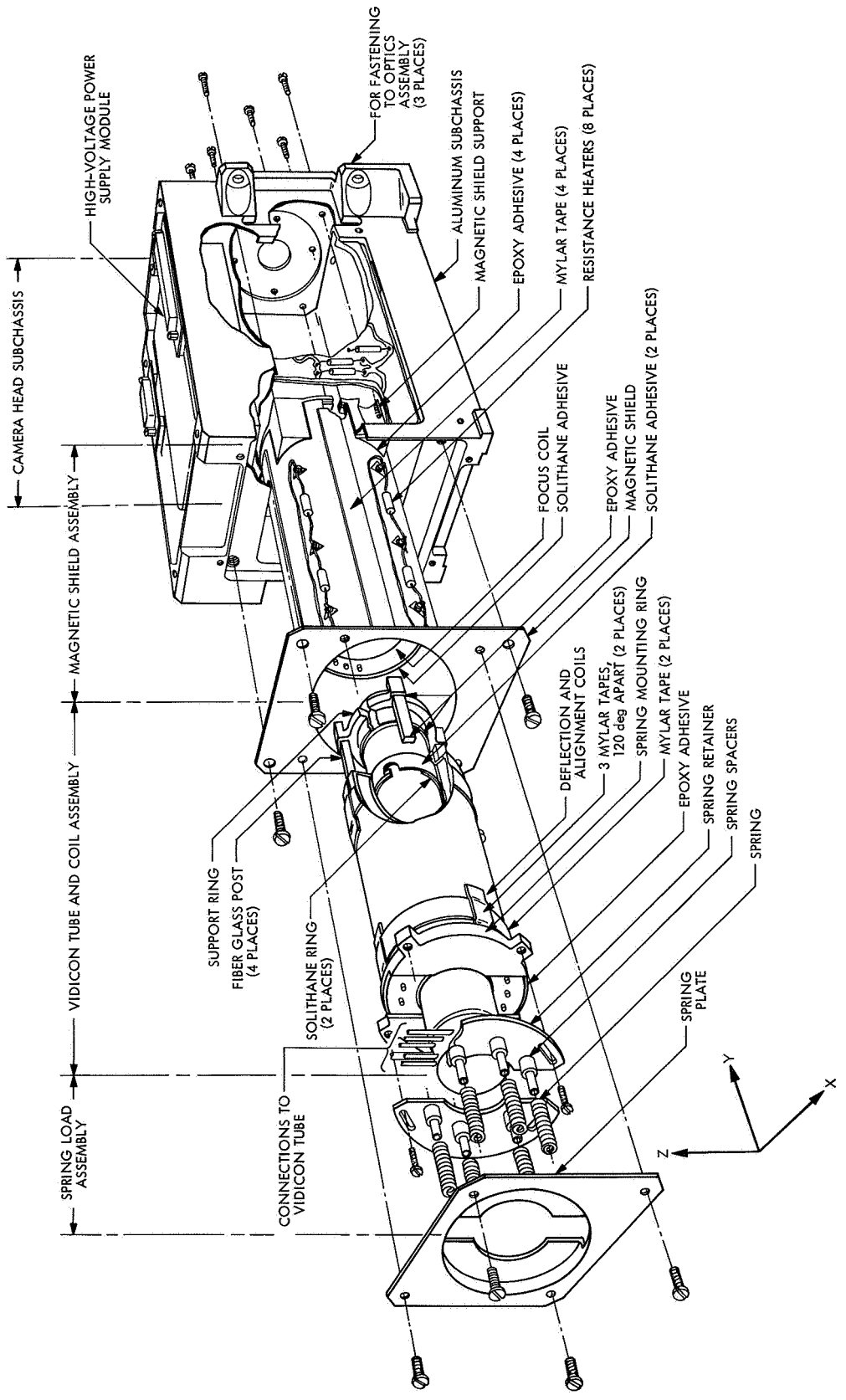

Fig. 13. Television camera head, exploded view

obtain more precise electron beam control. Another significant difference is that the *Mariner* Mars 1969 design is more rugged in order to meet the more severe environmental requirements.

b. Camera head attachment. The camera B subchassis is not mounted directly to the platform like camera A but is cantilevered from the B optics assembly through the same three rigid mounting bosses used to support the optics on camera A. A fourth semi-rigid mounting leg is added to stiffen and dampen the cantilevered load of the common head on the optics assembly. All bolting to the optics is done through mating sets of spherical washers to prevent strain of the optical structure under steady-state conditions.

The three rigid mounting legs are also designed to allow for focus adjustment of the optical system. Each leg may be adjusted to any point within a range of ± 0.10 in. The capability to adjust each leg independently also permitted corrections to be made for focal plane tilt.

The fourth semi-rigid leg is not adjustable so a special length spacer is made to fit each assembly after the rigid legs are fastened at the proper focus position. The semi-rigid leg is made up of two aluminum channels that are nested as shown in Fig. 14 and a Solithane material is applied within the 0.01-in. space between the legs of the channels. The outer channel is fastened to the optics structure, while the inner channel is attached to the camera head subchassis. The viscoelastic properties of the Solithane material improve the dynamic response at resonance without stressing the sensitive optical mount under steady-state conditions. Thus, the constraint-free advantages of a rigid three-point mount are not compromised by the addition of the semi-rigid leg.

c. Camera head subassembly configuration. The subchassis is machined from 6061-T6 aluminum with the outside surface polished to a mirror finish. A large deep hole is machined in the center to accept the magnetic shield assembly and the vidicon tube and coil assembly (Fig. 13). Compartments are located around the four sides

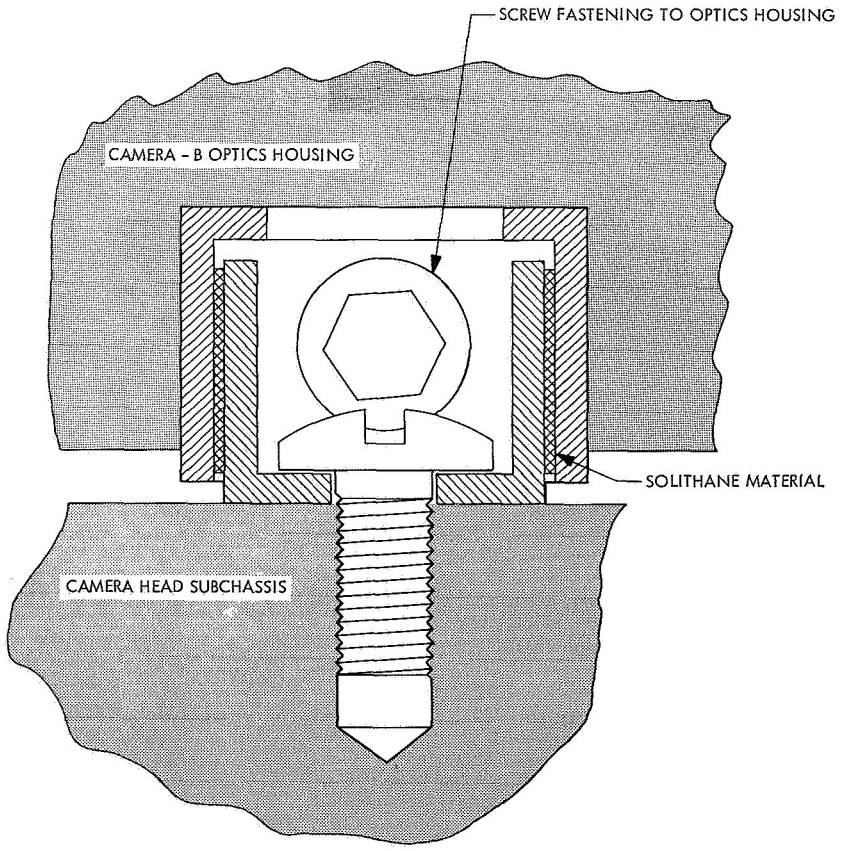

Fig. 14. Cross section of semi-rigid leg

of the subchassis for mounting the preamplifier stages, the high-voltage power supply, the shutter's capacitor bank, and other circuitry. Provisions for fastening the magnetic shield, the semi-rigid leg, the temperature transducer, and the polished aluminum covers are structurally integrated into the walls of the compartments.

The first stage of the preamplifier section is laid out at the target end of the vidicon tube to minimize the length of the video target lead that connects the vidicon tube face plate with the preamplifier input. This wire is fed through a hole in the subchassis as the vidicon tube assembly is inserted into the focus coil.

The position of camera A on the platform between two other instruments determined the connector compartment location. This compartment was also chosen to house the high-voltage power supply in order to isolate the 400-Hz circuitry. There are three major elements in the high-voltage circuitry: (1) the high-voltage transformer and associated components, (2) the high-voltage wire connecting the high-voltage power supply module and vidicon tube, and (3) the tube pin connections. They are designed to operate within the critical pressure region with no arcing or corona. The high-voltage requirements for both camera A and B high-voltage circuits are met by using identical power supply modules that are located in each camera head to provide minimum high-voltage transmission distance to the vidicon tube socket. The high-voltage module consists of a high-voltage transformer and associated components that are encapsulated and then embedded in an epoxy fiber glass box. The transformer windings and interconnection are designed to minimize voltage gradients between conductors. The final high-voltage wire connections to the vidicon tube are soldered to terminal connections on the high-voltage module or the vidicon tube pins and then embedded in Solithane. The high-voltage wire is polyolefin-insulated, which was selected because it forms a strong bond with the Solithane embedment material.

d. Vidicon tube and deflection components. The target end of the vidicon tube is fastened to a stainless-steel support ring with semi-rigid epoxy adhesive. A precision bonding fixture is used to locate the support ring relative to (1) the orientation of the vidicon tube's mask, (2) the perpendicularity of the mounting feet with the tube axis, and (3) the concentricity of the tube and ring. This fixture also recesses the fragile target face 0.003 in. below the ring's supporting feet so that the metal feet, not the glass, will contact the subchassis at assembly.

The vidicon tube is bonded to the deflection coil at each end with a band of flexible Solithane adhesive. Four fiberglass posts are bonded between the support ring and the deflection coil with epoxy adhesive. These posts serve to transmit the 82-lb spring load forces applied to the deflection coil directly to the subchassis and, thus, isolate the glass vidicon tube from the spring load forces (Figs. 13 and 15).

Electrical connections to the vidicon tube are pigtail wires that have been soldered to the tube pins and encapsulated. Connections to the deflection components are made at forked terminals on the coil assemblies. A set of resistance heaters is located on the focus coil shield to provide a constant power dissipation within the instrument even when its electronics is turned off during the cruise mode.

The adjustment of the vidicon tube relative to the deflection coil is provided by snugly fitting rings between the vidicon tube and the deflection coil. These rings are selected to allow a snug fit so that a precise adjustment can be made and retained by friction (Fig. 13). The correct position is fixed by spot bonding the adjacent parts in four places, thus allowing the removal of the vidicon tube and coil assembly from the camera head without loss of alignment. The rings also serve as dams during bonding and constrain the semi-rigid adhesive to a 0.5-in.-long band at the extreme ends of the deflection coil. The final adhesive bonding operation (fixing the coil and tube position) is done outside the camera head.

The focus coil position is also adjustable during the alignment of the vidicon tube. A snug fit between

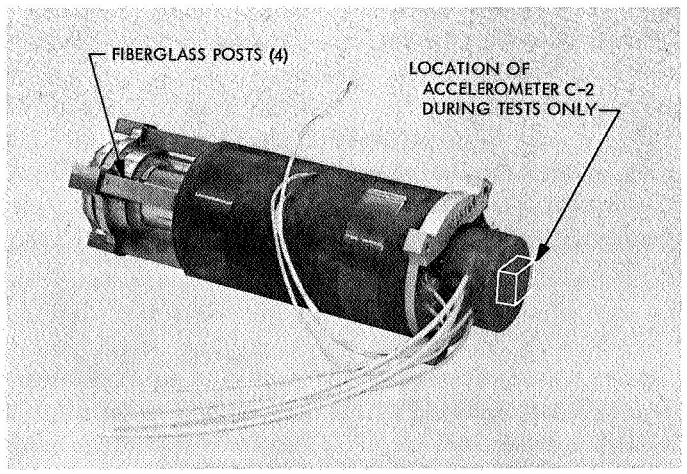

Fig. 15. Vidicon tube and deflection coil assembly

the magnetic shield and the focus coil is obtained by compressing four pieces of Teflon sleeving in the annulus between shield and coil. The sleeving is located at 90-deg intervals along the length of the focus coil. These pieces of sleeving center the coil within the shield and provide the desired fit that allows adjustment and temporary retention of position. The aligned position is also fixed by spot bonding in order that it can be removed from the camera head and bonded permanently with a semi-rigid adhesive.

The deflection coil and tube assembly is in turn inserted into the focus coil. Adhesive Mylar tape is used to build up an interference fit at three pads 120 deg apart at each end of the deflector coil. The interference fit at each pad is built up using combinations of three Mylar tape thicknesses: 0.0015, 0.003, and 0.006 in.

An insertion fixture is fastened to the deflection coil to facilitate grasping the vidicon tube assembly and measuring forces during installation into the focus coil. The pads at the target end are built up until a breakaway static friction force of 30 lb is obtained. The socket end pads are then built up to cause an additional 40 lb of insertion force. With all pads in place, the total insertion force is 70 lb.

The focus coil is bonded into a magnetic shield that is inserted into the camera head subchassis. Strips of Mylar tape are applied on the shield to cause an interference fit between shield and subchassis and, thus, structurally integrate the 1.5-lb assembly into the subchassis. Four fasteners are provided at each end of the magnetic shield assembly to attach it to the camera head subchassis.

The structural aspects of the vidicon supporting system are completed with the application of the spring load assembly that act in the Y axis. Six springs are used to apply a total force of 82 lb to the deflection coil and, thus, prevent the thermal expansion forces from affecting the critical face plate location. The springs also supplement four screws that hold the vidicon tube support ring to the front of the subchassis.

e. Camera A dynamic response. The worst overall dynamic characteristics of the camera A assembly were due to X-axis inputs (Fig. 11) that resulted in broad resonances between 450 and 650 Hz. Over this range measurements made in the X axis with type-approval-level inputs were 130 g peak at the C-1 location. The corresponding response on the tube socket location C-2 was 1.2 times greater. The dynamic characteristics due to Y- and Z-axis inputs were 25 to 40% lower at 450 Hz, but showed resonances up to 1000 Hz. The tube socket response during Y- and Z-axis inputs was approximately 0.85 to 1.4 times the subchassis inputs at resonant peaks.

f. Camera B dynamic response. Because the optics assembly supports the camera head in the camera B configuration, the overall dynamic characteristic at the head can be separated into two distinct band of frequencies. The low-frequency band up to 425 Hz is controlled by the optics configuration, because the camera head has a transmissibility of 1 (rigid body response) over this frequency range; within the frequency range of 425 to 2000 Hz, the overall dynamic response of the camera assembly is controlled by the interaction of varying transmissibilities within both the camera head and the optics assemblies. The major resonances of the camera head and the optics assembly do not occur at the same frequencies; therefore, extremely large overall resonances do not build up.

The dynamic characteristics of the camera head alone were determined during development testing on a fixture that simulated the camera B interface as a rigid plate. The camera head accelerometer locations on the subchassis were the same (C-1, Fig. 12) as were used for the camera B assembly development testing. Results of vibration testing at 12.6-g peak inputs in the X, Y, and Z axes showed first resonance in the X axis at 500 Hz and the Z axis at 450 Hz. The next highest response, 140 g peak at 450 Hz, was in the Z axis and was due to Z-axis inputs. The next higher response, 120 g peak at 600 Hz, was in the X axis and was due to X-axis inputs; at 500 Hz, the Z-axis response was 48 g peak. The Y-axis response was 20 g peak at 500 Hz and 50 g peak at 1100 Hz, all due to Y-axis inputs.

The dynamic characteristics of the camera head mounted on the optics assembly were most severe with Z-axis inputs. During Z-axis flight-acceptance-level (FA) vibration tests, the response at C-1 was 60 g peak at 220 Hz, 120 g peak at 300 Hz, and 30 g peak in the 400- to 1000-Hz range. The response at C-1 to FA-level inputs in the X and Y axes was similar to the Z-axis response in frequency, but was less in average magnitude at the resonance frequencies by 30%. The vibration levels on the vidicon tube socket C-2 were approximately 1.3 times greater than those on the camera head at C-1.

3. Heat Pipes

Heat pipes were to be used on the *Mariner* Mars 1969 to lower the temperature of the radio power amplifier and its associated power supply by more efficiently distributing its heat over the available radiator (the face of bay VI). Analytical predictions indicated that a 30°F temperature reduction in the radio power amplifier could be realized, which would give enough additional temperature margin to double the nominal 10-W RF output from the spacecraft.

A heat pipe is a very simple device in principle and construction. It consists of a sealed tube that contains only a fluid, its vapor, and a wick. When heat is applied at one part of the tube, the fluid vaporizes and the heat is transported to any colder part of the tube where the vapor condenses. The wick is a simple pump which, under weightless conditions, assures that the fluid from the condenser area is resupplied to the evaporator area.

The most conservative design alternatives were selected, resulting in the design shown in Figs. 16 and 17. The tube was 15.5 in. long with an outside diameter of 7/16 in. and was lined with a 100-mesh screen wick. The tube, its end fittings, and the screen were made of 304 stainless steel and the fluid was chemically pure water. The tube was attached to the face of bay VI with an aluminum housing. The interface between the tube and the bay face was filled with powdered silver in a silicone binder (RTV-11). A heat pipe assembly was located over each of the two radio transmitters. The skewed position of the lower tube in Fig. 17 was necessary to avoid the mounting screws of some of the radio receiver assemblies.

Unfortunately, this design did not reduce the temperature of the radio as predicted. An early test using a mockup radio resulted in a 17°F reduction in the radio temperature, but later tests using working radio assemblies resulted in only a 5°F reduction. This performance was judged to be insufficient and the pipes were removed from the spacecraft design. Fortunately, the radio temperatures were not as high as expected and the high-power transmitting mode was possible even without the heat pipes.

Although the heat pipes are no longer used on the *Mariner* Mars 1969, several observations may be of interest:

Inaccurate analysis. Although the best analytical tools available were used, the predicted radio temperatures either with or without the heat pipes were 20 to 30°F in error. It is believed that this was due to inaccurate conductivity information and/or power estimates. In the analysis that included the heat pipes, the isothermal node sizes were probably too large.

Performance degradation. The stainless-steel, "water" heat pipe was difficult to load without contamination by air and, even if correctly loaded, the performance would degrade with time. The degradation was attributed to trace amounts of free iron in the stainless steel combining with the oxygen in the water, thus releasing hydrogen as a noncondensable gas. This ultimately reduced the effective working length of the pipe. By changing the working fluid from water to ammonia, an easily filled nondegrading pipe was produced. Fortunately, the temperatures and power levels existing in this application were near the crossover point in performance between water and ammonia. At higher temperatures or power levels this substitution would not have been as desirable as a change in the tube and wick material. Preliminary results from a long-term test started during August 1968 indicate that degradation in the ammonia-filled pipe has not occurred.

Design consideration. The most important lesson to be learned was not how to make a good heat pipe, but how it should be incorporated into the design of the radio. Within the constraints imposed, the best design possible was not good enough. To illustrate, the radio power amplifier can be considered as a hot spot that must be cooled in two parallel ways. The design without a heat pipe was to spread the heat as quickly as possible to reduce the flux per unit area, hence the temperature differences across the bolted joints between it and the radiator. By the time the heat reached the radiating surface, it was spread over an area of approximately 25 or 30 in.^{2} A tube-type heat pipe could pick up only a small part of this heat and transfer it away via the fluid.

On the other hand, a larger plate-type heat pipe which could gather the heat and transport it away would be a radiation shield in the event that the pipe failed to work. Another alternative was to build the heat pipe into the hot spot before it was spread. This, however, required that the transmitting tube be modified or that the heat pipe be shaped around it. Either of these alternatives would have compromised the qualification history of the transmitting tube.

Thus, it can be concluded that a heat pipe can be used more effectively if the part to be cooled (or heated) can

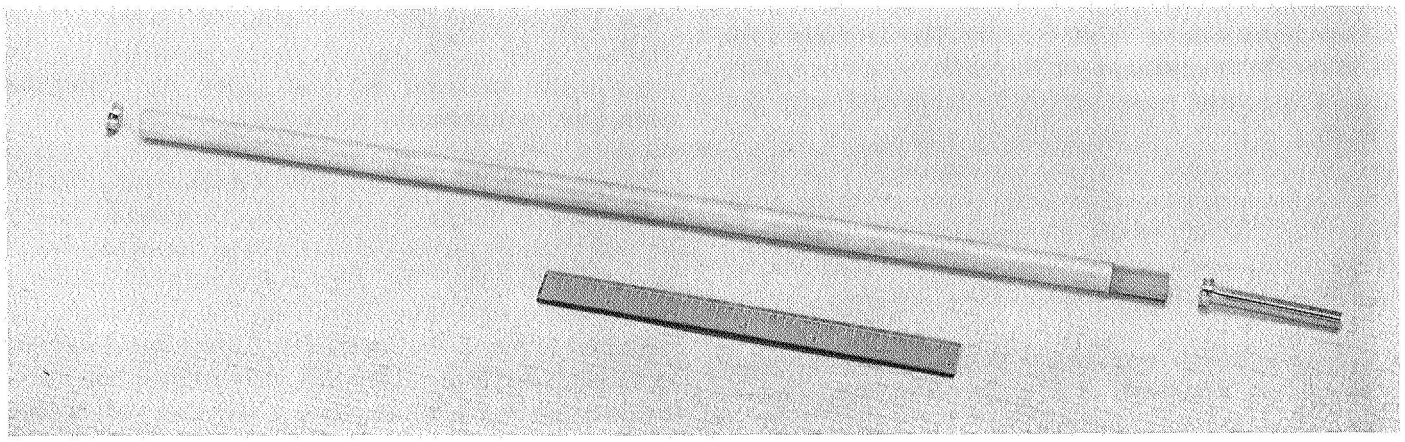

Fig. 16. Heat pipe configuration

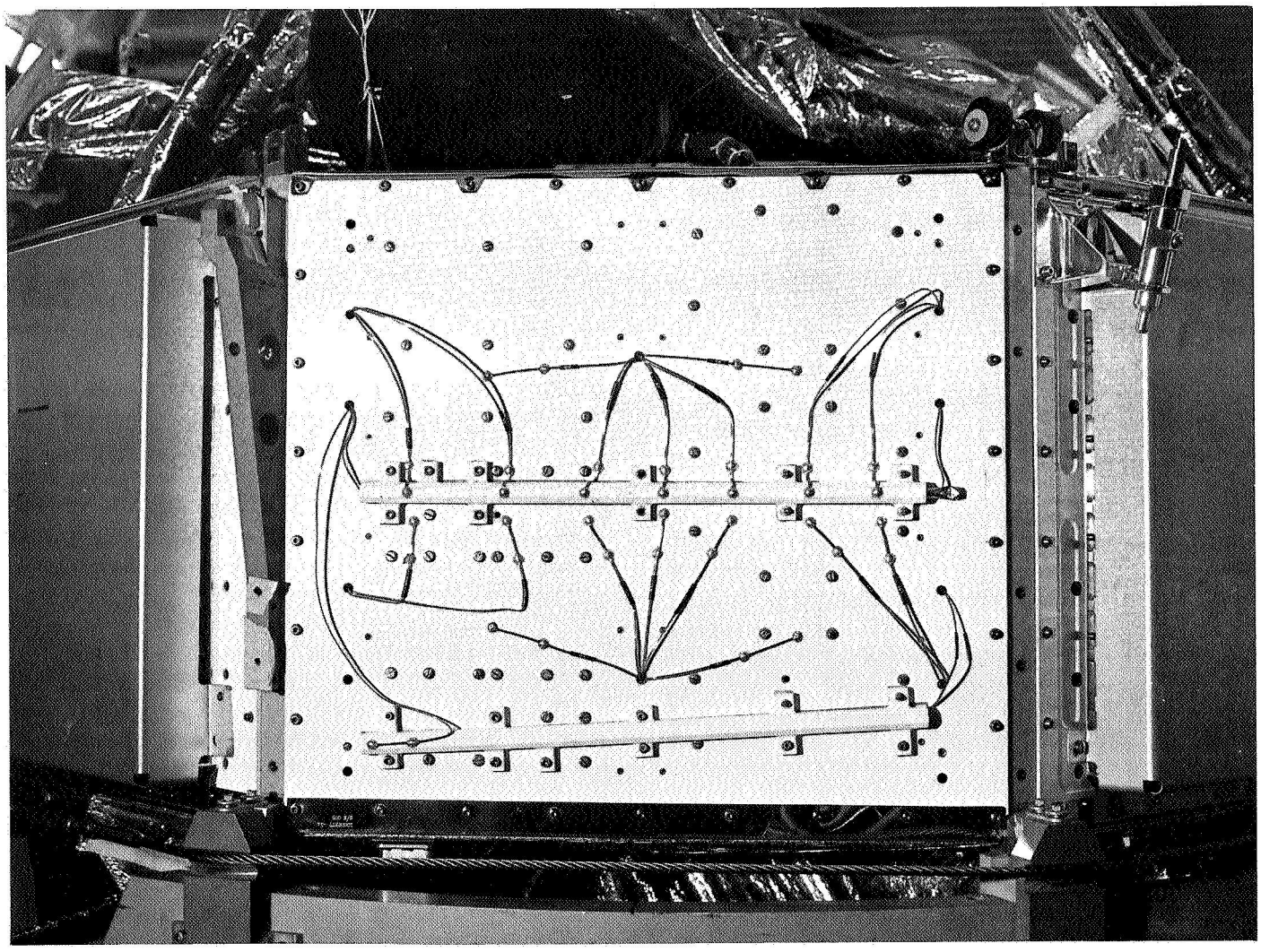

Fig. 17. Heat pipe assembly attached to bay VI

be influenced at the very early stage of its design. In some particular applications, it may be necessary to design a subsystem around the heat pipe.

E. Guidance and Control

1. Attitude-Control Subsystem

a. Introduction. A series of special tests was performed with the attitude-control subsystem to experimentally verify the compatibility of the derived-rate system. The tests were categorized into two parts: (1) verification and study of closed-loop system acquisitions, and (2) determination of the capture threshold of the system when it is in derived-rate limit-cycle control and is subjected to acceleration disturbances.

The gyro and Canopus sensor packages were mounted on a single-axis table (Fig. 18), with the gyro mounted so that it sensed the rate input of the table. A star simulator (Canopus) was mounted off of the table to provide an input to the Canopus sensor.

b. Sensor characteristics. Operating Canopus sensor characteristics were obtained by commanding the gyro *off* (DC-40) and driving the single-axis table through the simulated star and observing the Canopus sensor outputs. The results are depicted in Fig. 19 and are summarized as follows:

Roll error scale factor: −3.75 V/deg (specification −3.4 to −4.6 V/deg)

Saturated roll error: −13 V (specification −12 to −14 V)

Acquisition gate:

on_{ccw} = +5.2-deg roll

off_{ccw} = −6.8-deg roll

off_{cw} = +7.7-deg roll

c. Acquisitions. A normal acquisition with a worst-case gas system (half) is shown in Fig. 20. The half gas system results in an acceleration constant of 0.0129 deg/s². The spacecraft (table) starts with an initial position of 10.8 deg from Canopus and, upon application of power to the Canopus sensor, it generates a saturated roll error signal that results in a roll search rate of −0.21 deg/s. After acquisition the gyro is turned off in a normal manner.

After the gyro has run down, a roll override command (DC-21) is issued to reject the acquired star. The spacecraft (table) roll rate increases significantly beyond the desired roll rate during the period that the gyro is running up to synchronous speed. After achieving synchronous operation the search rate is reduced to the normal −0.21-deg/s rate.

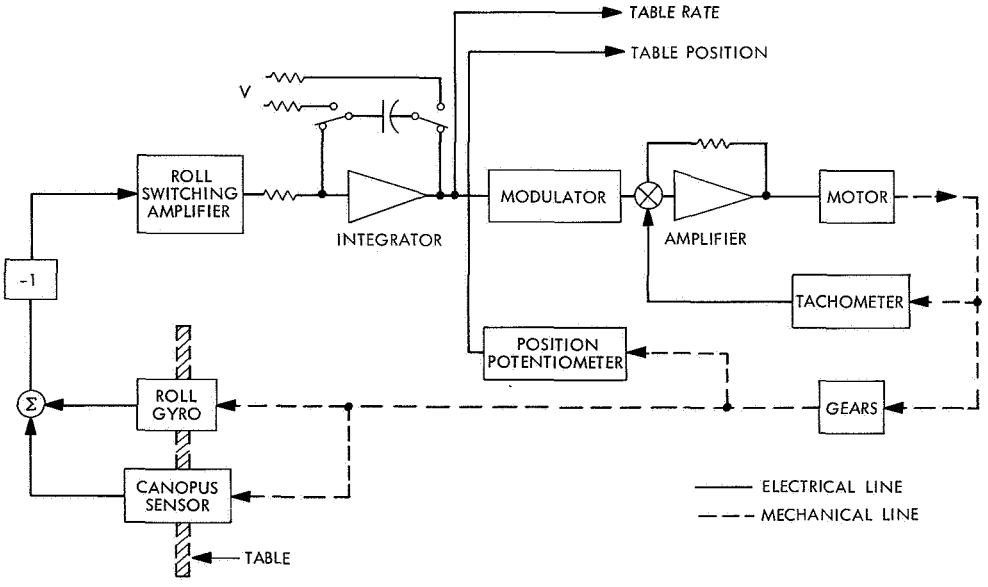

Fig. 18. Single-axis simulation

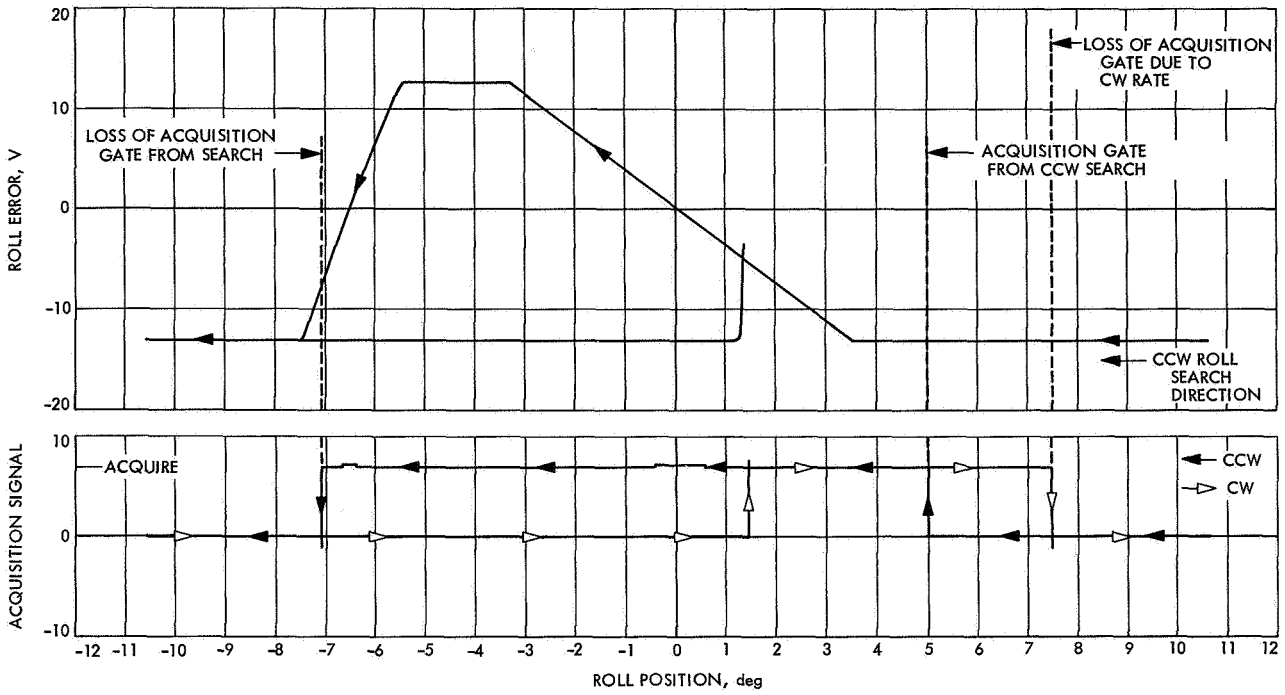

Fig. 19. Canopus sensor characteristics

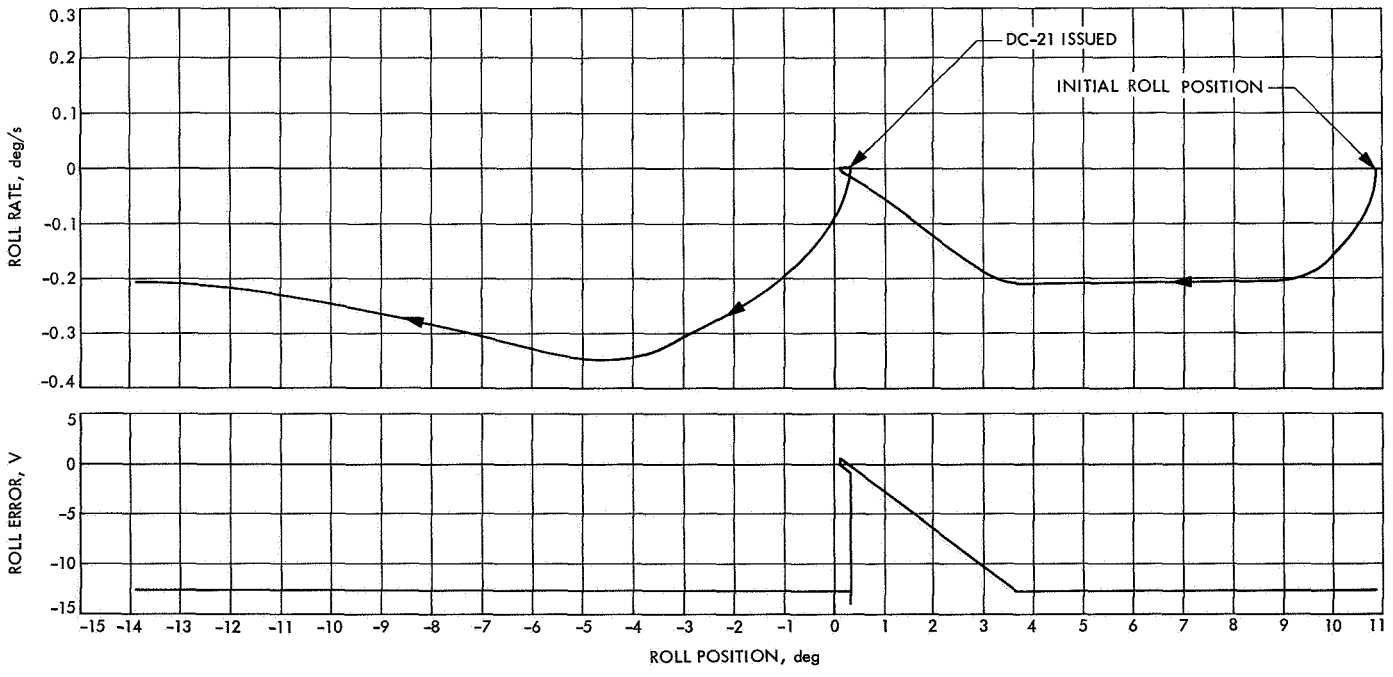

Fig. 20. Canopus acquisition with gyro-rate feedback (half gas system)

A derived-rate acquisition with the gyro inhibited (DC-40) and the Canopus sensor brightness gate logic inhibited (DC-15) is shown in Fig. 21. The figure indicates the maximum angular displacement in roll from which a star can be acquired with a full gas system while on derived-rate feedback. The limiting factor in establishing the limit is the length of time that the ccw roll valve is on. If the ccw roll valve is on in excess of 30 s, the roll search inhibit circuit actuates and disables the roll error (position) input to the roll switching amplifier. The roll search inhibit circuit can be reset with a roll override command (DC-21).

d. Disturbance torques. The maximum velocity from which the attitude-control roll-axis control system can recover is shown in Fig. 22 for a half gas system and Fig. 23 for a full gas system. The capture threshold is 0.36 deg/s for the half gas system and 0.50 deg/s for the full gas system. The limiting factors in establishing the capture threshold are primarily that the ccw roll valve *on* time shall not exceed 30 s, and that the star shall not exceed the acquisition gate limits during the transient reacquisition. A digital computer simulation of the roll axis in a derived-rate feedback mode was utilized to analytically determine the capture threshold. The results

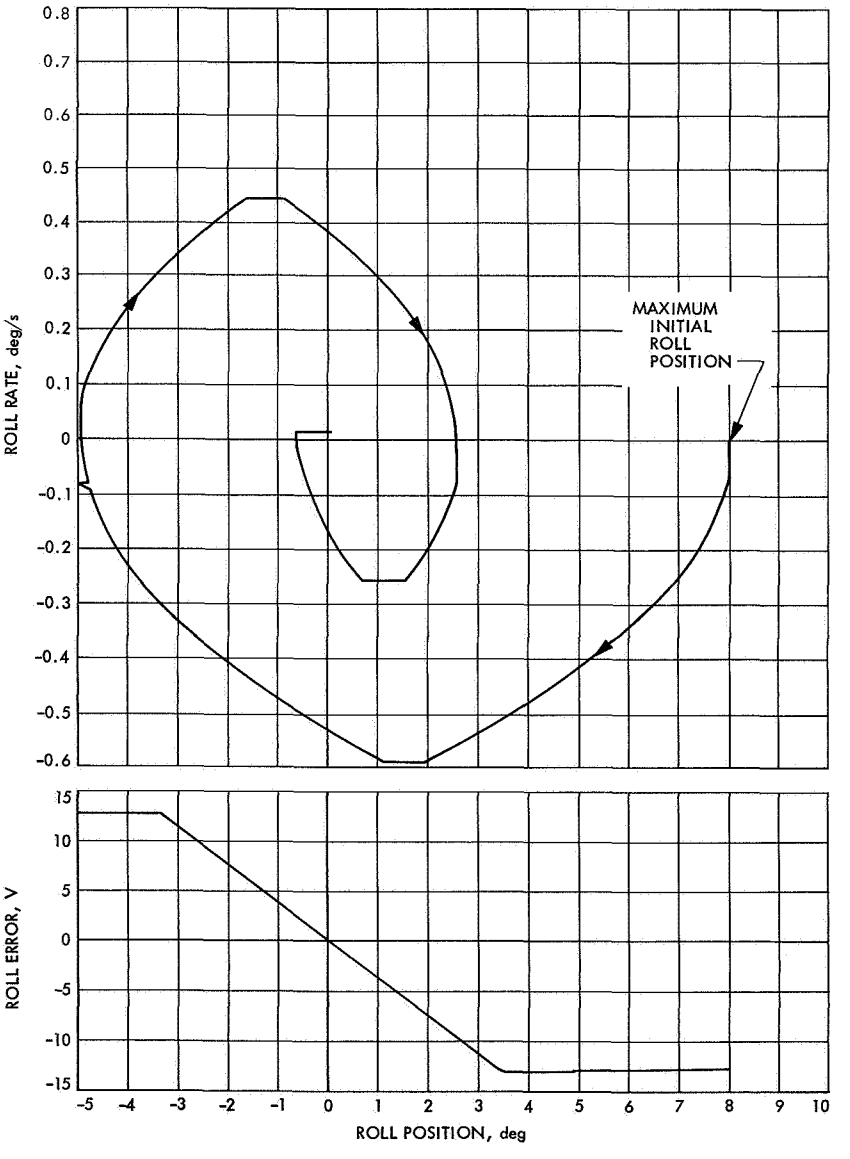

Fig. 21. Canopus acquisition with derived-rate feedback (full gas system)

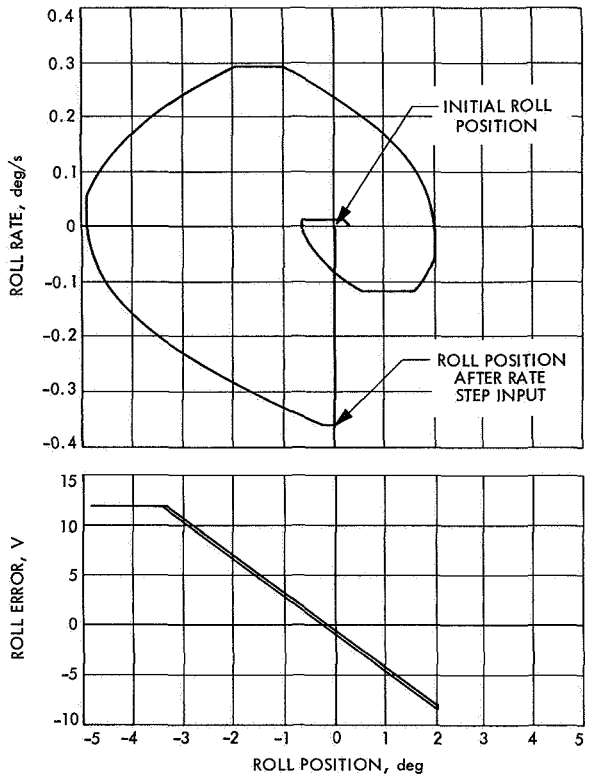

Fig. 22. Half gas system disturbance torque

are shown in Fig. 24. The computer simulation results compare favorably with the real simulation results.

The capture threshold of the *Mariner* Mars 1969 system is much higher than that of previously flown derived-rate attitude-control systems. The capture threshold of these systems is given below.

System	Capture threshold, deg/s	Acceleration constant, mrad/s²
Mariner Mars 1969	0.50	0.450
Mariner Mars 1964	0.28	0.450
Ranger Block III	0.30	0.60

e. Special tests. The following special tests were conducted successfully in support of this study:

(1) Acquisitions with a bright earth passing through the field of view before Canopus acquisition.

(2) Sun shutter operation.

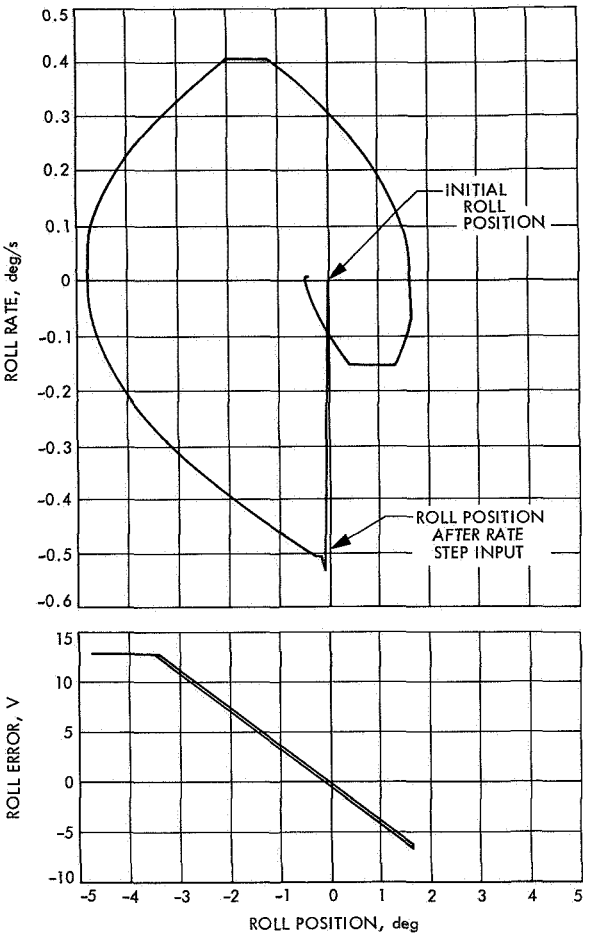

Fig. 23. Full gas system disturbance torque

(3) Acquisition of stars with varying intensity levels to verify operation of the intensity gate limits.

(4) Effect on the system of bright particles. (Generally these bright particles move quite rapidly so that the spacecraft cannot track them. The system operates in a manner such that the control system tries to follow the particle, loses the particle, initiates a Canopus sensor fly-back and sweep that reacquires the star.)

(5) Roll error offset when in the Mars encounter geometry. A special test to observe the effect of a bright Mars disk on the roll error null offset was conducted. With the system locked on the star Canopus, a 100-ft-cd Mars disk was brought within 23 deg (both cw and ccw roll displacements) of Canopus with minor null offsets (increase of approximately 100 mV).

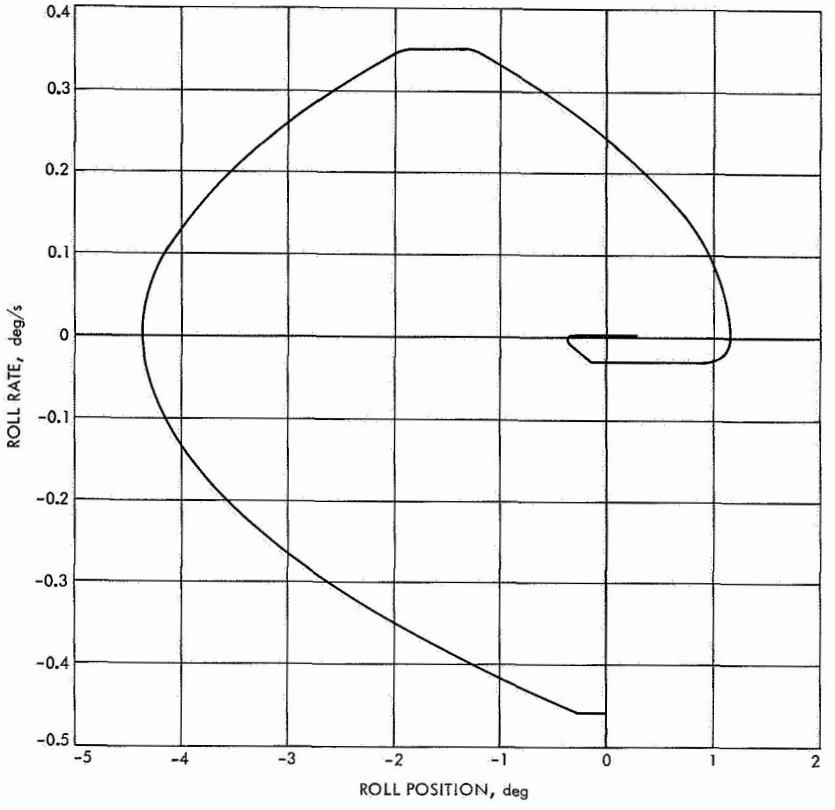

Fig. 24. Computer simulation disturbance torque

2. Sizing Procedures for AC Gas Nozzles To Meet Control Torque Requirements

a. Introduction. One of the major areas of concern in building an attitude-control (AC) gas system is the proper sizing of the gas nozzles to meet spacecraft control torque requirements. On past *Mariner* and *Ranger* missions, this sizing had been done primarily by hand calculations and trial-and-error machining. For *Mariner* Mars 1969 and future use, a computer program was generated that predicts the correct nozzle geometry. Also, test apparatus and procedures were developed to measure steady-state thrust levels under simulated flight conditions. (This test capability was previously nonexistent.) Figure 25 shows a cutaway view of the *Mariner* Mars 1969 valve–nozzle combination. Table 4 lists the *Mariner* Mars 1969 AC thrust requirements (based on zero cross-coupling).

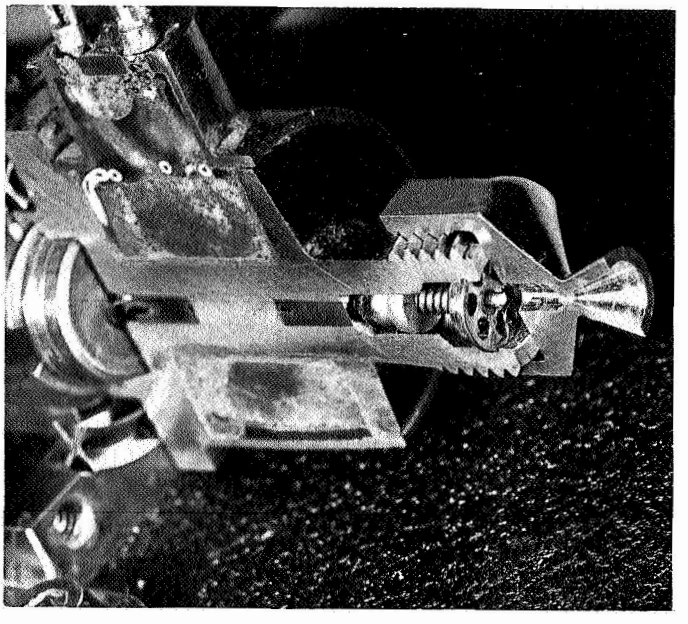

Fig. 25. Cutaway view of valve–nozzle combination

b. Nozzle-sizing computer program. The capabilities of the computer program have been reported in SPS 37-42, Vol. IV, pp. 47–48. Basically, the computer program will calculate the steady-state thrust level produced, taking into account the nozzle thrust losses, for a given set of input conditions. The relevant initial conditions, based on *Mariner* Mars 1969 requirements, as used in this analysis are listed in Table 5. The listed nozzle area ratio and exit half-angle, although not optimum (less by 1–2%),

Table 4. Attitude-control thrust requirements

Maneuver	Principal moment of inertia, slug-ft^2	Control acceleration, rad/s^2	Moment arm, in.	Calculated thrust required, lb
Pitch	$I_{xx} = 129.31$	2.25×10^{-4}	111.7	3.13×10^{-3}
Yaw	$I_{yy} = 131.92$	2.25×10^{-4}	111.7	3.19×10^{-3}
Roll	$I_{zz} = 209.60$	2.25×10^{-4}	111.7	5.43×10^{-3}

were established in this case so that previous nozzle tooling and blueprints could be used. Based on the listed initial conditions, the computer program was set up to output a curve of nozzle throat diameter versus thrust (all other relevant parameters were fixed). This curve (Fig. 26) was then used to pick the proper diameters to meet the flight thrust requirements. Test nozzles, identical to flight nozzles, were then fabricated for test.

Table 5. Initial conditions for nozzle-sizing computer program

Parameter	Value
Valve discharge coefficient	0.3478
Valve ball travel, in.	0.006
Ambient temperature, °C	25
Valve ball diameter, in.	0.188
Valve seat diameter, in.	0.132
Nozzle geometric area ratio	250
Nozzle exit geometry half-angle, deg	25
Ratio of specific heats (nitrogen)	1.4
Nitrogen gas constant, ft-lbf/lbm-°R	55.16
Ambient pressure, psi	0
Valve inlet pressure, psi	15.0
Nozzle throat diameter, in.	Variable; 0.010–0.020

c. Nozzle test procedures and results. Sili-gel molds were made of the fabricated test nozzles. These molds were inspected in an optical comparator to assure that nozzle internal geometry was identical to the print call-outs and computer input data. The nozzles were then tested for steady-state thrust level. The test apparatus

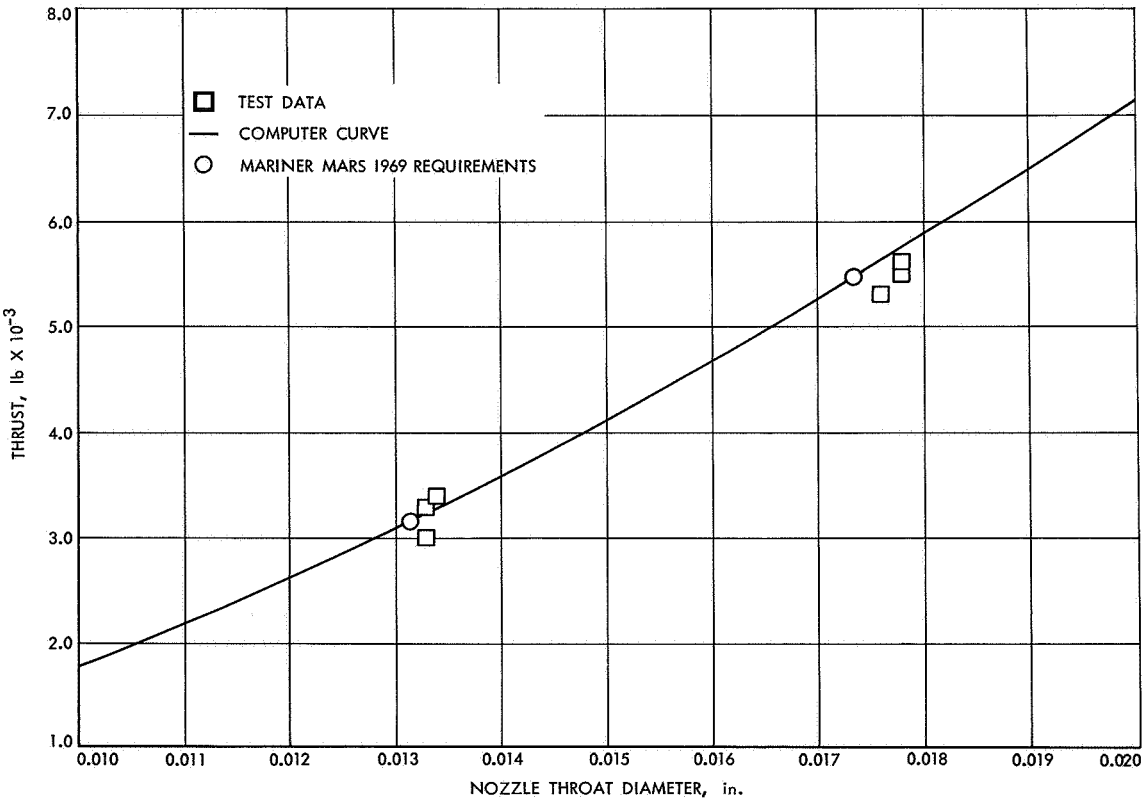

Fig. 26. Net thrust vs throat diameter

and calibration procedures developed are explained in SPS 37-44, Vol. IV, pp. 41–42, and SPS 37-50, Vol. III, pp. 112–114. Basically, the test setup is a vertical cantilever beam (also used as the gas feed line) pinned at the top. The valve and manifold are mounted at the bottom and at right angles to the beam (Fig. 27). Displacement of the beam is measured by a differential transformer pickoff and recorded on a strip chart recorder. Mercury pot damping has also been added. A hanging steel ball is used for calibration. The tests were run in a vacuum chamber (10^{-6} torr) and every attempt was made to duplicate flight conditions. The results of these tests are plotted over the computer data in Fig. 26.

Based on the accuracy of machining and computer predictions, it was concluded that the pitch and yaw thrust requirements could be taken to be identical. The computer run and test data indicate agreement within 5%, which was considered to be of sufficient accuracy since all the data were obtained for an inlet pressure of 15.0 psi. The spacecraft pressure regulation band is 15.0 ± 1.5 psi. Also, the spacecraft inertia data could change slightly before launch.

F. Telecommunications

1. Antenna Assembly

a. Introduction. The design philosophy of the *Mariner* Mars 1969 antenna assembly was to incorporate the *Mariner* Mars 1964 design without any modifications. Deviations were to be considered only if the changes would result in either improved mission performance, enhanced reliability, or reduced cost. As the *Mariner* Mars 1969 program progressed further into the design stages, it became apparent that changes in the *Mariner* Mars 1964 design would be necessary to ensure mission success.

b. Low-gain antenna. The *Mariner* Mars 1964 low-gain antenna (Fig. 28a) consists of a conical spiral feed, a circular waveguide, a set of aperture tuning loops, a cruciform aperture, and a ground plane. A right-hand circularly polarized (RHCP) wave is launched by the conical spiral feed down the waveguide and is then radiated from the cruciform aperture. The spiral feed is capable of launching several different propagation modes. However, the dimensions of the waveguide tube are such

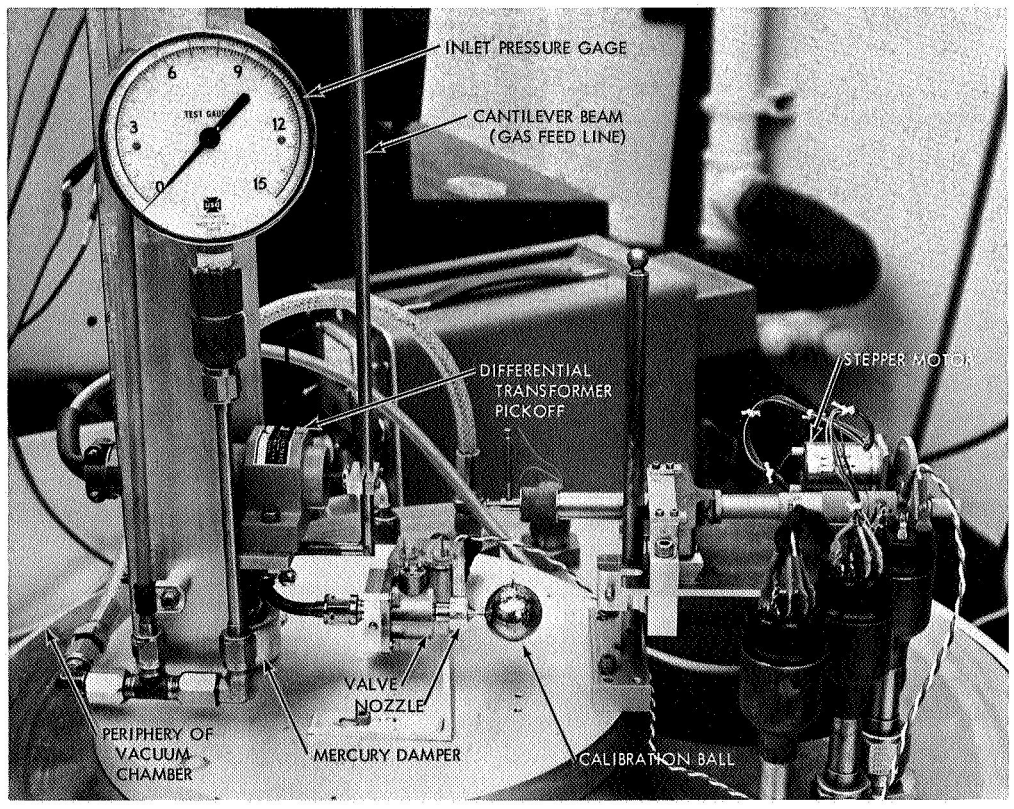

Fig. 27. Thrust measurement stand for nozzle-sizing

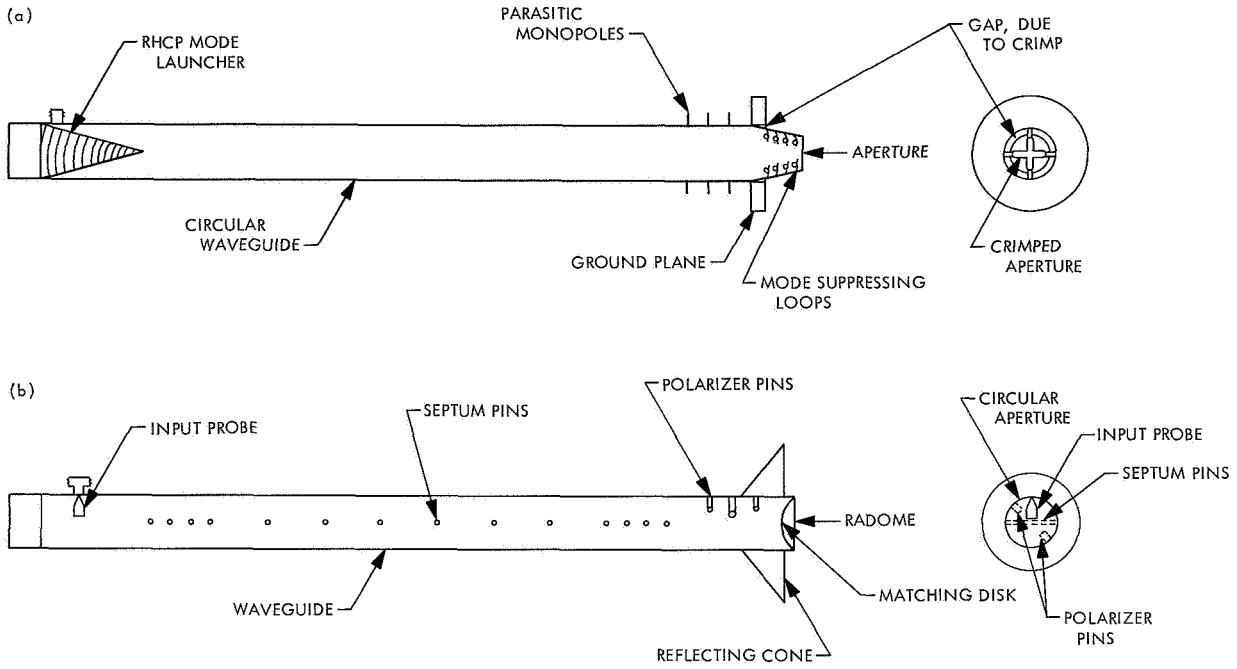

Fig. 28. Low-gain antennas: (a) *Mariner* Mars 1964, (b) *Mariner* Mars 1969

that all modes are rapidly attenuated as the waves travel down the guide except for the dominant transverse electric mode (designated TE_{11}).

Although the *Mariner* Mars 1964 low-gain antenna appeared to be a simple radiating device, many problems were encountered during the design and fabrication of the antenna.

The antenna was found to have a relatively high return loss. This was due to the fact that the cruciform aperture, which was formed by crimping one end of the tube, presented an abrupt discontinuity to the electromagnetic wave. As a result of the discontinuity, the next higher mode (transverse magnetic, TM_{01}) was excited. To suppress the undesired TM_{01} mode, an array of magnetic loops was placed at the discontinuity of the aperture.

The *Mariner* Mars 1964 low-gain antenna also had a high back-radiation problem. This was caused by surface currents traveling freely on the outer surface of the tube. This problem was somewhat relieved by the circular ground plane and the array of capacitive parasitic pins that were placed directly behind the aperture.

Probably the most costly requirement of the *Mariner* Mars 1964 design was the very tight tolerances needed on the conical feed and the waveguide tube diameter. The spiral feed wrap angle, and hence the winding separation, was the most critical parameter for controlling circular polarization. Small deviations in the wrap angle along the cone could produce a large axial ratio that would result in a high polarization loss. A great deal of time and money were expended to produce conical spirals (which are inherently difficult to fabricate) that met the strict tolerance requirements. Even with a reasonably good circularly polarized feed, there was still a requirement for tight tolerances on the waveguide tube diameter. Small deviations in the diameter of a circular waveguide could introduce phase variations in the wave traveling through the guide. The magnitude of the resultant effect depends on the magnitude of the physical deviations and the polarization (and orientation of the electric field relative to the physical deviation) of the wave. The phase shift, due to diameter tolerances, of a circularly polarized wave traveling in a circular waveguide can be expressed as

$$\Delta\phi = \frac{31\,\lambda_g}{a^3}\,\Delta d \text{ deg/in.}$$

where

$\Delta\phi$ = phase difference between the two orthogonal electric vectors

λ_g = waveguide wavelength

a = waveguide radius

Δd = waveguide diameter tolerance

For a nominal guide diameter of 3.875 in., a frequency of 2116 MHz, and a guide diameter tolerance of ± 0.004 in., the phase error will be 0.165 deg/in. If the ± 0.004-in. tolerance exists along the entire *Mariner* Mars 1964 waveguide, a worst-case ellipticity of 2 dB can result. Because of this sensitivity to the waveguide tolerances, it was necessary to place a strict tolerance on the tube dimensions. As a result, many man-hours were spent fabricating and sizing tubes that would meet the critical tolerance requirements.

Because of these problem areas, the variation of the electrical performance from antenna to antenna was large (a variation in gain of about 0.5 dB at 2116 MHz and 1.0 dB at 2298 MHz). The gain and ellipticity versus cone angle and the voltage standing-wave ratio (VSWR) versus frequency of a representative *Mariner* Mars 1964 antenna are shown in Figs. 29, 30, and 31, respectively; data for *Mariner* Mars 1969 are also included for comparison.

After a thorough analysis of the problems and performance of the *Mariner* Mars 1964 low-gain antenna, it was determined that complete redesign of the antenna was necessary. The *Mariner* Mars 1969 low-gain antenna design philosophy and requirements can be summarized as follows:

(1) Linear polarization is to be employed from the waveguide input to the aperture and converted to circular polarization at the aperture. This eliminates the requirement for extremely tight tolerances on the feed and waveguide tube since linear polarization is less susceptible to dimensional changes.

(2) The requirement to receive commands only on the low-gain antenna makes it desirable to have as much gain as possible at Mars encounter. This means maximizing the gain at a 40-deg cone angle (earth is at a 40-deg cone angle during Mars encounter) without degrading the on-axis gain requirement (greater than 5 dB) and a -10-dB minimum-gain requirement at a 90-deg cone angle for midcourse maneuver. A change in the antenna pattern requires a change in the aperture design.

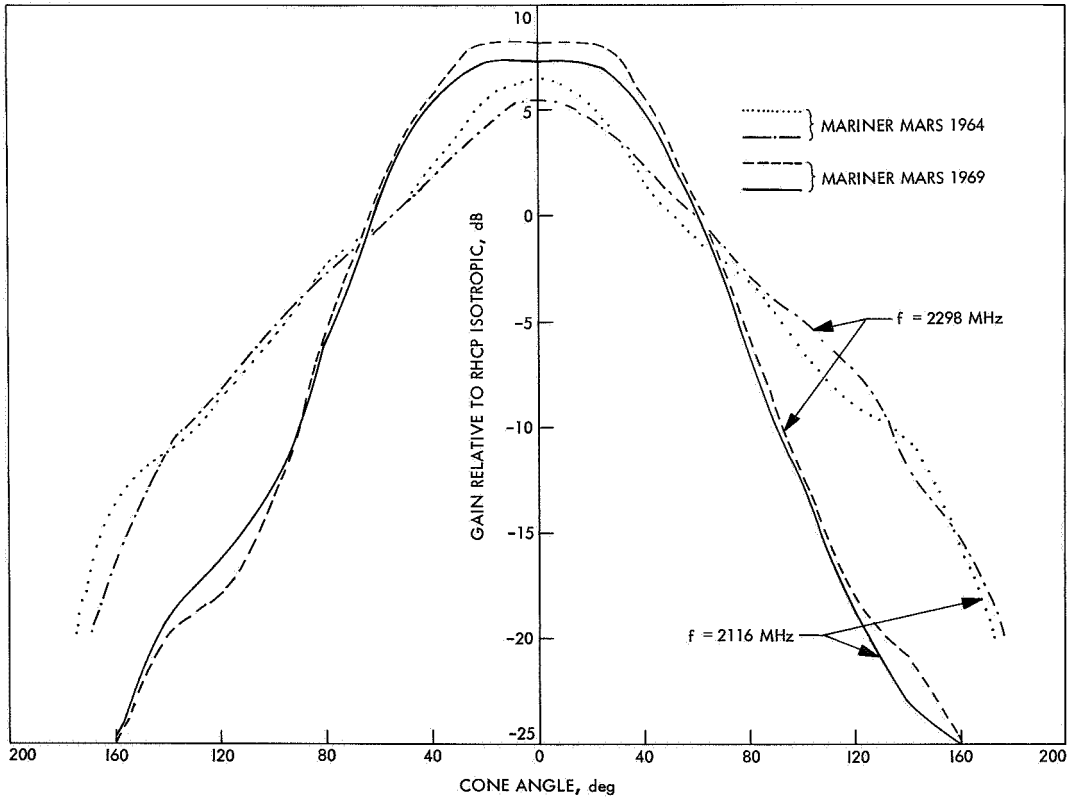

Fig. 29. Low-gain antenna gain vs antenna cone angle

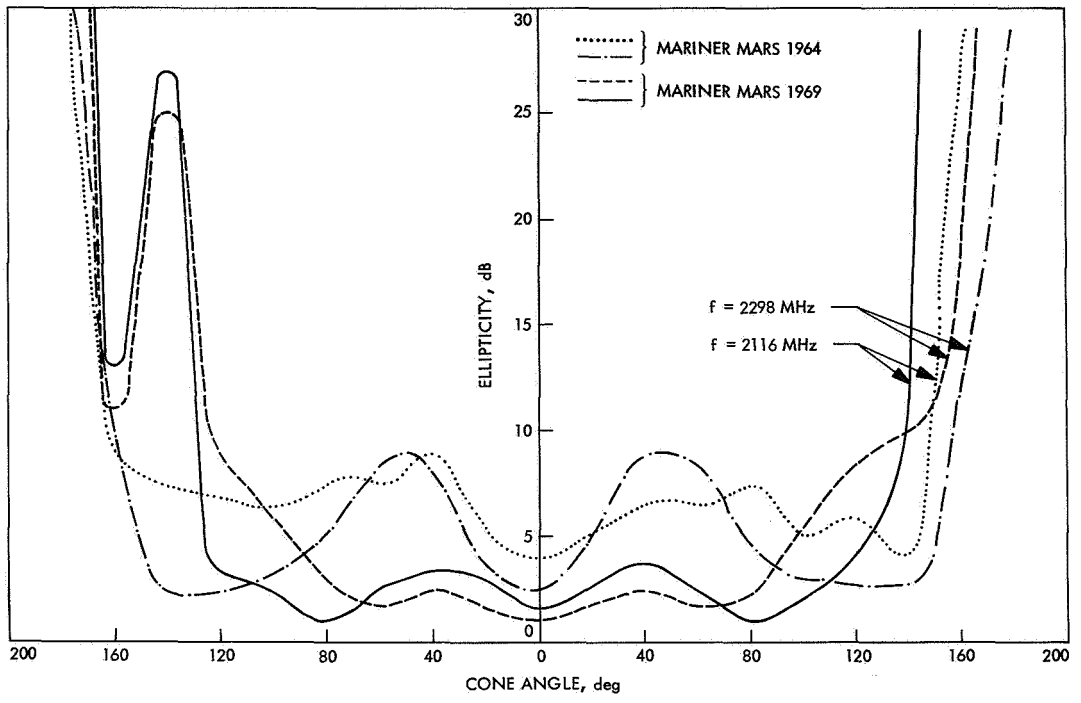

Fig. 30. Low-gain antenna ellipticity vs antenna cone angle

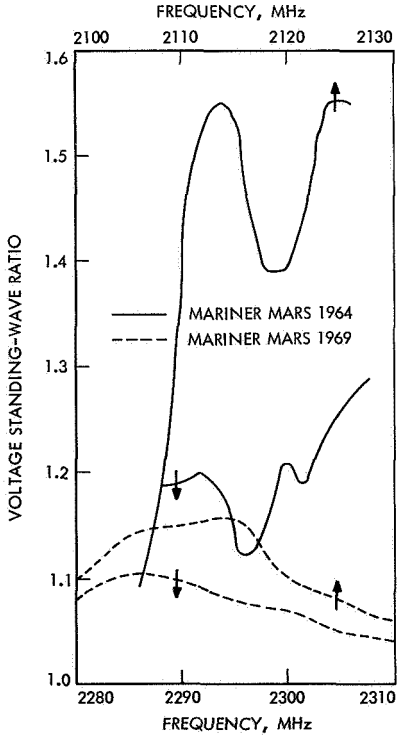

Fig. 31. Low-gain antenna VSWR vs frequency

(3) A radiation pattern that will yield sufficient gain is required to support the 8⅓- and/or 33⅓-bit/s engineering telemetry channel during the launch and cruise phase of the mission. (The details of this requirement are beyond the scope of this report since it is dependent on the radio assembly performance and Deep Space Instrumentation Facility capabilities.)

Figure 32 shows a completely assembled *Mariner* Mars 1969 low-gain antenna in its test fixture and Fig. 28b shows the detailed design. The antenna consists of a waveguide, a linear input probe, an array of transverse septum pins, an array of polarizer pins, a circular aperture with a radome and matching disk, and a conical ground plane. The linear input probe, septum pins, and polarizer essentially replace the *Mariner* Mars 1964 conical spiral feed. A linear, instead of a circular, TE_{11} wave is launched by the probe perpendicular to the septum pins. The septum pins are used to maintain mode purity and to guarantee that the electric vector will not rotate due to phase error effects as the wave travels down the tube. The electric vector must pass through the polarizer pins at a 45 ± 0.5-deg angle in order to produce good circular polarization. This technique of producing linear

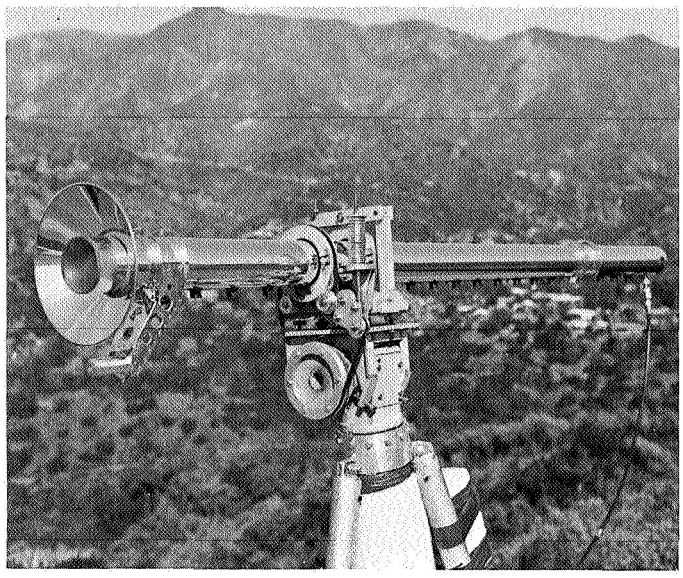

Fig. 32. *Mariner* Mars 1969 low-gain antenna

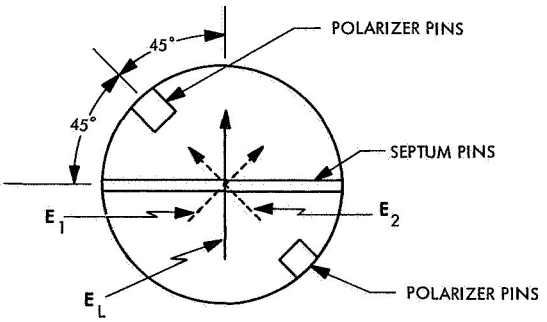

Fig. 33. Electric field inside *Mariner* Mars 1969 low-gain antenna

polarization instead of circular polarization along the entire guide is desirable since there is less chance of introducing phase error. Referring to Fig. 33, the electric vector of the linearly polarized wave can be represented by the sum of two orthogonal vectors:

$$\mathbf{E}_L = (\mathbf{E}_1 + \mathbf{E}_2) \cos \omega t$$

where

t = time, s

$\omega = 2\pi f$

and

f = frequency, Hz

The orthogonal vector $\mathbf{E}_1$ passes through the polarizer unaffected since it is perpendicular to the plane of the polarizer. However, $\mathbf{E}_2$ passes through a capacitive reactance that produces a 90-deg phase shift with respect to $\mathbf{E}_1$. The net result is a circularly rotating (circularly polarized) vector that can be represented by

$$\mathbf{E}_C = (\mathbf{E}_1 + j\,\mathbf{E}_2) \cos \omega t$$

The position of the polarizer relative to the septum pins determines the sense of circular polarization. Figure 33 shows a right-hand screw sense out of the paper. If the polarizer were displaced 90 deg, the screw sense would be left-hand. This entire concept of the probe, septum pins, and polarizer has allowed the tube tolerances to be relaxed to a standard manufacturing tube tolerance without any degradation of performance. Also, the probe, septum pins, and polarizer do not require very tight tolerances and have a simple geometry that reduces machining operations.

During the development phase of the probe and septum pin design, a 6-ft length of waveguide was used to test the purity of the polarization maintained by the septum pins. The linear probe was used to launch a linear TE_{11} wave in the guide with no septum pins. A cross-polarized wave, about 30 dB down from the principal wave, was observed. The principal wave had also rotated 10 deg from its launched position. Next, the septum pins were placed into the guide at an angle of 90 deg to the input probe. The cross-polarized wave was now greater than 40 dB down from the principal wave and the principal wave was parallel to the launched position. This test verified that the septum pin concept did indeed maintain polarization purity and was independent of phase errors introduced by slight deviations in the waveguide wall.

The optimum configuration of an aperture is one with no abrupt discontinuities so that a TM_{01} mode will not be generated. Figure 34 shows four different aperture designs that were studied and Table 6 gives a summary of the performance data. Aperture configuration c yields the best overall performance at the receive frequency (2116 MHz). It has a good on-axis gain and at the same time yields the highest gain of all the configurations at a 40-deg cone angle. Configuration c is also above the minimum allowable gain at a 90-deg cone angle.

The VSWR of the aperture was found to be 1.6 at 2116 MHz. However, a better match was obtained by placing a thin metallic disk, about the size of a quarter,

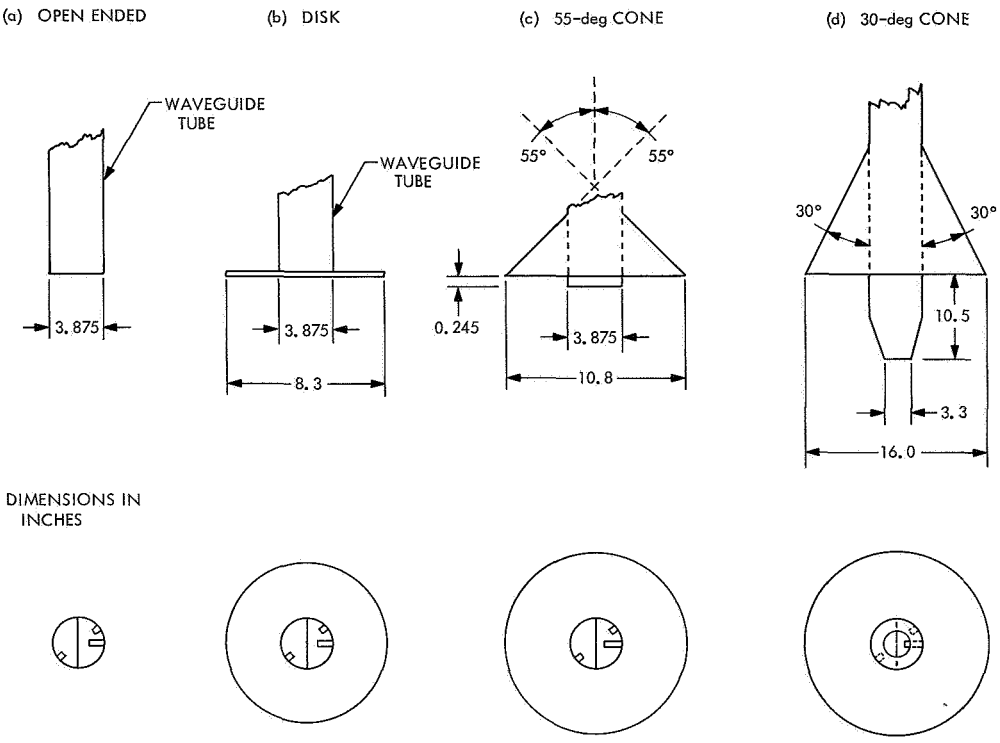

Fig. 34. *Mariner* Mars 1969 low-gain antenna aperture configurations

1.1 in. into the aperture (Fig. 28b). The introduction of the matching disk yielded a VSWR of 1.12 at 2116 MHz.

Radio frequency ionization breakdown tests were performed in the JPL Antenna Breakdown Facility to determine the power handling capability of the design when passing through the critical pressure region during launch.

Table 6. Performance data of various aperture designs

Aperture configuration	Frequency, MHz	Gain relative to RHCP isotropic for various cone angles[a], dB			
		0 deg	27 deg	40 deg	90 deg
a	2116	7.44	6.04	4.04	−5.2
	2298	7.82	5.82	4.12	−6.58
b	2116	7.58	6.28	4.58	−6.6
	2298	7.31	5.61	3.91	−8.5
c	2116	6.83	6.83	5.13	−9.0
	2298	7.85	7.25	5.65	−9.35
d	2116	9.02	3.2	4.32	−9.38
	2298	3.26	7.66	6.06	−7.0

[a]Cone angles measured from boresight axis.

Radio frequency breakdown occurred in the antenna probe input connector at 90 W (frequency = 2295 MHz, pressure = 2 mm of mercury). Therefore, the power handling capability of the *Mariner* Mars 1969 low-gain antenna is well above the spacecraft radio power (10 and 20 W).

The performance data of a completely assembled *Mariner* Mars 1969 low-gain antenna are summarized in Figs. 29, 30, and 31. Comparing these data with the *Mariner* Mars 1964 data, the *Mariner* Mars 1969 low-gain antenna has better overall performance in the forward hemisphere (note the approximately 3.7-dB increase in gain at a 40-deg cone angle). The performance of the *Mariner* Mars 1969 low-gain antenna is exceptionally uniform from antenna to antenna. The maximum gain variation between all the flight units is only 0.2 dB at either frequency and the maximum variation in the VSWR is from 1.13 to 1.16 at 2116 MHz and 1.07 to 1.12 at 2298 MHz. This exceptionally good repeatability comes from "as built" antennas. (The *Mariner* Mars 1969 antennas were built according to their drawings and never required any electrical changes or individual tuning.)

c. High-gain antenna. The *Mariner* Mars 1969 high-gain antenna was also to be designed using the *Mariner*

Mars 1964 design as a baseline. However, performance studies showed that, with the higher data rate requirement and the different trajectory geometry, a major design change was necessary. The two drawbacks of the *Mariner* Mars 1964 design were:

(1) The antenna gain was too low (23.3 dB) to accommodate the high-data rate playback during the post-encounter portion of the mission.

(2) The elliptical gain contours did not optimally fit the trajectory geometry. The *Mariner* Mars 1969 trajectory is such that optimizing the ellipse contours for post-encounter degrades the pre-encounter and encounter performance and vice versa.

The final results of the performance study showed that a fixed position, circular parabolic antenna, with a minimum gain of 25.5 dB, would satisfy the pre-encounter, encounter, and post-encounter performance requirements. A packaging study was then initiated to determine the maximum allowable size of the aperture that could be used on the spacecraft without interfering with any of the other subsystems. A 40-in.-diam aperture was determined to be the maximum allowable size, which meant an antenna efficiency of 59.7% or better would be necessary to meet the performance requirements. To keep the overall costs of the high-gain antenna at a minimum, the *Mariner* Mars 1964 parabolic dish contour was used ($x^2 = 60.72\ y$, which yields an $f/D = 3.795$ for the *Mariner* Mars 1969 dish, where f is the focal distance and D is the diameter of the dish) since the necessary tooling was already available. With a fixed dish contour, the requirement for obtaining a high overall efficiency factor was placed on the feed assembly design.

Four basic turnstile feed configurations were studied (Fig. 35). The performance effects of variations (such as cup depth, cone angle, and element lengths) to each configuration were also studied to obtain a "best tuned" feed for the fixed dish contour. The maximum overall efficiencies obtained with each feed configuration are given in Table 7. It can be seen that the best performance was

Table 7. Efficiency of various feed configurations

Feed	Gain, dB	Efficiency, %
Cupped cavity	25.31	57.0
Flat ground plane	25.62	61.3
Partial cone	25.61	61.2
Full cone	25.81	64.2

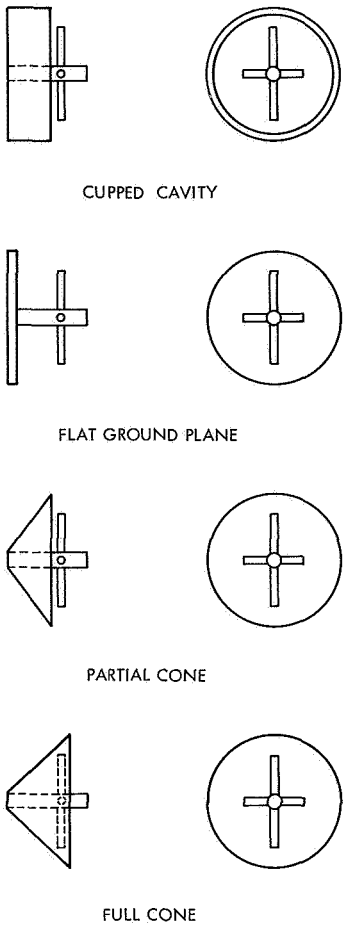

Fig. 35. High-gain antenna feed configurations

obtained from the full-cone feed. Figure 36 shows the left-hand polarized and right-hand polarized power patterns of the full-cone feed. The left-hand component contains 93.7% of the total radiated power, of which 91.8% is intercepted by the dish. (These power percentages are approximate since the characteristics of the feed will change slightly in the presence of a small secondary aperture.)

Because of the high overall efficiency requirement, it was desirable to minimize or even eliminate the effects of manufacturing tolerance buildup between the full-cone feed and the parabolic dish (the *Mariner* Mars 1964 had about a ± 0.3-dB uncertainty due to manufacturing tolerances). The full-cone feed is a relatively small structure with a simple geometry so that a tolerance as low as ± 0.002 in. is easily obtainable. However, this is not true of the dish structure. During the design stages of the *Mariner* Mars 1969 high-gain antenna, it was established that the worst tolerance on the parabolic contour could be as high as ± 0.070 in. due to the manufacturing

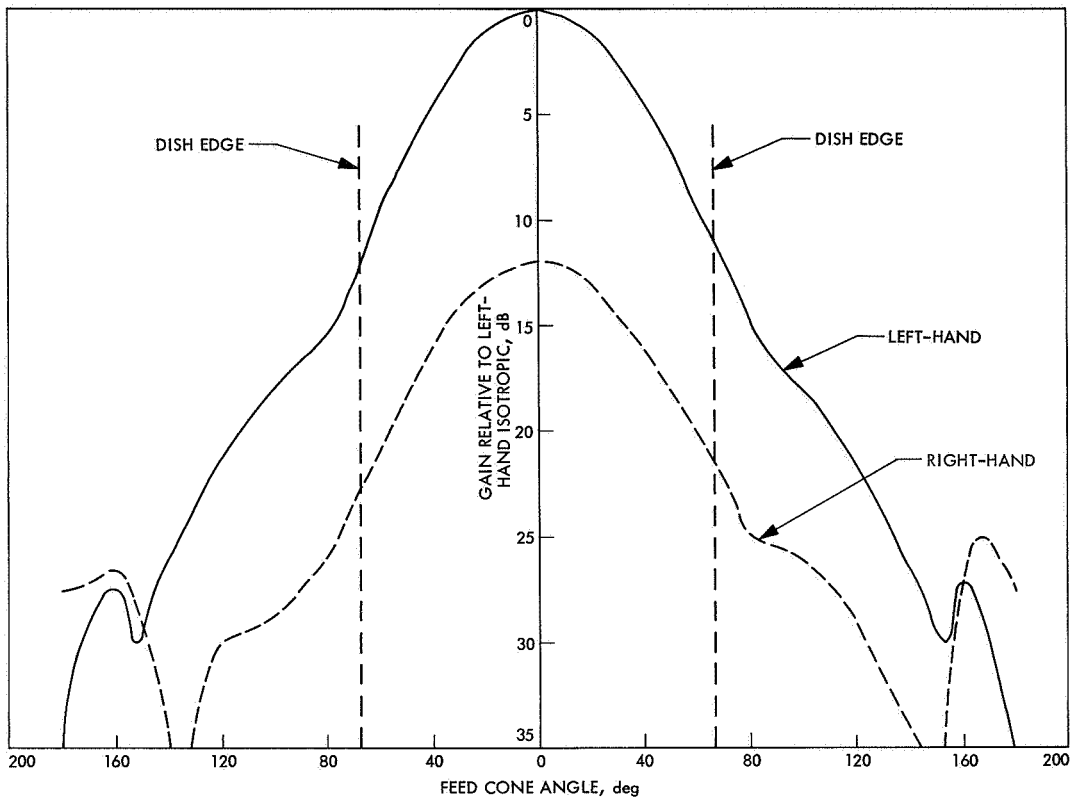

Fig. 36. Full-cone feed power pattern

process. A deviation of this magnitude will cause the theoretical focus point to shift. An analysis showed that a contour deviation of ±0.070 in. would cause a deviation in the focus location of +0.28 to −0.27 in.

To study the effects of this tolerance, the feed in the high-gain antenna was defocused +0.30 in. from the optimum position. The result was about a 0.3-dB loss in gain. Because of this tolerance problem and its effects, a ±0.30-in. feed adjustment about the nominal focus location was incorporated into the design so that each antenna could be individually peaked for performance. However, after the first parabolic dish [temperature control model (TCM)] was fabricated with the *Mariner* Mars 1969 tooling, it was discovered that the parabolic contour deviated only ±0.010 in. from the true contour. It was then established that the remaining six dishes could be duplicated to within ±0.010 in. of the TCM dish. Since the manufacturing repeatability was better than expected, it was concluded that testing costs and schedule could be reduced if the TCM dish was used as a representative model to determine a fixed-feed location for all the remaining antennas. Figure 37 shows the results of the feed optimization study that was performed on the TCM antenna. The peak gain occurs at a mounting plane distance of 15.625 in. from the vertex; however, the on-axis ellipticity is 2.8 dB, which could result in about a 0.13-dB polarization loss. The optimum feed location actually occurs at 15.749 in. from the vertex. The gain loss relative to the 15.625-in. position is 0.06 dB, and the ellipticity is 1.1 dB, which could result in about a 0.04-dB polarization loss. Also, the overall ellipticity as a function of the antenna cone angle for the 15.749-in. location was much lower than the overall ellipticity for the 15.625-in. location. This means that the feed phase center is approximately 0.32 in. in front of the mouth of the cone. As a result of this study, all *Mariner* Mars 1969 antennas have a fixed-feed mounting position of 15.749 in. from the vertex.

The feed cable location and orientation relative to the feed turnstile elements was also found to be a critical parameter if maximum efficiency was to be obtained. A study was conducted to determine a feed cable configuration that had the least deleterious effect on performance. The number of cable configurations was

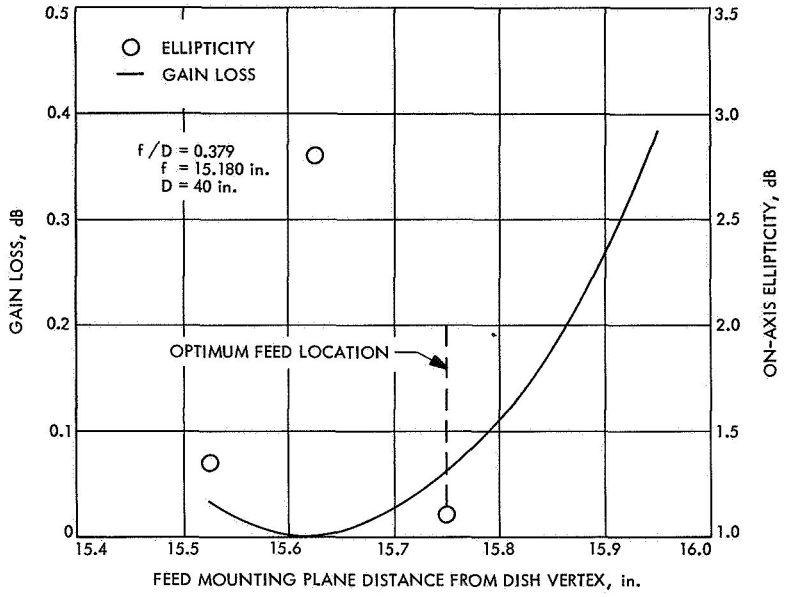

Fig. 37. High-gain antenna gain loss and ellipticity vs feed mounting distance from dish vertex

greatly reduced by first establishing two important ground rules: (1) the length of the cable should be minimized to reduce dissipative losses, and (2) the cable routing should minimize aperture blockage. Five different cable configurations were studied. Optimum results were obtained with the configuration shown in Fig. 38. The cable is contained in a single plane for minimum blockage. For minimum impedance and cross-polarization effects, the cable is 2.5 in. from the feed cone and is in the plane of the longest turnstile elements.

The high-gain antenna also has a small monitoring probe mounted in the dish, which is used to sample a portion of the radiated feed energy. The sampled signal is used as an umbilical function for monitoring the high-gain antenna output. The probe was initially designed to have a 20-dB coupling factor since the low-gain antenna precision coupler (which is also an umbilical function) has a 20-dB coupling factor; hence, the two umbilical signal levels would be about the same. However, a 20-dB probe coupler degraded the antenna ellipticity because the probe coupling was about 5 dB above the cross-polarized component of the antenna. A probe coupler was then designed with 25 dB of coupling and was found to have very little effect on the cross-polarized component. In the *Mariner* Mars 1969 probe design, a bulkhead TM connector is used on the back of the dish instead of a 4-in. RG 142 cable feed-through that was used on *Mariner* Mars 1964. A comparison of the performance between the two probes is shown in Table 8.

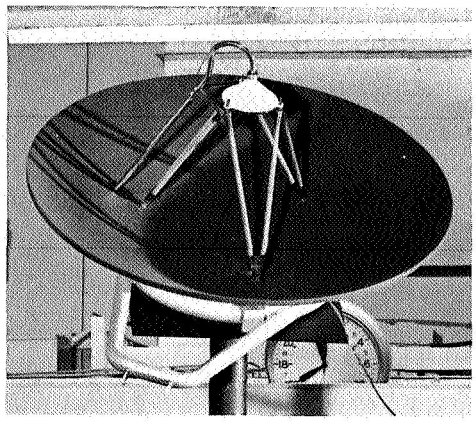

Fig. 38. *Mariner* Mars 1969 high-gain antenna

The performance of the *Mariner* Mars 1969 high-gain antennas is closely repeatable from antenna to antenna. The maximum variation in gain between the flight units

Table 8. Comparative data between *Mariner* Mars 1969 and *Mariner* Mars 1964 probes

Design	Frequency, MHz	Coupling, dB	Voltage standing-wave ratio
Mariner Mars 1969	2298	25.3	1.65
Mariner Mars 1964	2116 2298	28.8 25.8	4.8 4.7

and the proof-test model (PTM) unit was only 0.16 dB. The maximum variation in the VSWR of these units was 1.02 to 1.15, and the maximum variation in ellipticity was 0.4 dB. A summary of the performance of the PTM antenna is shown in Figs. 39 and 40. The on-axis gain of the M69-4 antenna was 25.76 dB, which was the lowest encountered in the four units (Table 9). It can be seen from Table 9 that the minimum design gain of 25.5 dB has been surpassed by at least 0.26 dB for all of the flight units. Studies have shown that the gain varies less than 0.04 dB over the operating band of 2295 ± 5 MHz.

The *Mariner* Mars 1969 high-gain antenna is a highly optimized device specifically designed for the *Mariner* Mars 1969 mission. However, its basic design could prove valuable for future planetary missions, especially if antenna pointing techniques were to be employed.

Table 9. Performance data of *Mariner* Mars 1969 high-gain antennas[a]

Unit	On-axis gain, dB	Efficiency, %	On-axis ellipticity, dB	Voltage standing-wave ratio
PTM	25.82	64.2	0.95	1.11
M69-2	25.92	65.7	1.00	1.12
M69-3	25.92	65.7	0.85	1.02
M69-4	25.76	63.4	1.25	1.15

[a]Frequency = 2298 MHz.

2. Flight Command Subsystem

a. Introduction. The *Mariner* Mars 1969 flight command subsystem (FCS) accepts modulated command subcarrier information from the transponder receiver and demodulates and decodes these signals into commands for the various flight subsystems. The commands are directed to the other flight subsystems via the switching of transistor switches, called universal isolation switches (UISs), which provide dc isolation between all spacecraft subsystems. There are three types of command signals: direct command (DC), coded command (CC), and quantitative command (QC).

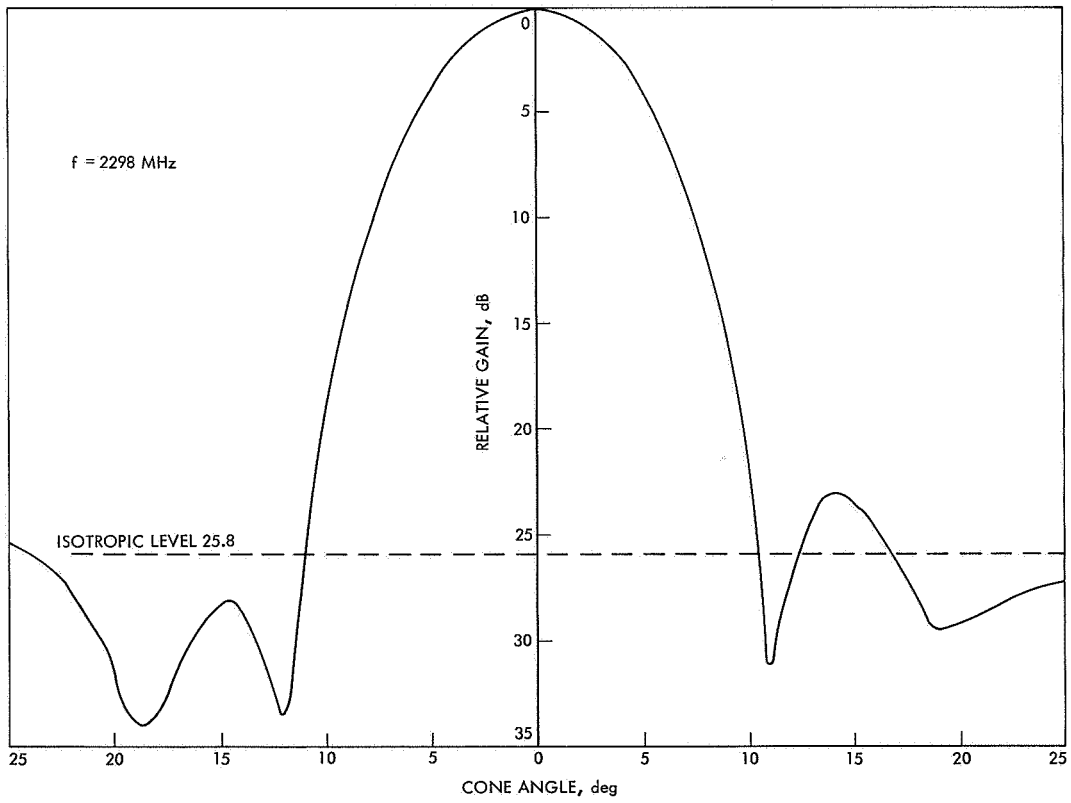

Fig. 39. *Mariner* Mars 1969 high-gain antenna gain vs cone angle

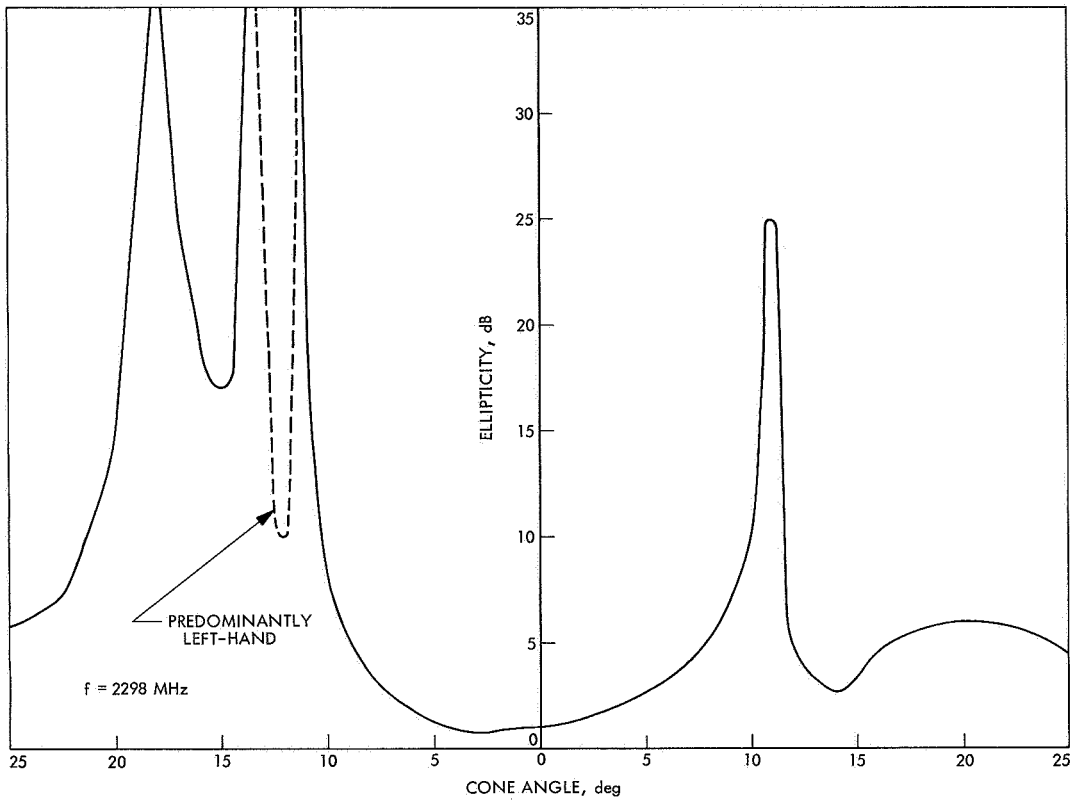

Fig. 40. *Mariner* Mars 1969 high-gain antenna ellipticity vs cone angle

The FCS is designed to operate with 53 DC signals, 3 CC signals, and 4 QC signals. The 53 DC signals are single 100-ms transistor switch closures to the applicable spacecraft subsystems. Of the three CC signals, two are 100-ms switch closures and one is switch closures resulting in serial nonreturn-to-zero data bits as opposed to the pulsed command. The CC signals operate redundantly, resulting in two each of the three output signals. The four QC signals are switch closures of 100-ms duration at 1-s intervals; the number of switch closures is controlled by the number of *ones* in bits 9 through 26. The operational data of the FCS detector are given in Table 10.

The command bits and reference frequency are transmitted via a coherent phase-shift-keyed (PSK) subcarrier of frequency f_s, with bit synchronization transmitted in the form of a pseudonoise (PN) code. The command detector separates the command and bit sync signals. The filtered and frequency-doubled command reference is then used to demodulate the command information coherently, and the command bits are detected in a matched filter. The detected binary pulse train is presented to a program control function, along with bit timing pulses.

The FCS consists of three main functional units: the command detector, command decoder, and program control. Also included is a transformer rectifier unit that converts the spacecraft 2.4-kHz voltage into ac and dc voltages required by the subsystem.

b. Command detector. The command detector provides three main functions: (1) establishes a phase coherent reference signal by locking a phase-locked loop (PLL)

Table 10. FCS detector operational data

Parameter	Value
Modulation input	PN $\oplus$ $2f_s \pm \sin 2\pi f_s t$
Composite input signal, mV rms	100 ± 25%
Threshold signal-to-noise ratio, dB/Hz	16.5 ± 1
Input signal noise bandwith, Hz	2350
Input impedance, kΩ	$\geq$100
Probability of bit error at threshold	$\leq 10^{-5}$
Probability of $\overline{\textit{in-lock}}$ indication at threshold	$2.25 \times 10^{-4} \pm 50\%$
Maximum detector lockup time, min	12.5

to the frequency-doubled transmitted-data subcarrier (PLL channel); (2) generates a detector *in lock* signal, which indicates proper synchronization with the transmitter, and enables the decoder (lock channel); and (3) demodulates and detects, in the presence of noise, data bits that are transmitted from earth as a biphase-modulated sinusoidal subcarrier (command channel). The simplified block diagram of the detector is given in Fig. 41.

The detector operates on a biphase-modulated data signal of $\pm \sin 2\pi f_s t$ added to a sync signal composed of a PN sequence, modulo-2 added to a square-wave signal at the clock frequency defined as $2f_s$. The composite signal may be expressed mathematically as PN $\oplus$ $2f_s$ $\pm \sin 2\pi f_s t$. The subcarrier $\sin 2\pi f_s t$ is used instead of $\cos 2\pi f_s t$ to lessen the intermodulation problems between data and sync signals (Ref. 1, pp. 7–10).

The phase ambiguity of the data signal is removed by $\times 2$ multiplication in the PLL channel, and the loop is locked to the $\sin 2\pi 2f_s t$ signal. The PLL signal is then used to provide a coherent reference for all phase detectors. Bit synchronization is obtained by correlating the transmitted PN $\oplus$ $2f_s$ with the FCS-generated PN $\oplus$ f_s (RS 36-10, Vol. I, pp. 54–63). Correlation is achieved by a discrete-step time search, in which the reference PN $\oplus$ f_s is compared against the received sync signal in the lock PN phase detector (Ref. 1, pp. 15–18).

The search mode is initiated by the detector logic when three consecutive *out-of-lock* signals are received from the locked channel matched filter. The search logic advances the code sequence one PN bit each cycle of the code. When the codes correlate, the PN phase detector produces an f_s $\angle 90°$ output, which is filtered in the f_s bandpass filter (BPF) to remove multiplication products.

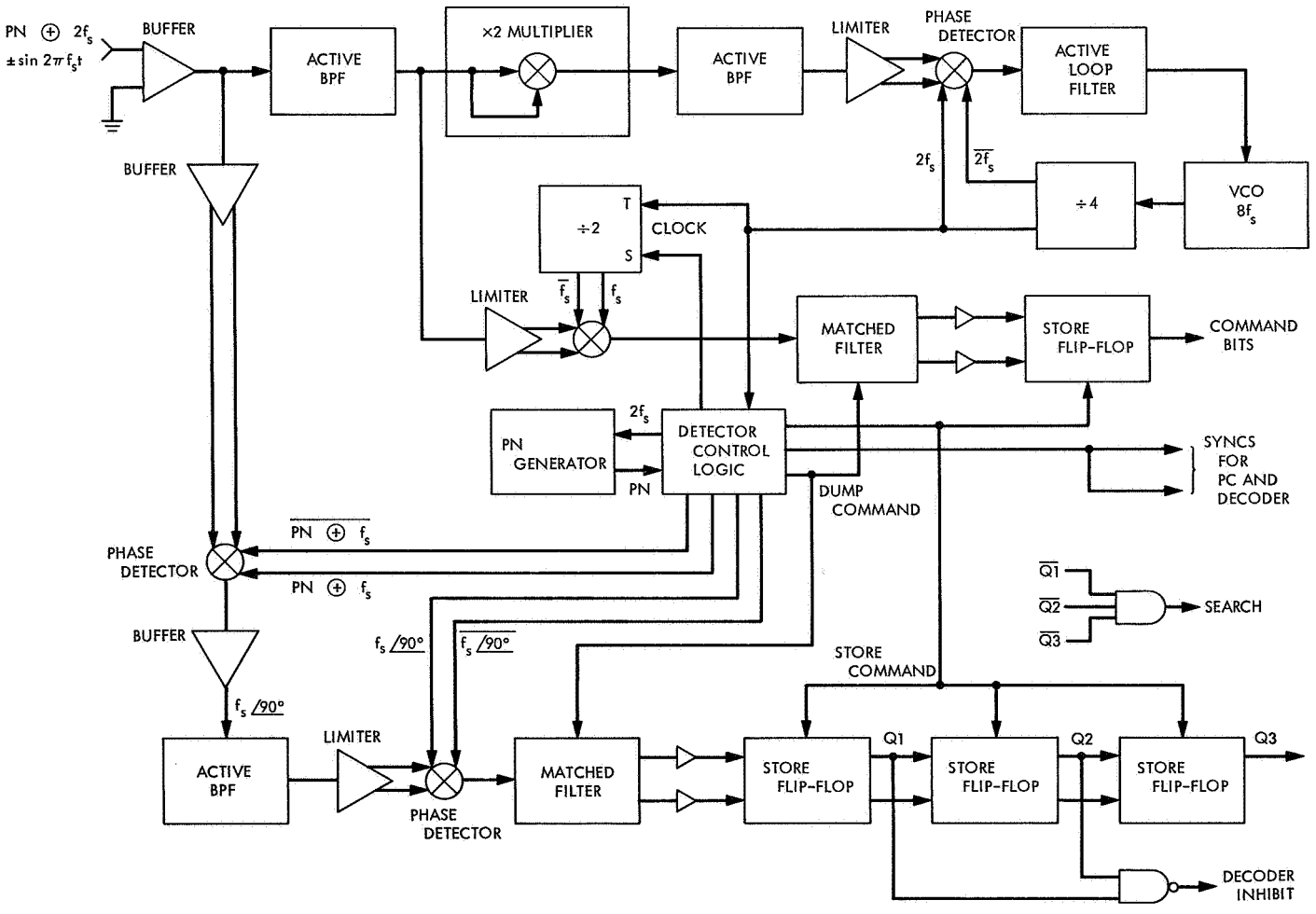

Fig. 41. FCS detector functional block diagram

The f_s ∠90° signal is then demodulated in the lock f_s phase detector and detected in the presence of noise by the lock matched filter. A bias is applied to the lock matched filter to establish a probability of indicating lock of 1.5×10^{-2} in the presence of all noise. When *in lock* is detected, the search is inhibited, and after two consecutive *in locks* the decoder is enabled for message processing. No commands are processed by the decoder until the lock channel establishes bit synchronization.

The command channel phase detector demodulates transmitted message bits with a clocked f_s' reference. The f_s' reference is derived from the PLL coherent $2f_s$ and is reclocked at the beginning of each bit time to obtain proper synchronization with the transmitted data signal. After demodulation, the data bits are detected from the noisy signal by further bandwidth reduction in the command matched filter. Threshold for the detector is defined at a bit error rate of 10^{-5}, and occurs at a composite command signal-to-noise ratio of 16.5 ± 1 dB in a 1-Hz noise bandwidth. At bit sync time, the detected bits are serially stored in a data shift register for interrogation by the decoder.

c. Command decoder. A simplified block diagram of the decoder is given in Fig. 42. The function of the decoder is to decode digital data bits from the program control and provide isolated output commands. It consists of 85 UISs, a synchronizer module, and a register preset module. The decoding function is implemented within each UIS by an integrated circuit diode *and* gate. Depending on the bits stored in the data registers, one or more of the UISs is closed upon being enabled by the program control. The synchronizer module synchronizes the UIS enable pulses to the 2.4-kHz power source used by the UIS, thereby controlling the turn-on characteristics of the switch. The register preset inhibits any decoder outputs that could occur during power turn-on.

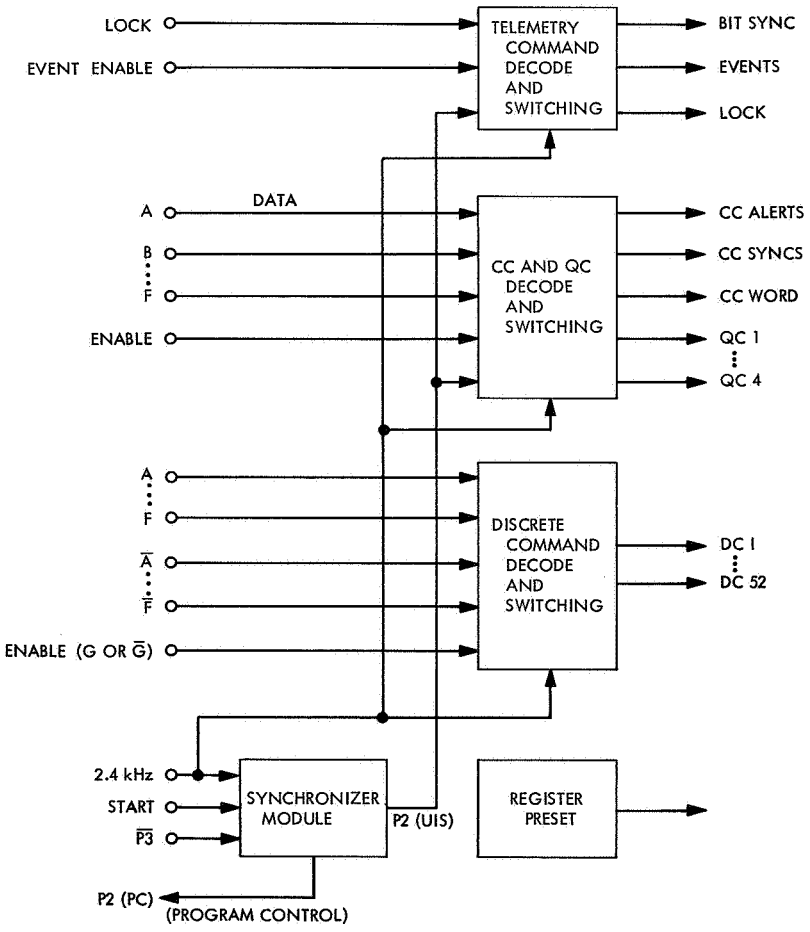

Fig. 42. Decoder block diagram

The command format for the *Mariner* Mars 1969 FCS is given in Fig. 43. Bits 1 through 3 form the word start pattern (110). Bits 4 through 9 are the command subaddress. If a DC subaddress is recognized by the program control, a corresponding set of DC switches is enabled so that the decoder will activate the UIS corresponding to the DC command address contained in bits 20 through 26. If bits 4 through 9 are not a DC subaddress, these bits are stored in the data registers and the QC and CC switches are enabled. Thus, the QC or CC switch corresponding to the stored address bits 4 through 9 will then be activated by the following bits 10 through 26. The *Mariner* Mars 1969 program control is capable of recognizing two DC command subaddresses. Presently only one DC subaddress recognition logic and related UIS enable signal is used. Thus, the *Mariner* Mars 1969 logic has a built-in expansion capability of 62 additional direct commands. All addresses use one bit for parity check, so that two bit errors would be necessary to generate an incorrect command.

The decoder also directs three command signals to the spacecraft telemetry subsystem to be telemetered to earth. The signals time-share the telemetry transmission channel. A listing of these signals and their information content follows:

(1) Detector delayed bit sync pulses that gate a stable 12-kHz oscillator providing a time-interval-type measurement of the command detector voltage-controlled oscillator (VCO) frequency. This telemetry measurement detects any flight VCO frequency drifts that would delay or prevent phase-lock acquisition.

(2) A binary detector lock signal that provides information concerning the detector lock condition. The detector lock data indicate whether the command subsystem is capable of detecting and processing the command signal.

(3) Command event pulses that indicate the command subsystem responses to commands. A command event pulse is initiated after a subaddress is recognized, and after every command has been completely processed.

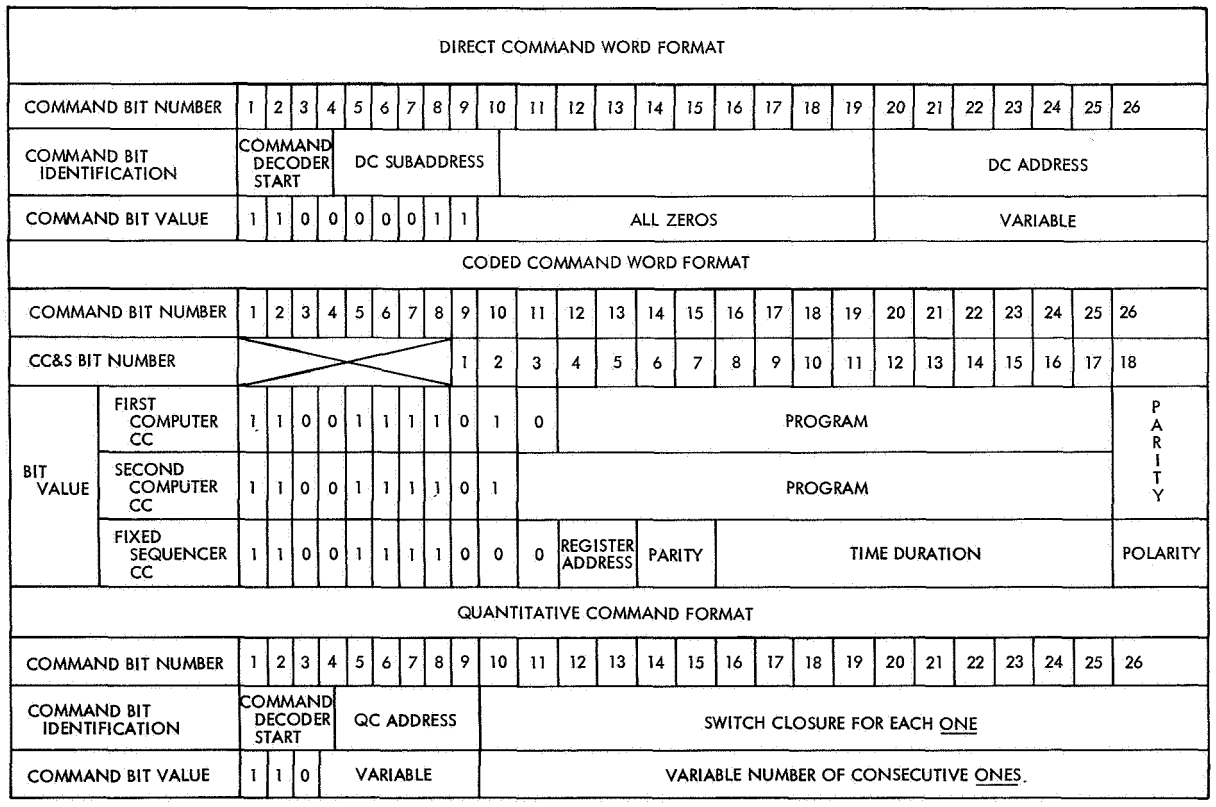

Fig. 43. *Mariner* Mars 1969 command word format

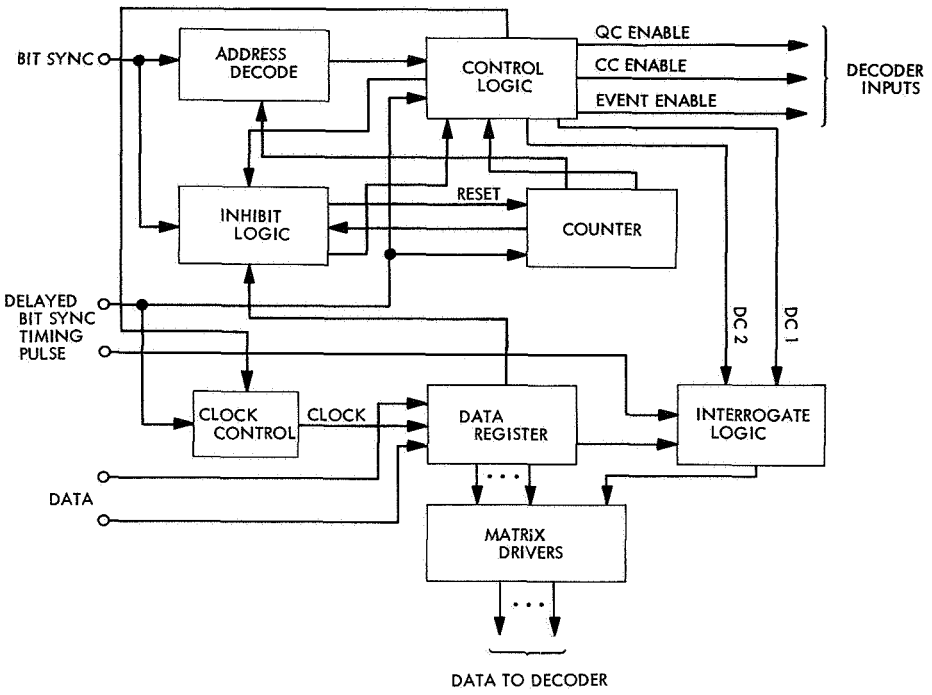

Fig. 44. Program control block diagram

d. Program control. The program control portion of the FCS performs the functions of word-start error checking, subaddress decoding, data processing, and decoder control. A block diagram of the program control is shown in Fig. 44. The program control logic receives decoder enable and timing pulses, along with data bits from the command detector. The logic circuit checks the serial data information for proper format. This information is processed into correct decoder control and data signals if the decoder enable control signal is present and the format checks. The operation of the program control is shown in Fig. 45.

Reference

1. *Mariner Mars 1969 Flight Command Subsystem and Operational Support Equipment*, Final Engineering Report, JPL Contract 951700. Motorola, Inc., Military Electronics Div., Aerospace Center, Scottsdale, Ariz., Sept. 1, 1967.

G. Space Sciences

1. Infrared Spectrometer Subsystem

a. Proof-test model. The malfunction of the channel 1 (HgGe) detector reported in SPS 37-52, Vol. I, p. 30, was found to be caused by a break in the detector wire. The wire had been damaged previously when an out-of-tolerance test fixture was inserted over the detector and cryostat. The proof-test model infrared spectrometer (IRS) monochromator–telescope assembly and the gas storage and delivery assembly are being updated to flight configuration for continuation of the assembly-level type-approval test program.

b. Flight units. The excessive noise appearing in the channel 2 (PbSe) output of the first flight unit (SPS 37-52, Vol. I) was found to be caused by mechanical stresses introduced at the channel 2 detector/mounting post interface at operating temperature (−38°C). The stresses were caused by the materials at the interface having different thermal coefficients of expansion. The material at the end of the mounting post was changed to solve this problem.

The three flight units have been delivered to JPL and have been used to support flight spacecraft testing. During thermal–vacuum testing of the M69-3 spacecraft, the IRS motor stalled and could not be restarted. Although disassembly and inspection of this unit has not been performed, it is believed that the problem resulted from galling at the shaft/bushing interfaces of the gear train (see *Paragraph c*). This gear train is driven by the motor and is not a part of the motor gear head. A design review has been conducted on the gear train resulting in a proposal to change the bushing material from stainless steel

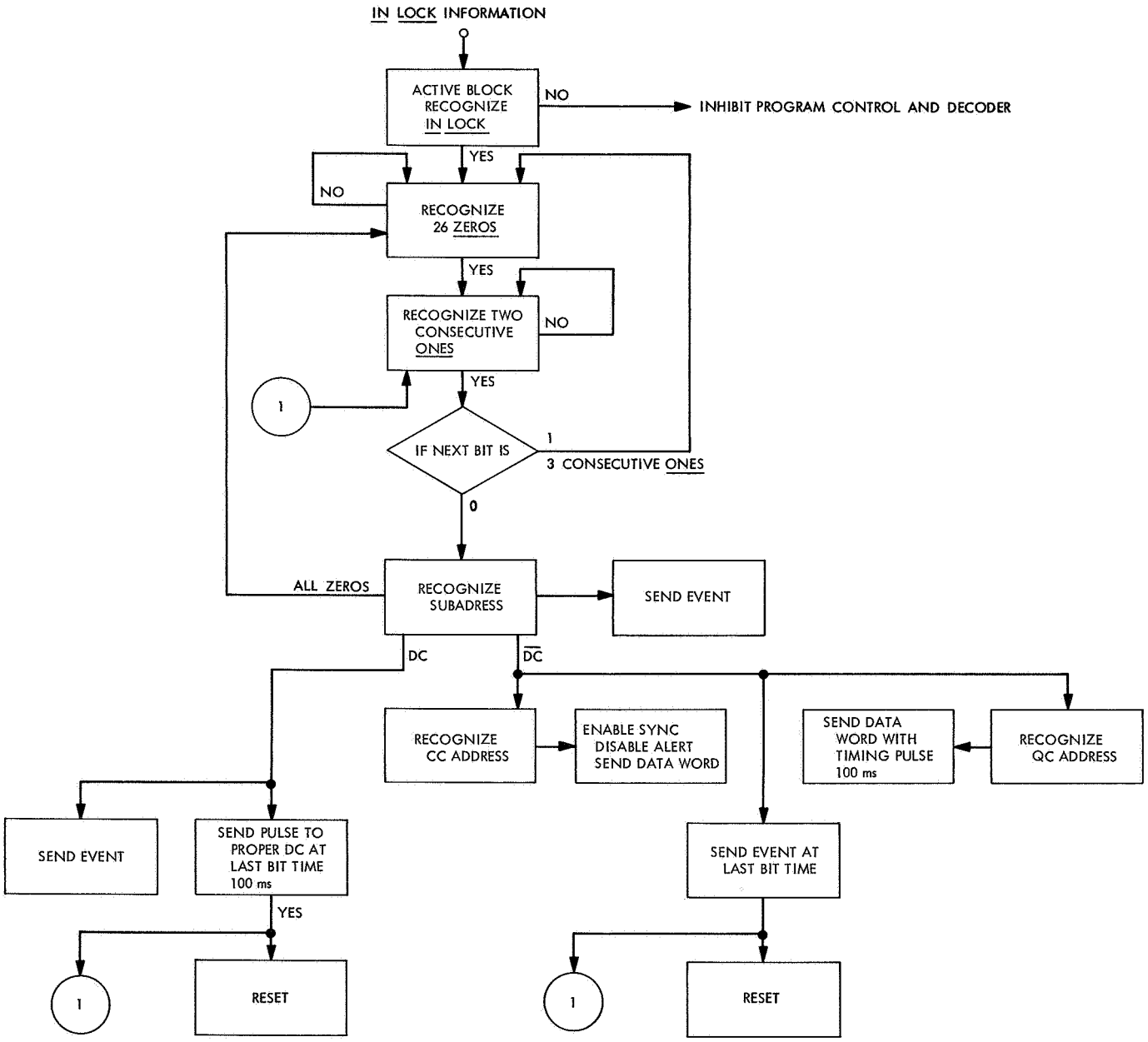

Fig. 45. Program control flow chart

to Teflon S-5. The Teflon S-5 bushings have been installed in a test unit gear train and are being evaluated for possible application to the flight units.

c. Molecular-sink test. Two additional life tests of the IRS gear train have been performed since initially reported in SPS 37-52, Vol. I. These tests consisted of a non-operating "soak" to simulate spacecraft cruise conditions (50 h at 10^{-11} torr and +40°C), an operating period of 10 h at +25°C, and then an extended operating period at −40°C. All three tests proceeded as planned through the simulated cruise phase. The motor stalled after 122 h of operation at −40°C in the first test, after 16 h of operation at −40°C in the second test, and after 4 h of operation at +25°C in the third test. Inspection after each test showed galling at the shaft/bushing interfaces although the shafts were free to turn in the bushings at room temperature after the first two tests. Metallic particles were found in the bushings after the third test, however, which caused the gear train to bind even at room temperature. These bushings have been replaced with Teflon S-5.

d. Gaseous hydrogen storage vessel. Continuation of the fracture-toughness measuring program at The Boeing Company revealed that Inconel 718 was quite susceptible to flaw growth in the presence of high-purity, high-pressure gaseous hydrogen. Inconel 718 is so tough in air that proof-testing reveals only that a flaw does not quite extend through the wall. Therefore, with a meaningless proof test, strong dependence on nondestructive test methods was unacceptable. Subsequent fracture-toughness testing showed that aluminum 2219 had no susceptibility to the hydrogen environment and indeed was as tough in high-pressure hydrogen as in air. Aluminum 2219 vessels have been fabricated, tested, and delivered to the University of California at Berkeley. These vessels have also been retrofitted into the IRS flight hardware.

2. Ultraviolet Spectrometer Subsystem

a. Introduction. The primary scientific objective of the ultraviolet spectrometer (UVS) experiment is to determine the relative abundance of the individual atoms, molecules, and ionic constituents of the Martian atmosphere by measuring the emission and absorption in the ultraviolet region during the planetary flyby. In addition, scale height measurements made on the individual species will be used to construct an atmospheric temperature profile as a function of altitude, and Rayleigh scattering measurements will give information about the total density in the lower atmosphere.

The *Mariner* Mars 1969 UVS is capable of detecting atmospheric constituents to 1% of the total density of the Martian atmosphere as determined by the *Mariner* Mars 1964 occultation experiment.

b. Instrument description. Figure 46 is a functional block diagram of the UVS, and Fig. 47 shows the UVS configuration and the optical path through the instrument. Light entering the entrance aperture is restricted to a narrow field of view before it strikes the telescope primary mirror. The telescope primary mirror focuses an image of the planetary limb on an occulting slit (pre-slit) that blocks out light from the planet disk. The telescope secondary mirror images the light from the occulting slit onto the entrance slit of the Ebert monochromator. Light from the entrance slit fills half of the Ebert mirror. The mirror collimates the light and reflects it to fill the grating, which is replica-ruled with 2160 lines/mm and mounted to borosilicate crown glass. The grating is rotated through approximately 20 deg every 3 s in scanning the spectrum. The dispersed light from the grating is focused on the two exit slits by the remaining half of the Ebert mirror. The two exit slits are used to provide signals for separate photomultiplier channels that operate in different wavelength bands.

The G channel (UVS 1) will use a tube with a lithium fluoride window and a cesium iodide cathode. It will view the spectrum in the first order from approximately 1800 to 2200 Å and in the second order from 1100 to 2150 Å. The N channel (UVS 2) will use a tube with a sapphire window and a bialkali cathode. It will view the spectrum in the first order from 1900 to 4300 Å and in the second order from 1500 to 2150 Å. The N channel leads the G channel by approximately 100 Å in scanning the spectrum. Light passing through the exit slits enters the sensors and is converted to electrical signals that are proportional to intensity.

The electronics portion of the UVS consists of two independent photomultiplier analog channels supplying signals to separate analog-to-pulse-width (A/PW) converters, two high-voltage power supplies and associated control drivers, appropriate logic circuits to supply the proper synchronized switch signals, electronic calibration signals, a planetary disk detector, calibration sources, a fiducial generator, countdown and scan motor drive circuits, a current limiter, and a low-voltage power supply.

The dynamic range of the instrument is from 70 Rayleighs to 18 × 10^3 Rayleighs per 20-Å interval for the G channel and 80 Rayleighs to 20 × 10^3 Rayleighs for the N channel at high gain. At low gain, the N channel range is 200 × 10^3 Rayleighs to 50 × 10^6 Rayleighs.

The resolution of the instrument for first order spectra is 20 Å and the accuracy of measurement is 5%. At a flyby distance of 5700 km, the dimensions of the column of space 100 km above the planet surface, viewed by the slit, are 24 by 240 km.

One scan is made every 3 s and about 180 ms of the scan time will be required for grating flyback to begin scan position. Each channel is sampled every 5 ms. Channel N is sampled 2.5 ms after channel G. There are 200 samples/s/channel and each sample is digitized to 8 bits.

The total weight of the instrument is 35 lb and the maximum overall dimensions are 21.5 × 11 × 6 in., not including the telescope sun shade extension. The instrument requires 15 W of 50-V rms, 2400-Hz power.

c. Design problems. The problem with the flexible metallic bellows (SPS 37-51, Vol. I, p. 18) used to house the gear train in the scan drive mechanism has been solved. The original bellows, made from a nickel alloy, cracked as a result of vibration tests. A newly designed bellows assembly made of pure nickel has been successfully tested to type-approval and life-test requirements. This newly designed bellows assembly was subsequently retrofitted to all units.

Another major problem not previously reported was that of the planocentric needle bearings. Initial system testing on the proof-test model (PTM) spacecraft resulted in the binding and stalling of the scan drive mechanism. Inspection of the bearings revealed that oil marks on the crank were skewed around the crank rather than along the axis of the crank. This led to the conclusion that the needles are cocked or skewed during operation and would tend to make the bearing act as a clamp. The local heat generated from the friction would tend to degrade the lubricant. The rocking motion of the planocentric pinion due to the bellows tended to aggravate this problem.

This problem was solved by replacing the needle bearing with a ball bearing. The bearing used has a phenolic retainer vacuum-impregnated with oil, which tends to act as a wick for the lubricant. This newly designed bearing system has successfully passed both type-approval and life-test requirements. All units have been retrofitted with this new design.

More recently a problem was encountered with double fiducial pulses from two of the flight units. On one unit (SN001), a small particle of ferrous material was found on one pole of the magnet, which caused inhomogeneities in the magnetic field and resulted in spikes on the pickup signal. The problem was resolved by removing the particle. On SN003 the double fiducial pulse was caused because the magnet was installed backwards. The error was corrected by reversing the leads on the pickup coil. The correction, however, resulted in the Lyman-alpha portion of the spectrum arriving about 8 samples late with respect to the Data Automation System (DAS) integration of samples 182 to 201 counted from the fiducial pulse (Fig. 48). This deviation will be adjusted during the final calibration period.

d. Performance testing. All of the flight units have successfully completed the required subsystem flight-acceptance tests. These units are presently undergoing testing at the system level on the respective spacecraft.

Figure 49 is an example of UVS data on an IBM 4020 computer plot. This plot was made from data taken during a system test in the space simulator. Both the limb sensor stimulus and the internal mercury lamp are on. The limb stimulus has the effect of reducing the gain on channel 2. The edge of the continuum from this lamp is seen at the end of the scan on channel 2. Lines from the mercury lamp are seen on both channels. On channel 1 the 1849-Å mercury line is seen in first and second order. The 2537-Å line is seen on both channels.

On October 1, the prototype UVS was launched from White Sands, N.M., on an Aerobee rocket in order to complement the scientific results expected at Mars. In general, the instrument performed well throughout the data-gathering sequence. However, during part of the sequence, an excessive amount of light was detected above 3000 Å. Also, the instrument failed to turn off at the proper time upon re-entering the lower atmosphere. This anomaly resulted in arcing at the critical pressure and operational failure in both channels. With the electronics inoperative, postflight test could not be immediately performed.

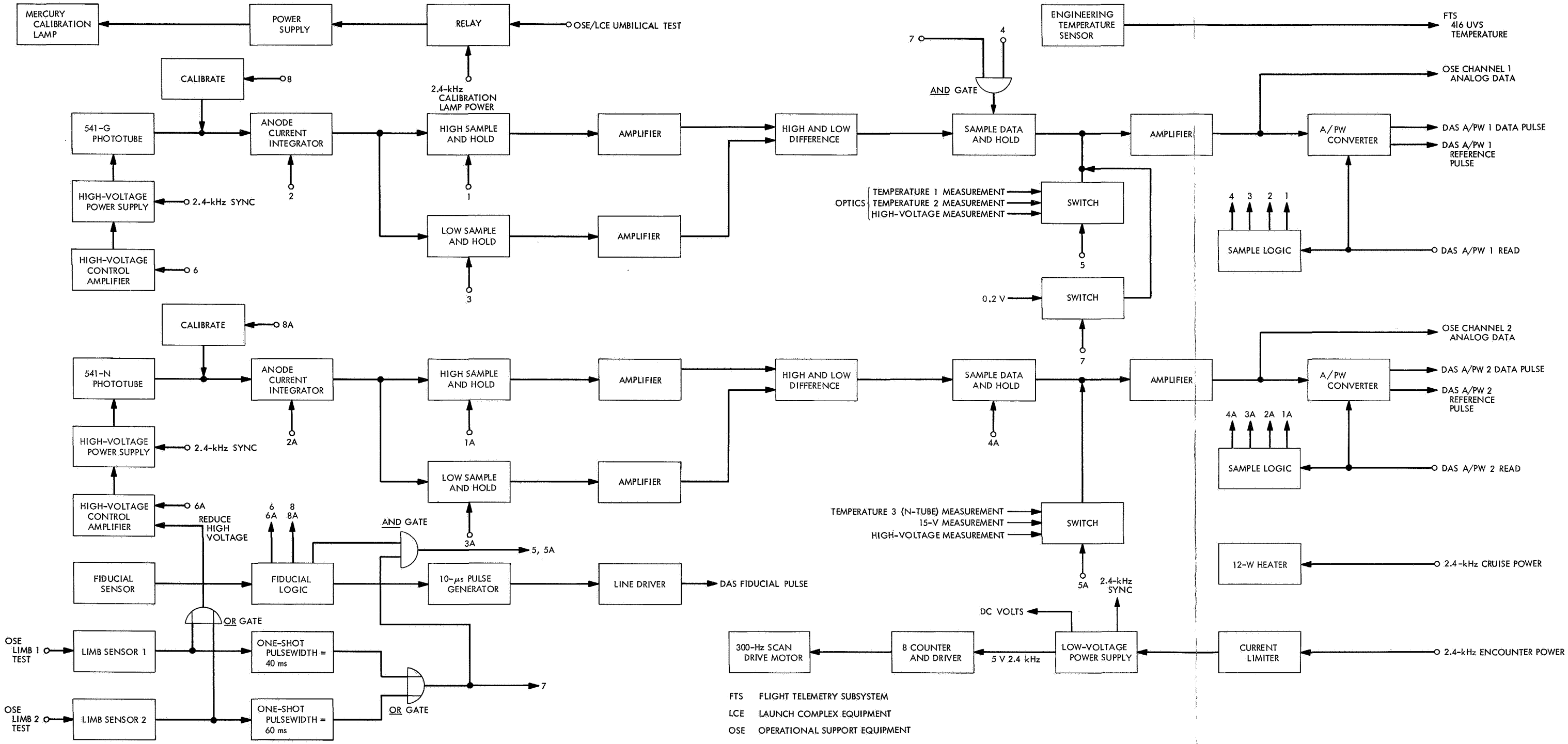

FTS FLIGHT TELEMETRY SUBSYSTEM
LCE LAUNCH COMPLEX EQUIPMENT
OSE OPERATIONAL SUPPORT EQUIPMENT

Fig. 46. Ultraviolet spectrometer functional block diagram

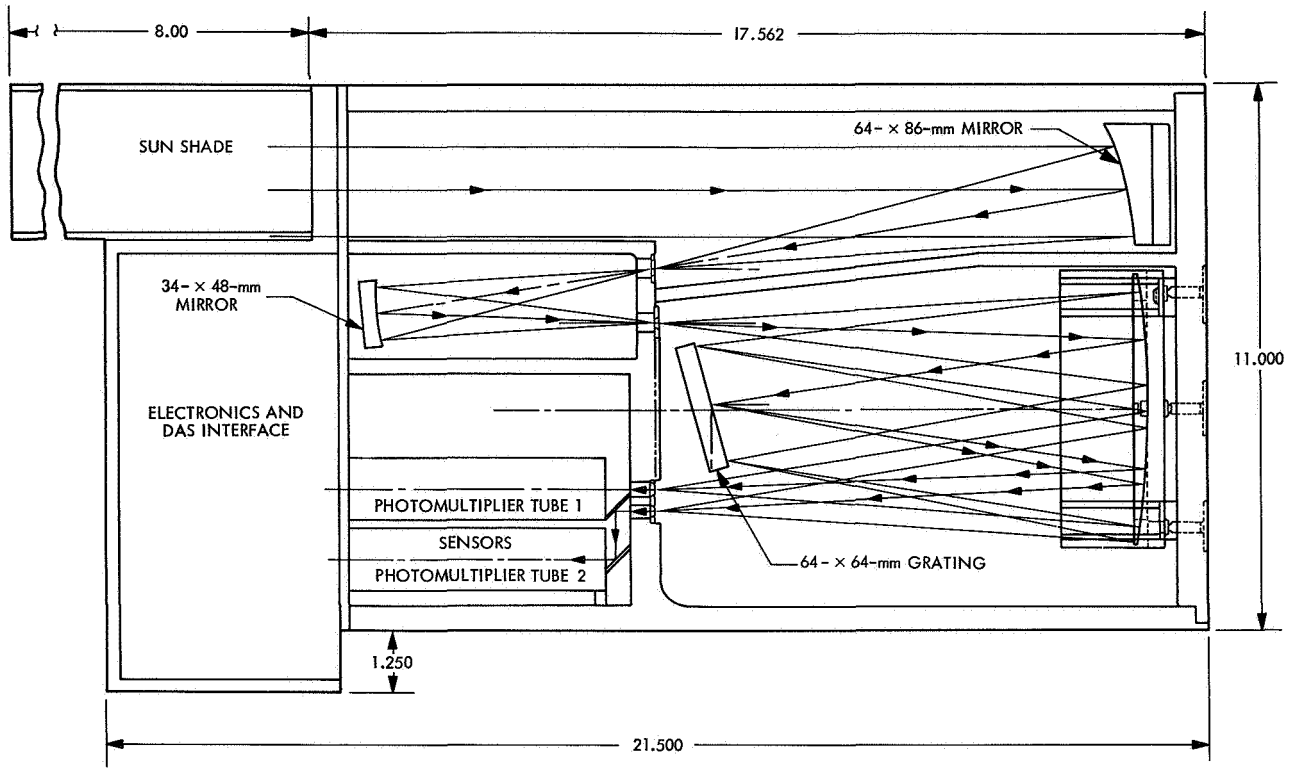

DIMENSIONS IN INCHES EXCEPT AS INDICATED

Fig. 47. Ultraviolet spectrometer physical configuration

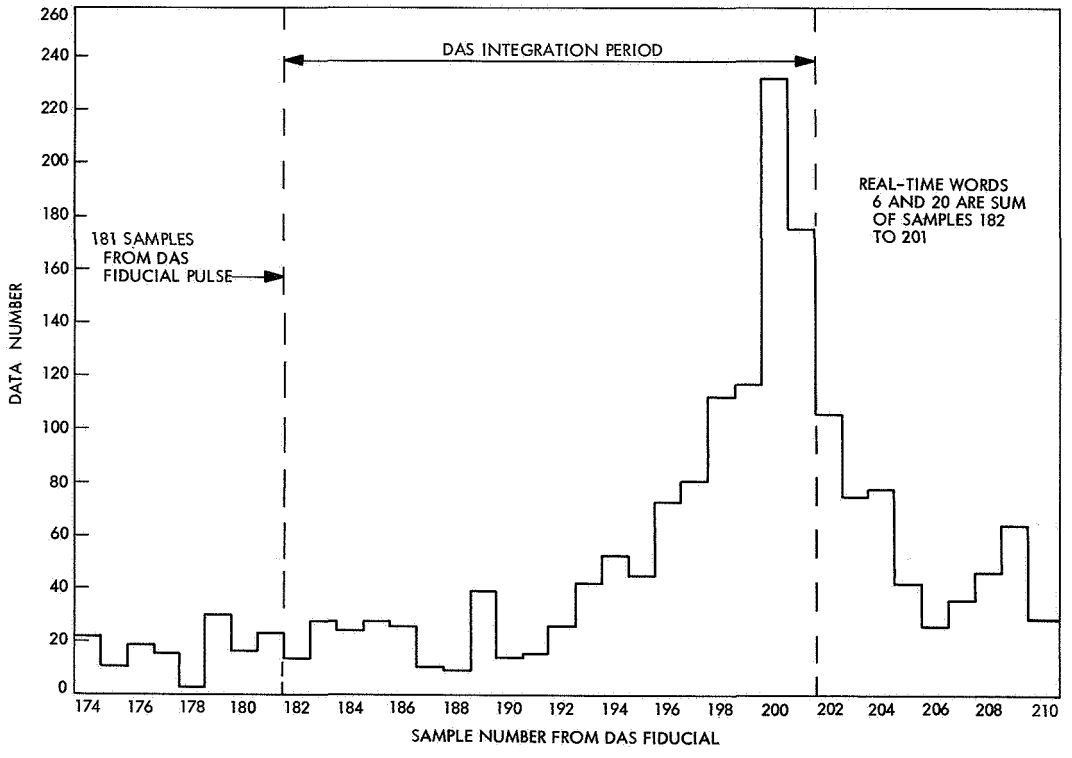

Fig. 48. Lyman-alpha portion of ultraviolet spectrum sampled in real time

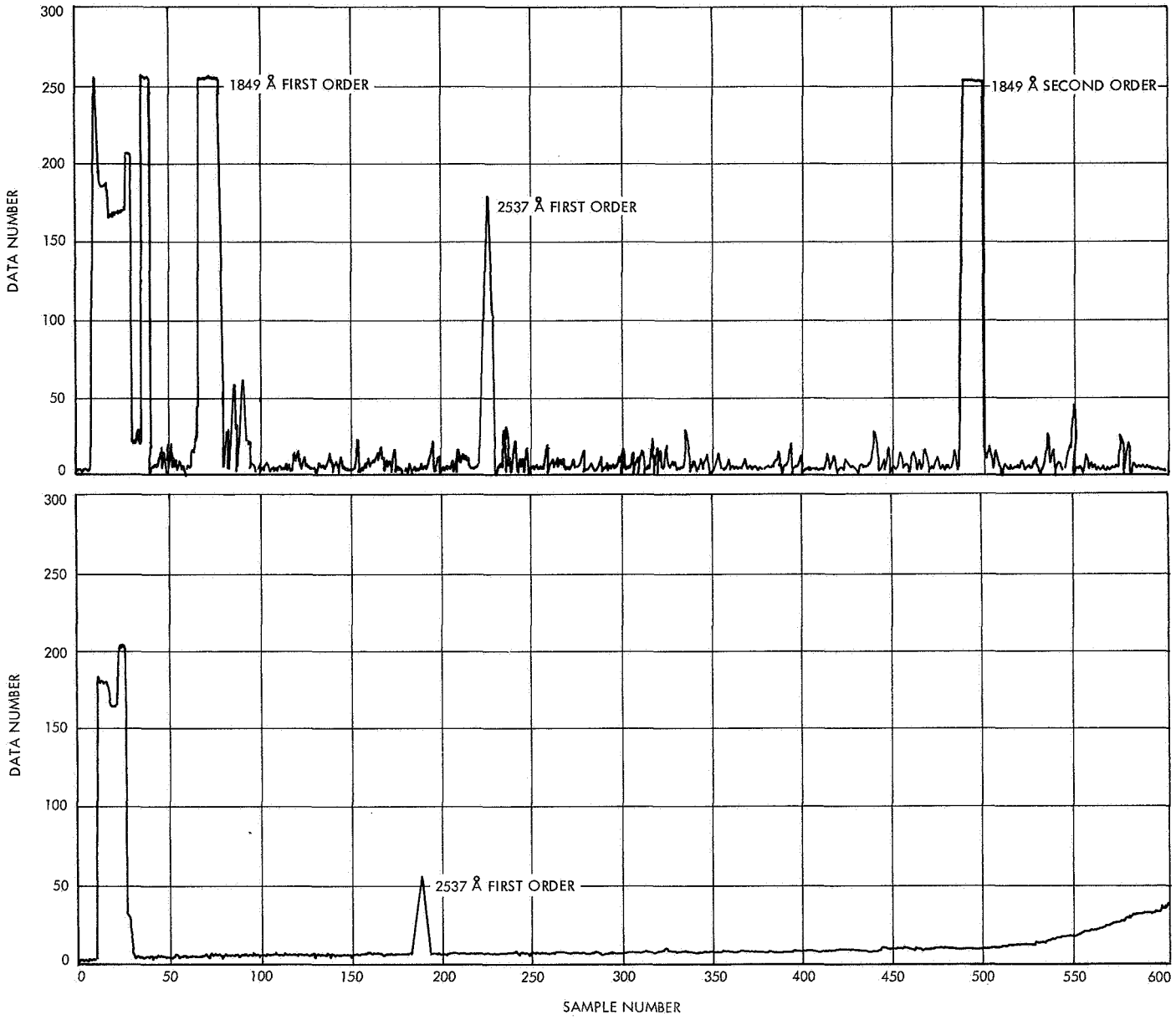

Fig. 49. Typical IBM 4020 computer plot of UVS data during systems test

To investigate the excessive light, "extended field" light-scattering tests were performed on the PTM and have shown that the quartz envelope of the internal stimulus causes excessive scattering of off-axis light into the instrument. The magnitude of the scattering is sufficiently great to warrant the removal of the lamp and accept the slightly increased risk resulting from no on-pad stimulus. It has been demonstrated from tests under the shroud that on-pad verification for the N channel can still be performed using the TV stimulus. In addition, the G channel engineering information and the random spikes produced by cosmic radiation should be sufficient to verify the operation of this channel in the absence of an actual stimulus. The risk of removing the stimulus is, therefore, minimal. The stimulus assembly will probably be removed from the flight units during the final calibration period.

The final calibration of the UVS instruments will be performed at the University of Colorado and complemented by calibration on the vacuum optical bench at the Goddard Space Flight Center.